ISSN: 2220-9506 (Print)
ISSN: 2414-0473 (Online)

ПРИБОРЫ И МЕТОДЫ ИЗМЕРЕНИЙ

DEVICES AND METHODS OF MEASUREMENTS

Том 12 № 1 Vol. 12

100 ЛЕТ БНТУ 1920

ХРАНИМ ТРАДИЦИИ, ЖИВЕМ НАСТОЯЩИМ, СОЗДАЕМ БУДУЩЕЕ!

2021

ПРИБОРЫ И МЕТОДЫ ИЗМЕРЕНИЙ

Научно-технический журнал

Основан в 2010 г.

Учредитель
Белорусский национальный технический университет

Выходит 4 раза в год

Журнал включен в базы данных:
Web of Science Core Collection (ESCI),
EBSCO, DOAJ, WorldCat, OpenAIRE, Google Scholar, РИНЦ,
ЭБС «Лань», НЭБ «КиберЛенинка», Соционет

Том 12 **№ 1** **2021**

Издание зарегистрировано в Министерстве информации Республики Беларусь 25 июня 2010 г.
Регистрационный номер 1372
В соответствии с решением ВАК от 8 июля 2011 г. №13/1 журнал включен в Перечень научных изданий для опубликования результатов диссертационных исследований; научное направление: «Средства и методы измерений, контроля, диагностики и оценки качества объектов и процессов» (технические и физико-математические науки)
ISSN 2220-9506

Подписка осуществляется через почтовые отделения связи по «Каталогу газет и журналов Республики Беларусь».
Подписные индексы – 74835; 748352.

Ответственный секретарь редакции: Шахлевич Л.Н.
Редактор: Чабарова О.Л.
Набор и верстка выполнены в редакции журнала «Приборы и методы измерений».
Подписано в печать 18.03.2021. Формат бумаги 60×84 1/8. Бумага мелованная.
Гарнитура Times New Roman. Печать цифровая. Усл. печ. л. 9,77. Уч.-изд. л. 3,82. Тираж 100 экз.
Дата выхода в свет 23.03.2021. Заказ № 134.
Отпечатано в Белорусском национальном техническом университете. ЛП № 02330/74 от 03.03.2014. Пр. Независимости, 65, 220013, г. Минск

АДРЕС РЕДАКЦИИ:
Белорусский национальный технический университет
пр. Независимости, 65, 220013, г. Минск, Республика Беларусь,
тел.: +375 (17) 293 96 67, факс: +375 (17) 292 67 94
e-mail: pimi@bntu.by
http://pimi.bntu.by

DEVICES AND METHODS OF MEASUREMENTS

Scientific and Engineering Journal

Founded in 2010

Founder
Belarusian National Technical University

Issued four times a year

The Journal is included in the following databases:
Web of Science Core Collection (ESCI),
EBSCO, DOAJ, WorldCat, OpenAIRE, Google Scholar,
RISC, Lan, CyberLeninka, Socionet

Volume 12 **№ 1** **2021**

ADDRESS:
Belarusian National Technical University
Nezavisimosty Ave., 65, Minsk 220013, Belarus
Tel.: +375 (17) 293 96 67, fax: +375 (17) 292 67 94
e-mail: pimi@bntu.by
http://pimi.bntu.by

СОДЕРЖАНИЕ

Средства измерений

Методы измерений, контроля, диагностики

CONTENTS

Measuring Instruments

Methods of Measurements, Monitoring, Diagnostics

Experimental Installation for Determination of Attenuation Coefficient of Permanent Magnetic Field by Protective Materials

V.M. Fedosyuk

*Scientific and Practical Materials Research Center of the National Academy of Sciences of Belarus,
P. Brovki str., 19, Minsk 220072, Belarus*

Received 19.01.2021
Accepted for publication 22.02.2021

Abstract

The permanent magnetic field in addition to electromagnetic radiation has a significant effect on performance of devices. This is particularly true for highly sensitive precision measuring equipment, such as, for example, magnetometers or photomultiplier tubes. In this regard a new high-performance materials for protection against permanent fields and electromagnetic radiation need to be developed. The purpose of this paper is a development of a hardware and software complex for high-precision determination of permanent magnetic field attenuation coefficient and certification of protective materials.

This paper describes an experimental installation for determining the attenuation coefficient of a permanent magnetic field using materials and coatings on standard package for electronic equipment. The installation ensures a uniform magnetic field flow in the measurement volume. The advantage of the measuring device is the ability to measure magnetic field in three coordinates due to the use of three pairs of Helmholtz coils and a three-dimensional Hall sensor. The software will enable to control of the magnetic field in all three directions, simulating the real operating conditions of devices that require protection from such influences. In addition, a movable positioning system makes it possible to compensate for the Earth's magnetic field, which increases the accuracy of estimating the attenuation coefficient by protective materials in weak magnetic field.

An alternative use of the capabilities of the installation is to test the performance of the devices in a permanent magnetic field and evaluate the electromagnetic compatibility. Experimental results of the work includes determination of the magnetic field attenuation coefficient using standard photomultiplier tube package made of electrolytically deposited permalloy and the sheet of annealed permalloy. Thus, the effect of annealing and closed magnetic circuit on the degree of weakening of the magnetic field is shown. It has been demonstrated that annealing which causes a significant increase in the magnetic permeability promotes an effective attenuation of weak magnetic fields (up to 1 mT). In magnetic fields with an induction of 1 mT or more, effective attenuation is provided by a closed magnetic circuit.

Keywords: Helmholtz coils, constant magnetic field, attenuation coefficient, permalloy.

DOI: 10.21122/2220-9506-2021-12-1-7-12

Адрес для переписки:
Федосюк В.М.
НПЦ НАН Беларуси по материаловедению,
ул. П. Бровки, 19,
г. Минск 220072, Беларусь
e-mail: fedosyuk@physics.by

Address for correspondence:
Fedosyuk V.M.
Scientific and Practical Materials Research Center of the National Academy of Sciences of Belarus,
P. Brovki str., 19, Minsk 220072, Belarus
e-mail: fedosyuk@physics.by

Для цитирования:
V.M. Fedosyuk.
Experimental Installation for Determination of Attenuation Coefficient of Permanent Magnetic Field by Protective Materials.
Приборы и методы измерений.
2021. – Т. 12, № 1. – С. 7–12.
DOI: 10.21122/2220-9506-2021-12-1-7-12

For citation:
V.M. Fedosyuk.
Experimental Installation for Determination of Attenuation Coefficient of Permanent Magnetic Field by Protective Materials.
Devices and Methods of Measurements.
2021, vol. 12, no. 1, pp. 7–12.
DOI: 10.21122/2220-9506-2021-12-1-7-12

Экспериментальная установка для определения коэффициента ослабления постоянного магнитного поля защитными материалами

В.М. Федосюк

Научно-практический центр Национальной академии наук Беларуси по материаловедению, ул. П. Бровки, 19, г. Минск 220072, Беларусь

Поступила 19.01.2020
Принята к печати 22.02.2021

Постоянное магнитное поле наряду с электромагнитным излучением оказывает существенное влияние на рабочие характеристики и работоспособность приборов. Особенно это касается высокочувствительного прецизионного измерительного оборудования, такого как, например, магнитометры или фотоэлектронные умножители. В связи с этим возникает необходимость разработки новых высокоэффективных материалов для защиты от воздействия постоянного магнитного поля и электромагнитного излучения. Целью данной работы являлась разработка программно-аппаратного комплекса для высокоточного определения коэффициента ослабления постоянного магнитного поля и аттестации защитных корпусов.

В работе описана измерительная установка для определения коэффициента ослабления постоянного магнитного поля с помощью материалов и покрытий на стандартных корпусах. Установка обеспечивает однородное магнитное поле во всём измерительном объёме. Отличие измерительной установки от существующих стендов заключается в возможности проведения измерений в трёх координатах благодаря использованию трёх пар катушек Гельмгольца и трёхкоординатного датчика Холла. Программное обеспечение позволит управлять магнитным полем во всех трёх направлениях, моделируя реальные условия эксплуатации приборов, требующих защиты от таких воздействий. Кроме того, подвижная система позиционирования в пространстве позволяет компенсировать магнитное поле Земли, что повышает точность оценки коэффициента ослабления магнитного поля защитными материалами в слабых полях.

Альтернативным вариантом использования возможностей установки является проверка рабочих характеристик приборов в условиях воздействия постоянного магнитного поля и оценка электромагнитной совместимости. Экспериментальная часть работы включает результаты определения коэффициента ослабления магнитного поля с помощью стандартных корпусов для фотоэлектронного умножителя, изготовленных из листового отожжённого пермаллоя и пермаллоя, осаждённого электролитически на алюминиевую подложку. Таким образом, показано влияние отжига и замкнутости магнитоконтура на степень ослабления магнитного поля. Установлено, что отжиг, вызывающий существенное повышение магнитной проницаемости, способствует эффективному ослаблению слабых магнитных полей (до 1 мТл). В магнитных полях с индукцией от 1 мТл эффективное ослабление обеспечивает замкнутый магнитоконтур.

Ключевые слова: катушки Гельмгольца, постоянное магнитное поле, коэффициент ослабления, пермаллой.

DOI: 10.21122/2220-9506-2021-12-1-7-12

Адрес для переписки:
Федосюк В.М.
НПЦ НАН Беларуси по материаловедению,
ул. П. Бровки, 19,
г. Минск 220072, Беларусь
e-mail: fedosyuk@physics.by

Address for correspondence:
Fedosyuk V.M.
Scientific and Practical Materials Research Center of the National Academy of Sciences of Belarus,
P. Brovki str., 19, Minsk 220072, Belarus
e-mail: fedosyuk@physics.by

Для цитирования:
V.M. Fedosyuk.
Experimental Installation for Determination of Attenuation Coefficient of Permanent Magnetic Field by Protective Materials.
Приборы и методы измерений.
2021. – Т. 12, № 1. – С. 7–12.
DOI: 10.21122/2220-9506-2021-12-1-7-12

For citation:
V.M. Fedosyuk.
Experimental Installation for Determination of Attenuation Coefficient of Permanent Magnetic Field by Protective Materials.
Devices and Methods of Measurements.
2021, vol. 12, no. 1, pp. 7–12.
DOI: 10.21122/2220-9506-2021-12-1-7-12

Introduction

The problem of exposure to various types of electromagnetic fields on the equipment and systems, as well as living organisms is extremely important and multifaceted due to the complexity of interpretation of the processes of interaction of fields with the materials [1–3]. There are many fairly effective solutions for protection against electromagnetic radiation divided into active and passive protection methods [4–6]. The most difficult task is protection from exposure by static magnetic fields. This problem is acute for precision measuring equipment and space equipment [7] which is intensely exposed to constant and alternating magnetic fields. The physical principle of protection against magnetostatic effects consists in shunting the magnetic flux by a housing made from ferromagnetic material with high magnetic permeability [8–9]. The force lines of the external magnetic field will predominantly pass through the material with high magnetic permeability and will not affect the operation of the enclosed equipment. In connection with the above, active developments are underway in the field of creating materials and optimizing housing designs for effective weakening of magnetic flux and protection of sensitive electronics and equipment [10–14].

An important stage in the development of materials and housings is certification and determination of the degree of weakening of the magnetic field using a protective housing. The developers face the greatest number of difficulties when determining the shielding of weak magnetic fields from which it is necessary to protect, for example, photomultiplier tubes operating in outer space (of the orbit of the "MIR" station, the magnetic field induction is 0.4–0.6 mT). Difficulties in the development of measuring equipment are primarily related to the need to create a uniform and controlled magnetic flux as well as to compensate for the Earth's magnetic field to improve accuracy. Therefore the main goal of this work was to develop a software and hardware complex for high-precision determination of the attenuation coefficient of a constant magnetic field and certification of protective enclosures.

Installation for determining the magnetostatic shielding effectiveness

Device for determining the magnetic field attenuation coefficient should include the following capabilities:

– ensuring a uniform magnetic field throughout the entire volume of measurements;

– possibility of standard package for electronic equipment attestation;

– ability to carry out measurements at a magnetic field induction from 0.03 to 0.5 mT for materials that weaken the magnetic field by 100 times, and in the range from 0.5 to 10 mT for materials that weaken by 1000 times;

– compensation of the Earth's magnetic field when measuring in weak fields;

– ability to measure in three coordinates.

The problem of forming a uniform magnetic field and constant magnetic flux in a certain volume of space can be solved in many ways. Often for this permanent magnets are used between the poles of which a constant field is formed without the application of any energy. The main disadvantage of such a solution is the complexity of a controlled change in the magnitude of the magnetic field, since the magnitude of the magnetic induction for permanent magnets is determined exclusively by the remanent magnetization of the material and the distance between its poles.

It is advisable to create a weak and uniform magnetic field (up to 0.1 T) with a variable value using solenoids or coils. It is better to use electromagnets to generate magnetic fields of greater magnitude with which you can obtain a high magnetization of the core with a relatively low current value or a coreless coil made of superconducting material.

Since an important criterion for a measuring device is to obtain a magnetic field with a high degree of homogeneity, the most promising solution seems to be the use of Helmholtz coils which substitute two solenoids located coaxially at a distance equal to their radius, as shown in Figure 1*a*. The coils diameter should be larger than the size of the area in which a uniform magnetic flux is required. Figure 1*b* shows how the magnetic induction B will change along the axis of the Helmholtz coils. The graph is plotted schematically in relative units where one corresponds to the maximum value of B. The magnetic induction at the midpoint on the axis between coils can be calculated using the equation (1):

$$B = \left(\frac{4}{3}\right)^{3/2} \frac{\mu_0 n I}{R}, \qquad (1)$$

where μ_0 is the magnetic constant, $1.257 \cdot 10^{-6}$ T·m/A; n is the number of turns of the coil; I is the current flowing through the coil, A; R is the radius of the coil, m.

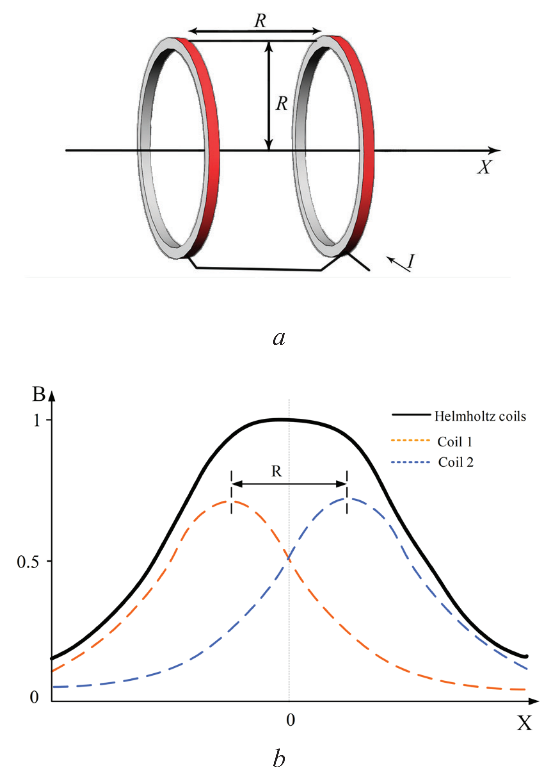

Figure 1 – Image of Helmholtz coils (*a*) and a schematic graph of changes in the magnetic induction of Helmholtz coils (*b*)

For implementation of the comprehensive certification of protective enclosures for radio electronic equipment it is important to be able to control not only the magnitude of the magnetic field but also the direction of the magnetic flux. Therefore, the facility under development includes three pairs of Helmholtz rings with a diameter of 30, 35 and 40 cm generating a constant magnetic field directed along the X, Y, and Z axes, respectively. In this case, the magnetic flux Φ for each of the coils is numerically equal to the magnetic induction B multiplied by the cross-sectional area of the coil S in square meters (2):

$$\Phi = B \cdot S. \tag{2}$$

To register the magnitude of the magnetic field the installation uses a three-coordinate Hall sensor with ferrite concentrators of the magnetic strip installed at the intersection of the axes of the coils in such a way that the plane of the sensor crystal is perpendicular to the magnetic flux lines. The signal from the sensor is read by a nanovoltmeter. Figure 2 shows a diagram of an installation with two pairs of Helmholtz coils. The pairs of coils are connected to a direct current source during the flow of which a constant uniform magnetic field is created. The current strength is directly proportional to the magnetic field strength H, therefore, the coefficients $k_{I \to H}$ for recalculating the current strength into the magnetic field induction according to formula (3) for each pair of coils have been experimentally established. Their values are presented in Table.

$$H = k_{I \to H} \cdot I. \tag{3}$$

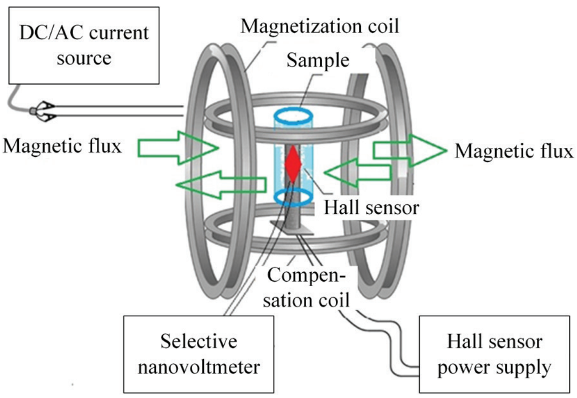

Figure 2 – Installation for measuring the attenuation coefficient of a permanent magnetic field

Table

Helmholtz coil parameters

№	Magnetic flux direction axis	Coil diameter, d, m	Conversion factor, $k_{I \to H}$
1	Y	0.40	$2.24 \cdot 10^{-3}$
2	X	0.35	$2.28 \cdot 10^{-3}$
3	Z	0.30	$2.33 \cdot 10^{-3}$

The installation has the ability to adjust its position in space to compensate for the Earth's magnetic field. To compensate it is necessary to install the three-coordinate Helmholtz coils in the optimal position achieving the minimum value of the potential difference on the sensitive element of the Hall sensor due to spatial manipulation.

It is necessary to calibrate the Hall sensor by setting the reference values of the potential difference over the entire range of magnetic fields with the step selected for the measurement before each measurement of the shielding efficiency. The change in the intensity of the external permanent magnetic field formed by the Helmholtz coils is carried out by changing the value of the constant current at the power source. After calibration the Hall sensor is placed in a protective case or covered with a cylindrical or flat shield keeping its position in space unchanged. The values of the potential difference on the sensor protected by the shield are recorded at the same values of the magnetic field strength. Shielding efficiency E is often a dimensionless quantity that shows how many times the strength of an external magnetic field decreases when a shield is used. The calculation of the magnetostatic shielding efficiency is carried out according to the formula:

$$E = (U_0/U_x), \quad (4)$$

where U_0 is the value of the potential difference (arithmetic mean) on the sensitive element of the Hall sensor without package (reference value); U_x is the value of the potential difference (arithmetic mean) on the sensitive element of the Hall sensor when using a protective case.

The attenuation coefficient k_E (or the efficiency expressed in decibels) is used to assess the effectiveness of shielding. k_E can be estimated using formula (5):

$$k_E = 20\lg(U_0/U_x) \text{ or } k_E = 20\lg E, \text{ dB}. \quad (5)$$

Experimental results

The weakening coefficients of the magnetic field were determined for two cylindrical specimens made of sheet permalloy (GOST 10160-75) and an aluminum cylinder coated with the same material ($Ni_{80}Fe_{20}$) using the developed installation. Samples had equal overall dimensions (length of 120 mm, a diameter of 45 mm, and a thickness of the magnetic material of 0.5 mm). An annealed permalloy foil was rolled into a cylinder of the corresponding diameter and spot welded to prepare a sheet sample. A coating was deposited on aluminum cylinder of appropriate size by electrolytic deposition as described in [15]. The shape of the sample is due to the fact that it matches the size of the housing of a wide range of photomultiplier tubes. $Ni_{80}Fe_{20}$ alloy was chosen as a reference sample as one of the most effective materials for protection against permanent magnetic field and electromagnetic radiation due to its high magnetic permeability [8]. High magnetic permeability provides effective shunting of the magnetic flux and, accordingly, a strong weakening of the magnetic field strength after passing through the coating (Figure 3).

The measurements of the magnetic field attenuation coefficient by the coating material were carried out in the range of magnetic fields from 0.1 to 9 mT. The results are shown in Figure 4.

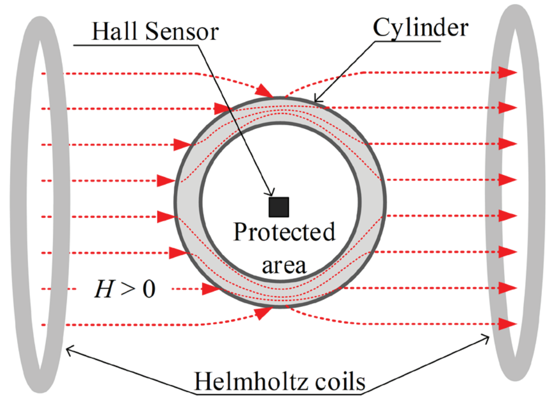

Figure 3 – Schematic representation of the principle of shunting magnetic flux using a cylindrical body made of material with high magnetic permeability

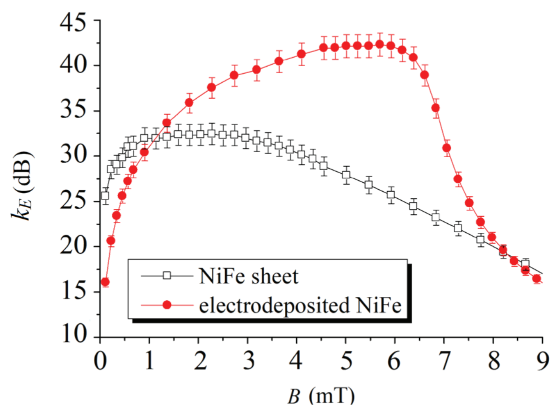

Figure 4 – Results of the study of the magnetic field attenuation coefficient after passing through the package made of sheet permalloy and the package with the electrodeposited permalloy coating

It was found that in the range of weak magnetic fields (up to 1 mT) a sample of annealed sheet permalloy is a more promising material, since it demonstrates an attenuation of the order of 26–32 dB, which corresponds to 20–43 times, while the electrodeposited and unannealed sample in this the same range showed an increase in the attenuation coefficient from 16 to 31 times (or from 6 to 35 times). However, with a further increase in the magnetic field induction, no increase in the attenuation coefficient was observed for the sheet permalloy sample. The maximum value of k_E for a sheet sample was 32.7 dB or 43 times. The attenuation coefficient increased to 42.3 dB, which corresponds to 130 times. Thus, it is shown that in the range of magnetic fields up to 1 mT the most significant factor for increasing the efficiency of magnetic flux attenuation is the high magnetic permeability of the protective material,

Devices and Methods of Measurements
2021, vol. 12, no. 1, pp. 7–12
V.M. Fedosyuk

which is characteristic of annealed alloys. In fields from 1 mT, the limiting factor for effective shunting of the magnetic flux is the closedness of the magnetic circuit or the continuity of the coverage in this case.

Conclusion

A unique measuring installation has been developed to determine the attenuation coefficient of the permanent magnetic field using protective package for electronic equipment. The installation will allow simulating the external effect of a permanent magnetic field in three-dimensional space to determine the effectiveness of protective materials and assess the performance of partings. The installation has a high accuracy in measuring weak magnetic fields due to the uniform magnetic flux generated by three pairs of Helmholtz coils and compensation of the Earth's magnetic field.

Certification of cylindrical package for protection against magnetostatic effects made of sheet permalloy and in the form of an electrodeposited coating on a cylindrical substrate has been carried out. It is shown that in weak fields (up to 0.1 mT), permalloy – annealed with in accordance with GOST 10160-75 – is a more effective material and weakens the magnetic field by 20–43 times due to high magnetic permeability. However with an increase in the magnetic field induction above 0.1 mT the most important parameter providing effective attenuation is the closed magnetic circuit. Thus the continuous coating showed attenuation up to 130 times while the sheet alloy body had an attenuation coefficient of less than 43 times.

References

1. Chung D.D.L. Materials for electromagnetic interference shielding. *Mater. Chem. Phys*., 2020, vol. 255, p. 123587. **DOI:** 10.1016/j.matchemphys.2020.123587

2. Geetha S., Satheesh Kumar K.K., Chepuri R., Rao K., Vijayan M., Trivedi D.C. EMI shielding: Methods and materials. *A review. J. Appl. Polym. Sci*., 2009, vol. 112, iss. 4, pp. 2073–2086. **DOI:** 10.1002/app.29812

3. Chung D.D.L. Electromagnetic interference shielding effectiveness of carbon materials. *Carbon*, 2001, vol. 39, iss. 2, pp. 279–285.
DOI: 10.1016/S0008-6223(00)00184-6

4. Steven Reimers S. System and method for shielding electrical components from electromagnetic waves. Patent United States US6320123B1. Date: 2019-10-20.

5. Shenkman A., Sonkin N., Kamensky V. Active protection from electromagnetic field hazards of a high voltage power line. *HAIT J. Sci. Eng. B*., 2005, vol. 2, pp. 254–265.

6. Zhang Q., Liang Q., Zhang Z., Kang Z., Liao Q., Ding Y., Ma M., Gao F., Zhao X., Zhang Y. Electromagnetic Shielding Hybrid Nanogenerator for Health Monitoring and Protection. *Adv. Funct. Mater*., 2018, vol. 28, p. 1703801.
DOI: 10.1002/adfm.201703801

7. Sumner T.J., Pendlebury J.M., Smith K.F. Convectional magnetic shielding. *J. Phys. D: Appl. Phys*., 1987, vol. 20, p. 1095. **DOI:** 10.1088/0022-3727/20/9/001

8. Grabchikov S.S., Trukhanov A.V., Trukhanov S.V., Kazakevich I.S., Solobaya A.A., Erofeenko V.T., Vasilenkov N.A., Volkova O.S., Shakin A. Effectiveness of the magnetostatic shielding by the cylindrical shells. *J. Magn. Magn. Mater*., 2016, vol. 398, pp. 49–53. **DOI:** 10.1016/j.jmmm.2015.08.122

9. Trukhanov A.V., Grabchikov S.S., Solobai A.A., Tishkevich D.I., Trukhanov S.V., Trukhanova E.L. AC and DC-shielding properties for the $Ni_{80}Fe_{20}$/Cu film structures. *J. Magn. Magn. Mater*., 2017, vol. 443, pp. 142–148. **DOI:** 10.1016/j.jmmm.2017.07.053

10. Ala G., Di M., Silvestre L. A simulation model for electromagnetic transients in lightning protection systems. *IEEE Trans. Electrom*., 2002, vol. 44, iss. 4, pp. 539–554. **DOI:** 10.1109/TEMC.2002.804773

11. Moglie F., Micheli D., Laurenzi S., Marchetti M., Primiania V.M. Electromagnetic shielding performance of carbon foams. *Carbon*, 2012, vol. 50, pp. 1972–1980.
DOI: 10.1016/j.carbon.2011.12.053

12. Unal E., Gokcen A, Kutlu Y. Effective electromagnetic shielding. *IEEE Microw. Mag*., 2006, vol. 7, iss. 4, pp. 48–54.
DOI: 10.1109/MMW.2006.1663989

13. Ishibashi K., Yoshioka T., Wakao S., Takahashi Y., Andjelic Z., Fujiwara K. Improvement of Unified Boundary Integral Equation Method in Magnetostatic Shielding Analysis. *IEEE Trans. Magn*., 2014, vol. 50, iss. 2, pp. 105–108, art. no. 7002404.
DOI: 10.1109/TMAG.2013.2282304

14. Reutov Yu.Ya. Physical interpretation of magnetostatic shielding. *Russian Journal of Nondestructive Testing*, 2000, vol. 36, pp. 117–126.
DOI: 10.1007/BF02759406

15. Zubar T.I., Fedosyuk V.M., Trukhanov A.V., Kovaleva N.N., Astapovich K.A., Vinnik D.A., Trukhanova E.L., Kozlovskiy A.L., Zdorovets M.V., Solobai A.A., Tishkevich D.I., Trukhanov S.V. Control of Growth Mechanism of Electrodeposited Nanocrystalline NiFe Films. *J. Electrochem. Soc*., 2019, vol. 166, iss. 6, pp. D173–D180. **DOI:** 10.1149/2.1001904jes

Design of Peltier Element Based on Semiconductors with Hopping Electron Transfer via Defects

N.A. Poklonski, S.A. Vyrko, A.I. Kovalev, I.I. Anikeev, N.I. Gorbachuk

Belarusian State University,
Nezavisimosti Ave., 4, Minsk 220030, Belarus

Received 28.01.2021
Accepted for publication 09.03.2021

The study of thermoelectric properties of crystalline semiconductors with structural defects is of practical interest in the development of radiation-resistant Peltier elements. In this case, the spectrum of energy levels of hydrogen-like impurities and intrinsic point defects in the band gap (energy gap) of crystal plays an important role.

The purpose of this work is to analyze the features of the single-electron band model of semiconductors with hopping electron migration both via atoms of hydrogen-like impurities and via their own point triple-charged intrinsic defects in the c- and v-bands, as well as to search for the possibility of their use in the Peltier element in the temperature range, when the transitions of electrons and holes from impurity atoms and/or intrinsic defects to the c- and v-bands can be neglected.

For Peltier elements with electron hopping migration we propose: (i) an h-diode containing $|d1)$- and $|d2)$-regions with hydrogen-like donors of two types in the charge states (0) and (+1) and compensating them hydrogen-like acceptors in the charge state (−1); (ii) a homogeneous semiconductor containing intrinsic t-defects in the charge states (−1, 0, +1), as well as ions of donors and acceptors to control the distribution of t-defects over the charge states. The band diagrams of the proposed Peltier elements in equilibrium and upon excitation of a stationary hopping electric current are analyzed.

A model of the h-diode containing hydrogen-like donors of two types $|d1)$ and $|d2)$ with hopping migration of electrons between them for 50 % compensation by acceptors is considered. It is shown that in the case of the reverse (forward) electrical bias of the diode, the cooling (heating) of the region of the electric double layer between $|d1)$- and $|d2)$-regions is possible.

A Peltier element based on a semiconductor with point t-defects is considered. It is assumed that the temperature and the concentration of ions of hydrogen-like acceptors and donors are to assure all t-defects to be in the charge state (0). It is shown that in such an element it is possible to cool down the metal–semiconductor contact under a negative electric potential and to heat up the opposite contact under a positive potential.

Keywords: doped semiconductor, diode with hydrogen-like donors of two types, triple-charged intrinsic point defects, electron hopping migration, Peltier element.

DOI: 10.21122/2220-9506-2021-12-1-13-22

Адрес для переписки:
Поклонский Н.А.
Белорусский государственный университет,
пр-т Независимости, 4, г. Минск 220030, Беларусь
e-mail: poklonski@bsu.by; poklonski@tut.by

Address for correspondence:
Poklonski N.A.
Belarusian State University,
Nezavisimosti Ave., 4, Minsk 220030, Belarus
e-mail: poklonski@bsu.by; poklonski@tut.by

Для цитирования:
N.A. Poklonski, S.A. Vyrko, A.I. Kovalev, I.I. Anikeev, N.I. Gorbachuk.
Design of Peltier Element Based on Semiconductors with Hopping Electron Transfer via Defects.
Приборы и методы измерений.
2021. – Т. 12, № 1. – С. 13–22.
DOI: 10.21122/2220-9506-2021-12-1-13-22

For citation:
N.A. Poklonski, S.A. Vyrko, A.I. Kovalev, I.I. Anikeev, N.I. Gorbachuk.
Design of Peltier Element Based on Semiconductors with Hopping Electron Transfer via Defects.
Devices and Methods of Measurements.
2021, vol. 12, no. 1, pp. 13–22.
DOI: 10.21122/2220-9506-2021-12-1-13-22

Схема элемента Пельтье на полупроводниках с прыжковым переносом электронов по дефектам

Н.А. Поклонский, С.А. Вырко, А.И. Ковалев, И.И. Аникеев, Н.И. Горбачук

*Белорусский государственный университет,
пр-т Независимости, 4, г. Минск 220030, Беларусь*

*Поступила 28.01.2021
Принята к печати 09.03.2021*

Исследование термоэлектрических свойств кристаллических полупроводников с дефектами структуры представляет практический интерес при создании радиационно-стойких элементов Пельтье. При этом важную роль играет спектр уровней энергии водородоподобных примесей и собственных точечных дефектов в энергетической щели (запрещённой зоне) кристалла.

Цель работы – анализ особенностей одноэлектронной зонной модели полупроводников с прыжковой миграцией электронов как по атомам водородоподобных примесей, так и по собственным точечным трёхзарядным дефектам, а также поиск возможности их использования в элементе Пельтье в области температур, когда переходами электронов и дырок с атомов примесей и/или собственных дефектов в c- и v-зоны можно пренебречь.

В качестве элементов Пельтье с прыжковой миграцией электронов предложены: 1) h-диод, содержащий |d1)- и |d2)-области с водородоподобными донорами двух сортов в зарядовых состояниях (0) и (+1) и компенсирующие их водородоподобные акцепторы в зарядовом состоянии (−1); 2) однородный полупроводник, содержащий собственные t-дефекты в зарядовых состояниях (−1, 0, +1), а также ионы доноров и акцепторов для управления распределением t-дефектов по зарядовым состояниям. Проанализированы зонные диаграммы предлагаемых элементов Пельтье в равновесии и при возбуждении стационарного прыжкового электрического тока.

Рассмотрена модель h-диода, содержащего водородоподобные доноры двух сортов |d1) и |d2) с прыжковой миграцией между ними электронов при компенсации их на 50 % акцепторами. Показано, что при обратном (прямом) электрическом смещении диода возможно охлаждение (нагревание) области двойного электрического слоя между |d1)- и |d2)-областями.

Рассмотрен элемент Пельтье на основе полупроводника с точечными t-дефектами. Принималось, что температура, а также концентрации ионов водородоподобных акцепторов и доноров таковы, что практически все t-дефекты находятся в зарядовом состоянии (0). Показано, что в таком элементе возможно охлаждение контакта металл–полупроводник, находящегося под отрицательным электрическим потенциалом, и нагревание противоположного контакта, под положительным потенциалом.

Ключевые слова: легированный полупроводник, диод с водородоподобными донорами двух сортов, трёхзарядные собственные точечные дефекты, прыжковая миграция электронов, элемент Пельтье.

DOI: 10.21122/2220-9506-2021-12-1-13-22

Адрес для переписки:
Поклонский Н.А.
Белорусский государственный университет,
пр-т Независимости, 4, г. Минск 220030, Беларусь
e-mail: poklonski@bsu.by; poklonski@tut.by

Address for correspondence:
Poklonski N.A.
Belarusian State University,
Nezavisimosti Ave., 4, Minsk 220030, Belarus
e-mail: poklonski@bsu.by; poklonski@tut.by

Для цитирования:
N.A. Poklonski, S.A. Vyrko, A.I. Kovalev, I.I. Anikeev, N.I. Gorbachuk.
Design of Peltier Element Based on Semiconductors with Hopping Electron Transfer via Defects.
Приборы и методы измерений.
2021. – Т. 12, № 1. – С. 13–22.
DOI: 10.21122/2220-9506-2021-12-1-13-22

For citation:
N.A. Poklonski, S.A. Vyrko, A.I. Kovalev, I.I. Anikeev, N.I. Gorbachuk.
Design of Peltier Element Based on Semiconductors with Hopping Electron Transfer via Defects.
Devices and Methods of Measurements.
2021, vol. 12, no. 1, pp. 13–22.
DOI: 10.21122/2220-9506-2021-12-1-13-22

Introduction

Thermoelectric phenomena in semiconductor systems caused by the migration of electrons in the c-band and holes in the υ-band are intensively studied (see, e. g., [1–7]). The thermopower was measured for hopping migration of holes via hydrogen-like acceptors of the same type in homogeneous germanium crystals at liquid helium temperatures and below [8, 9]; see also [10].

The efficiency of semiconductor materials used in thermoelectric converters is determined by the dimensionless thermoelectric figure of merit ZT and by the Peltier coefficient Π (see, e. g., [11–13]):

$$ZT = \frac{\sigma S^2 T}{\kappa}; \quad \Pi = ST, \tag{1}$$

where Z is the figure of merit [K^{-1}], $T = (T_1 + T_2)/2$ is the operating temperature [K], T_1 and T_2 are the absolute temperatures of hot and cold electrodes to the material, σ is the direct current specific electrical conductivity [Ohm^{-1}·m^{-1}], S is the Seebeck coefficient (or thermopower) [V/K], κ is the thermal conductivity [W·m^{-1}·K^{-1}], Π is the Peltier coefficient [V].

Note that the Peltier coefficient Π, as a rule, is not measured directly, but is calculated from Eq. (1) by the value of the Seebeck coefficient S, which is easier to measure.

There are various ways to increase the thermoelectric figure of merit (see, e. g., [12–14], as well as the reviews on this topic [15–19]): selection of the optimal concentration of mobile charge carriers (electrons, holes or ions) in homogeneous materials; selection of the optimal band gap (energy gap); changing the chemical composition of materials (e. g., by chemical doping or neutron transmutation doping) or modifying their structure by introducing, for example, radiation defects. The possibilities of increasing of the thermoelectric figure of merit of nanostructured materials consisting of low-dimensional systems are also considered [1]. Realistic estimates of the limiting values of figure of merit of thermoelectric composites are given in [3].

Investigation of the optimal band gap E_g of a semiconductor showed that the condition $E_g \gg k_B T$ should be fulfilled [4]. This is easily explained by the fact that for the Fermi level lying near the bottom of the c-band, the concentration of minority carriers (holes in the υ-band), and as a consequence, their contribution to the thermopower can be neglected. However, this method makes it possible to increase the ZT value insignificantly. The modification of the chemical composition and disordering of the structure consists in the preparation of solid solutions or the growth of disordered alloys based on them; in the selection of the optimal concentrations of these compounds; combining them. Some samples obtained by such methods demonstrated thermoelectric figure of merit up to $ZT = 2.2$ at room temperature (see, e. g., [14]).

The existence of an optimal doping level is due to the fact that an increase in the concentration of mobile charge carriers (electrons and/or holes) usually increases the electrical conductivity σ, but decreases the Seebeck coefficient S (see Eq. (1)). Due to an increase in the concentration of charge carriers, they become degenerate and the Fermi level goes into the c-band (or in the υ-band). In this case, the energy and velocities of electrons (or holes) will be determined by the Fermi level (Fermi energy) and will practically not depend on temperature. As a consequence, the charge fluxes from the hot and from the cold electrodes to the sample will hardly differ.

A Peltier element is a thermoelectric two-terminal device. When a stationary electric current is excited in it, it cools down at one contact (electrode) of the element and heats up at the other electrode. The Peltier element is still attractive for applications as a silent and environmentally friendly device. It can be used as a thermoelectric generator operating by utilizing heat losses in other devices and working substances.

Typically, Peltier elements consist of n- and p-type semiconductors connected in series with metal bridges. The contacts, which are cooled when passing an electric current, are placed on one surface of the Peltier element, and the contacts, which are heated, on the opposite surface. In the p- and n-branches of the electrical circuit of the Peltier element, holes and electrons move from the cooled surface to the heated one [20, 21].

Heat release power (energy released per unit time at the contact of a unit area) of the Peltier element [W·m^{-2}]:

$$W = \frac{Q}{At} = (\Pi_1 - \Pi_2)\frac{It}{At} = (\Pi_1 - \Pi_2)J, \tag{2}$$

where Q is the heat released at the contact [J], A is the cross-section area of the contact [m^2], t is the time [s], Π_1 and Π_2 are the Peltier coefficients of materials 1 and 2 brought into electric and thermal contact [V], I is the electric current [A], J is the electric current density [A/m^2]; It is the charge passing through the electrical contact of two different conductors [C]. The value $W > 0$ if heat is released, and $W < 0$ if heat is absorbed.

In the work [22] the *p–n* junction is considered as a potential thermoelectric device. Note that for the effective functioning of the *p–n* diode as a Peltier element, the width of the electric double layer in the *p–n* diode must be comparable or less than the diffusion length of electrons in the *c*-band and the diffusion length of holes in the υ-band. Electrons and holes formed in the electric double layer due to the absorption of heat in it go into electrical ohmic contacts (of n^+- and p^+-type) to the *n*- and *p*-type regions under the action of both the internal potential difference and the external electrical bias. In this case, the time of the drift "flight" of electrons and holes through the double layer should be less than their recombination lifetime [23].

Most works on thermoelectricity proceed from the band theory of crystalline solids and consider the migration of electrons delocalized in the *c*-band and υ-band holes.

Within the framework of the band theory of crystalline solids, first proposed by Wilson (see essay [24]) on the basis of quantum mechanics, materials were distinguished by their electrical properties into insulators, semiconductors, and metals according to their single-electron energy spectrum. Subsequently, this led to the creation of the first bipolar transistors (see, e. g., [25, 26]) on germanium crystals, as well as integrated circuits on silicon [27]. Charge coupled devices (based on the metal–insulator–semiconductor structure) were invented [28, 29], which made it possible to record optical images in digital form. Finally, the features of the electron energy spectrum of layered semiconductor structures, called semiconductor heterostructures, consisting of semiconductor materials with different band gap, were used to create semiconductor lasers [30, 31] that operate at room temperature and above. Nevertheless, the potential of defects in the crystal structure of semiconductors for creating devices based on them is far from being realized within the limits of the possible.

It is known that the properties of semiconductors containing crystal structure defects substantially depend on the type of defects, their concentration, and spatial distribution (see, e. g., [32, 33]). In this regard, it is of practical interest to study the thermoelectric properties of semiconductor materials with hopping electron migration via impurity atoms and/or intrinsic point defects of the crystal matrix.

Let us briefly consider the possible arrangements of the energy levels of impurity atoms (hydrogen-like donors of two types) or intrinsic point triple-charged defects of the crystal structure in the band gap of semiconductors, suitable for the development of Peltier elements on their basis.

In crystalline semiconductors doped with hydrogen-like impurities at low temperatures, *c*-band electrons are "frozen out" on donors (υ-band holes – on acceptors). In this case, electrical conduction is carried out through the hopping migration of electrons (or holes) via impurity atoms. For example, it was shown in [34] that the hopping migration of holes via boron atoms (as acceptors) and electrons via phosphorus atoms (as donors) in diamond occurs even at room temperature (see also [35]). However, impurity atoms with an increase in their concentration in the crystal matrix form clusters (associates) [36]. In general, hopping electrical conduction in crystals at room temperature can be realized via *t*-defects – radiation point defects of one type in three charge states (−1, 0, +1). Such radiation defects make it possible to significantly modify the electrical properties of semiconductors without changing their chemical composition [37–39].

The purpose of the work is to analyze the manifestation of the arrangement of the energy levels of atoms of hydrogen-like impurities or intrinsic point defects in the band model of crystalline semiconductors with hopping electron migration for the design of the Peltier element.

In this paper, two possible schemes for the implementation of Peltier elements based on two semiconductor systems with hopping electron migration between ohmic contacts (electrodes) to these systems are considered.

The first system is a flat crystalline semiconductor sample, on the one side doped with hydrogen-like donors with thermal ionization energy E_{d1}, and on the other side – with hydrogen-like donors with ionization energy $E_{d2} < E_{d1}$. Donors of two types can be in charge states (0) and (+1). Each donor introduces one energy level into the band gap. The degree of compensation by hydrogen-like acceptors is approximately 50 %. The hopping transfer of electrons via donors is “refracted” at the region of the electric double layer between the $|d1)$- and $|d2)$-regions of the system, which form the *h*-diode. Thus, the *h*-diode contains a $|d1)$–$|d2)$ junction and ohmic contacts to $|d1)$- and $|d2)$-regions. (The properties of ohmic contacts to such semiconductors are presented in reviews [40, 41].)

The second system is a partially disordered semiconductor containing radiation *t*-defects in the dominating concentration, each of which can be in one of three charge states (−1, 0, +1). Each *t*-defect introduces two energy levels into the band gap. Hydrogen-like donors and acceptors are ionized and control the number of *t*-defect charge states that are realized at a given temperature.

Design 1 – hopping electron migration via donors of two types

In contrast to works [8–10], let us consider an *n*-type crystalline semiconductor doped with hydrogen-like donors of two types (|d1) and |d2)) with different thermal ionization energies ($E_{d1} > E_{d2}$); see Figure 1*a*. The charge states (0) and (+1) of |d1) donors in the region $x < x_j = 0$ and |d2) donors in the region $x > x_j$ provide the possibility of hopping electrical conduction. Compensating acceptors of one type |a), uniformly distributed along the *x* axis, are in the charge state (−1). Fluctuations in the energy levels of impurities are not shown. Short lines within the band gap indicate the mean values of the donor ionization energy.

We assume that all hydrogen-like donors |d1) and |d2) with concentrations $N_{d1}(x)$ and $N_{d2}(x)$ are immobile and are in charge states (0) and (+1), and their distribution along the *x* coordinate (along the diode) is determined as follows [42]:

$$N_{d1}(x) = \frac{N_{d1}}{1+\exp(x/l)}, \quad N_{d2}(x) = \frac{N_{d2}}{1+\exp(-x/l)}, \quad (3)$$

where N_{d1} and N_{d1} are the maximum concentrations of |d1) and |d2) donors [m^{-3}]; *l* is the doping profile parameter [m]; $x = x_j = 0$ in Figure 1 corresponds to $N_{d1}(x_j) = N_{d1}$ and $N_{d2}(x_j) = N_{d2}$. The concentration of hydrogen-like acceptors N_a does not depend on the *x* coordinate; all acceptors are in the charge state (−1).

To implement *h*-diode with the Peltier effect on *n*-type silicon crystal, in the capacity of |d1) donors we can take arsenic atoms (As) with thermal ionization energy $I_{d1} = 53.8$ meV and in the capacity of |d2) donors – antimony atoms (Sb) with thermal ionization energy $I_{d2} = 42.7$ meV [43]. Boron (B) or aluminium (Al) atoms can be taken as compensating acceptors.

The critical donor concentration $N_d = N_M$, corresponding to the low-temperature transition of a semiconductor crystal from the insulator state to the metallic one (the Mott transition), is given by the relation [44]:

$$N_M^{1/3} a_H = \frac{0.542}{[(1-K)(\varepsilon_r+2)]^{1/3}}, \quad (4)$$

where $a_H = e^2/8\pi\varepsilon_r\varepsilon_0 I_d$ is the Bohr radius [m] for a single donor with the ionization energy I_d [J]; *e* is the elementary charge [C]; ε_r is the relative permittivity; ε_0 is the electric constant [F/m]; $K = N_a/N_d$ is the compensation ratio.

Figure 1 shows the case of hopping electrical conduction via donors of two types with equal donor concentrations $N_{d1} = N_{d2} \approx 0.1 N_M$ and the ratio of their compensation by acceptors $K = N_a/N_{d1} = N_a/N_{d2} = 0.5$. In this case, the effective concentration of electrons hopping via both |d1) donors and |d2) donors is maximum [45].

When a reverse bias is applied (Figure 1*b*; $U_r < 0$), in the region where the type of doping donors changes, due to electron hopping the heat $Q_{ab} \approx E_{d1} - E_{d2}$ will be absorbed, which is necessary to overcome the difference in the ionization energy of |d1) and |d2) donors. The junction region will cool down in this case. And vice versa, when a forward bias is applied (Figure 1*c*; $U_f > 0$), in the region where the type of doping donors changes, due to electron transitions to deeper donors an excess of electron energy will be released in the form of heat $Q_{em} \approx E_{d1} - E_{d2}$, and the junction region will heat up.

The typical temperature T_h, at which the electrical conduction of a semiconductor is determined only by the hopping migration of electrons via hydrogen-like donors, is $T_h = T_j/2$, where T_j is the temperature at which the *c*-band and hopping electrical conductivities are equal. The temperature T_j is given by the expression [46]:

$$T_j = \frac{0.728}{k_B}\frac{e^2}{4\pi\varepsilon_r\varepsilon_0}(KN_d)^{1/3}, \quad (5)$$

where k_B is the Boltzmann constant [J/K]; *e* is the elementary charge [C]; $\varepsilon_r\varepsilon_0$ is the dielectric constant of the crystal matrix [F/m]; $N_d = N_{d1} = N_{d2}$ is the concentration of the doping impurity (|d1) and |d2) donors) [m^{-3}]. [Electrical neutrality condition: the concentration of donors in the charge state (+1) is equal to the concentration of the negatively charged (−1) compensating impurity (acceptors) KN_d.]

In a doped semiconductor with compensation ratio $K \approx 0.5$, the ionization energy of hydrogen-like donors decreases with their concentration [47]:

$$E_d = I_d\left(1 - \frac{a_H}{R_{res}}\right), \quad (6)$$

where $R_{res} = (2\pi N_d)^{-1/3}$ is the radius of the spherecal region of the crystal matrix per impurity atom (both donor and acceptor) at $K = 0.5$.

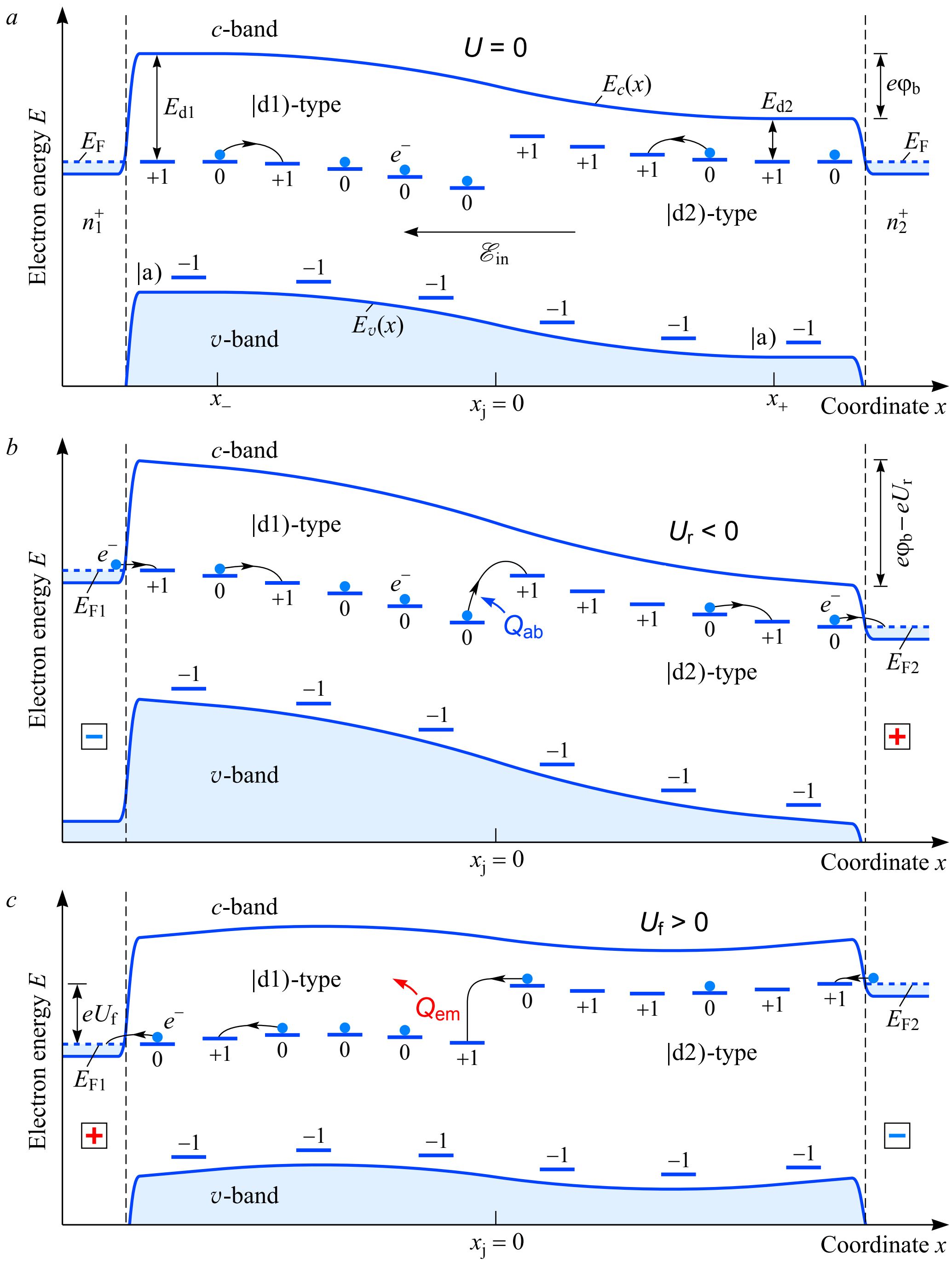

Figure 1 – Band diagrams (dependences of the single-electron energy E on the coordinate x) at low temperatures for a Peltier element based on the h-diode, which is an n-type semiconductor doped with hydrogen-like donors of two types $|\mathrm{d1})$ and $|\mathrm{d2})$ with different thermal ionization energies ($E_{\mathrm{d1}} > E_{\mathrm{d2}}$) and compensated by acceptors $|\mathrm{a})$: in the equilibrium (a; $U = 0$), under the reverse bias (b; $U_\mathrm{r} < 0$) and under the forward bias (c; $U_\mathrm{f} > 0$). The potential barrier height: $e\varphi_\mathrm{b}$ (a), $e\varphi_\mathrm{b} - eU_\mathrm{r}$ (b), $e\varphi_\mathrm{b} - eU_\mathrm{f}$ (c); the electrical double layer width is ($x_+ - x_-$). In the case of the reverse bias (b; $U_\mathrm{r} < 0$), heat Q_{ab} is absorbed in the junction region and the structure cools down. Under the forward bias (c; $U_\mathrm{f} > 0$), heat Q_{em} is released in the junction region and the structure heats up. The Peltier element operates in the vicinity of the temperature of realization of the hopping conductance $T_\mathrm{h} = T_\mathrm{j}/2$, where T_j is given by Eq (5)

Note that to implement the device structure (h-diode) with the Peltier effect on a p-type silicon crystal, in the capacity of $|\mathrm{a1})$ and $|\mathrm{a2})$ acceptors, we can take boron atoms (B) with the thermal ionization energy $I_{\mathrm{a1}} = 44.4$ meV and aluminium atoms (Al) with the ionization energy $I_{\mathrm{a2}} = 69$ meV, respectively [43]. Antimony (Sb) or arsenic (As) atoms can be taken as compensating donors.

A thermal cooler of this type can be used as a "cold finger" for bolometers [48] and infrared detectors [49] operating at cryogenic temperatures.

Design 2 – hopping electron transfer in a partially disordered semiconductor

A number of works (see, e. g., [50, 51] and references therein) describe the mechanisms of Fermi level "pinning" by point structure defects both at the metal–semiconductor interface and inside the semiconductor.

Let us consider the processes of transfer of electrons and energy in a "metal–partially disordered semiconductor–metal" device structure upon excitation of a stationary electric current in it.

The proposed scheme of a Peltier element based on a semiconductor with two energy levels (E_{t1} and E_{t2}) of point triple-charged t-defects [52, 53] is shown in Figure 2. We consider the case of hopping migration (drift and diffusion) of electrons via the upper level E_{t2} only.

Note that triple-charged point defects can be introduced into a semiconductor by polyenergetic ion implantation (ion kinetic energy > 1 MeV/nucleon) through contacts (electrodes) or by irradiation with fast reactor neutrons [38, 39].

Let us consider a one-dimensional model of the proposed device structure (Peltier element). A flat semiconductor sample is located between two metal electrodes (contacts); see Figure 2a. Two-level t-defects are created in the sample, each of which can be in one of three charge states (−1, 0, +1).

Let t-defects be immobile and uniformly distributed over the volume of the semiconductor:

$$N_t(x) = N_t = \text{const}, \tag{7}$$

where $N_t(x) = N_{t,-1}(x) + N_{t,0}(x) + N_{t,+1}(x)$ is the total concentration of t-defects in all three charge states.

As can be seen from Figure 2a, t-defects contained in a semiconductor effectively reduce its band gap to a value of $\Delta_t < E_g$. The width of the energy gap between the average values of the energy levels of t-defects is $\Delta_t = E_g - (E_{t1} + E_{t2}) > 3k_BT$. (Note that in a narrow-gap crystalline semiconductor, the band gap E_g is less than the electron affinity energy $\text{EA} = E_{vac} - E_c$, where E_{vac} is the vacuum level, E_c is the bottom of the c-band).

The average value of the lower energy level E_{t1} corresponds to the energy required for the transition of an electron from the v-band to the t-defect in the charge state (+1). The average value of the upper energy level E_{t2} corresponds to the energy required

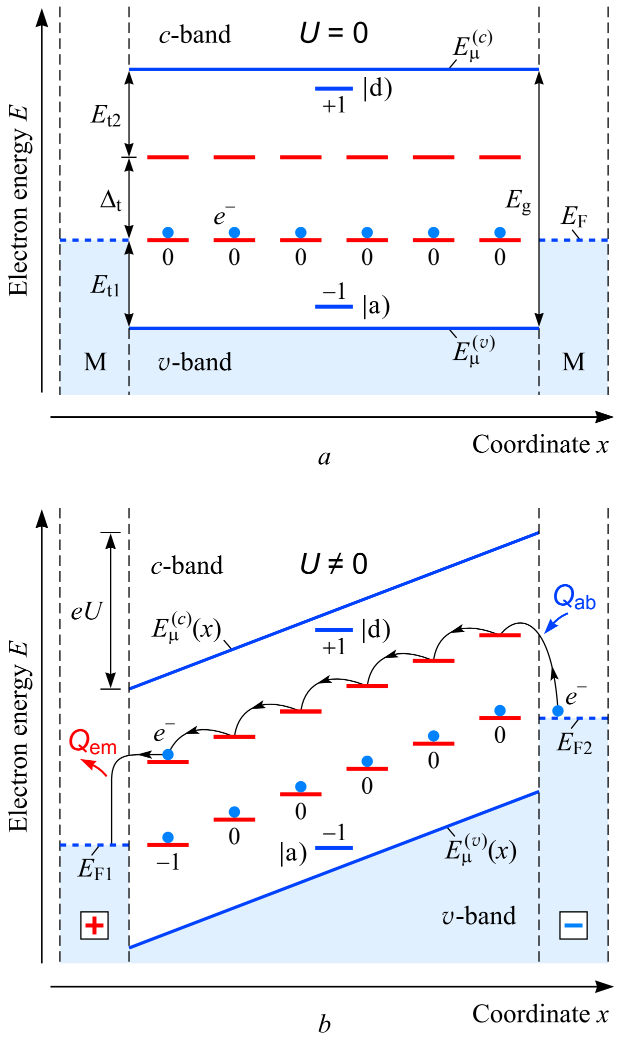

Figure 2 – Band diagrams $E(x)$ of the Peltier element in the thermodynamic equilibrium (a; $U = 0$) and under the electrical bias (b; $U \neq 0$). A semiconductor (working substance) contains ions of donor $|d)$ and acceptors $|a)$ along with triple-charged t-defects. When a stationary hopping current is excited (for $U \neq 0$), the heat Q_{ab} is absorbed in the region of the contact under a negative potential and the contact cools down, and in the region of the contact under a positive potential, the heat Q_{em} is released and the contact heats up

for the transition of an electron from the t-defect in the charge state (−1) to the bottom of the c-band. In a partially disordered semiconductors with a high concentration of defects, the energy positions of the edges of the allowed energy bands (the bottom of the c-band and the top of the v-band) fluctuate along the coordinate (have random deviations from the average value at different points of the crystal). When describing the electrical properties of such disordered semiconductors, the concept of the mobility edge (percolation threshold) for electrons in the c-band $E_\mu^{(c)}$ and holes in the v-band $E_\mu^{(v)}$ is introduced [54].

When an electrical bias is applied (Figure 2*b*; $U \neq 0$), in the region of contact under a negative potential a thermally stimulated transition of electron from a metal to a semiconductor occurs and the heat $Q_{ab} \approx \Delta_t$ is absorbed, which is necessary to overcome the energy difference between the upper level of t-defect E_{t2} and the Fermi level E_{F2} in metal. The contact region will cool down in this case. And vice versa, in the region of the opposite contact under a positive potential due to transitions of electrons from the t-defect upper level to the Fermi level E_{F1} in metal, the excess of the electron energy is released in the form of the heat $Q_{em} \approx \Delta_t$, and the contact region will heat up.

In combination with radioisotope heater, the proposed Peltier element (Figure 2) becomes a generator of electrical energy. It is less susceptible to radiation degradation than an element based on conventional moderately doped semiconductor crystals, since it contains triple charged t-defects in a sufficiently high concentration, which were previously introduced into the crystal matrix.

A decrease in the thermal conductivity of a Peltier element occurs due to the creation in a semiconductor material (working substance) of a sufficiently large (for realization of electron hopping) number of point defects of structure, which effectively scatter phonons (both optical and acoustic) of all wavelengths [55]. For example, at cryogenic temperatures, the thermal conductivity of amorphous SiO_2 is much lower than the thermal conductivity of crystalline SiO_2 [56].

Conclusion

As Peltier elements with the electron hopping migration between electrical contacts to the semiconductor we proposed: (i) an h-diode containing inhomogeneously distributed along the semiconductor hydrogen-like donors of two types $|d1)$ and $|d2)$ in the charge states (0) and (+1), as well as uniformly distributed compensating ions of hydrogen-like acceptors; (ii) a semiconductor with uniformly distributed point t-defects in the charge states $(-1, 0, +1)$ and ions of hydrogen-like donors and acceptors.

It is shown that in the h-diode under the reverse bias ($U_r < 0$) for a cryogenic temperature, the region of the electric double layer between $|d1)$- and $|d2)$-regions cools down, and under the forward bias ($U_f > 0$) it heats up.

It is shown that in a Peltier element based on a semiconductor with triple-charged t-defects, upon current excitation, it is possible to cool down a metal–semiconductor contact under a negative electric potential and to heat up an opposite contact with a positive potential.

Acknowledgments

The work was supported by the Belarusian National Research Program "Materials Science, New Materials and Technologies".

References

1. Dresselhaus M.S., Chen G., Tang M.Y., Yang R., Lee H., Wang D., Ren Z., Fleurial J.-P., Gogna P. New directions for low-dimensional thermoelectric materials. *Adv. Mater.*, 2007, vol. 19, no. 8, pp. 1043–1053. **DOI:** 10.1002/adma.200600527

2. Shevelkov A.V. Chemical aspects of the design of thermoelectric materials. *Russ. Chem. Rev.*, 2008, vol. 77, no. 1, pp. 1–19. **DOI:** 10.1070/RC2008v077n01ABEH003746

3. Snarskii A.A., Zhenirovskii M.I., Bezsudnov I.V. Limiting values of the quality factor of thermoelectric composites. *Semiconductors*, 2008, vol. 42, no. 1, pp. 80–85. **DOI:** 10.1134/S1063782608010119

4. Dmitriev A.V., Zvyagin I.P. Current trends in the physics of thermoelectric materials. *Phys. Usp.*, 2010, vol. 53, no. 8, pp. 789–803. **DOI:** 10.3367/UFNe.0180.201008b.0821

5. Mani P., Nakpathomkun N., Hoffmann E.A., Linke H. A nanoscale standard for the Seebeck coefficient. *Nano Lett.*, 2011, vol. 11, no. 11, pp. 4679–4681. **DOI:** 10.1021/nl202258f

6. Upadhyaya M., Boyle C.J., Venkataraman D., Aksamija Z. Effects of disorder on thermoelectric properties of semiconducting polymers. *Sci. Rep.*, 2019, vol. 9, no. 1, pp. 5820(1–11). **DOI:** 10.1038/s41598-019-42265-z

7. Liu X., Wang Z. Printable thermoelectric materials and applications. *Front. Mater.*, 2019, vol. 6, pp. 88(1–5). **DOI:** 10.3389/fmats.2019.00088

8. Andreev A.G., Zabrodskii A.G., Egorov S.V., Zvyagin I.P. Thermopower of transmutation-doped Ge:Ga in the region for hopping conductivity. *Semiconductors*, 1997, vol. 31, no. 10, pp. 1008–1013. **DOI:** 10.1134/1.1187015

9. Andreev A.G., Zabrodskii A.G., Egorov S.V., Zvyagin I.P. Thermopower of neutron transmutation-doped Ge:Ga in the hopping region. Phys. *Status Solidi B*, 1998, vol. 205, no. 1, pp. 381–384. **DOI:** 10.1002/(SICI)1521-3951(199801)205:1<381::AID-PSSB381>3.0.CO;2-W

10. Poklonski N.A., Lopatin S.Yu. A lattice model of thermopower in hopping conduction: application to

neutron-doped crystalline germanium. *Phys. Solid State*, 2001, vol. 43, no. 12, pp. 2219–2228.
DOI: 10.1134/1.1427945

11. Ioffe A.F. Semiconductor Thermoelements and Thermoelectric Cooling. London, Infosearch, 1957, viii+184 p.

12. Nolas G.S., Sharp J., Goldsmid H.J. Thermoelectrics: Basic Principles and New Materials Developments. Berlin, Springer, 2001, viii+292 p.
DOI: 10.1007/978-3-662-04569-5

13. Handbook of Thermoelectrics: Macro to Nano, ed. by D.M. Rowe. Boca Raton, CRC Press, 2006, 1014 p. **DOI:** 10.1201/9781420038903

14. Sun P., Wei B., Zhang J., Tomczak J.M., Strydom A.M., Søndergaard M., Iversen B.B., Steglich F. Large Seebeck effect by charge-mobility engineering. *Nat. Commun.*, 2015, vol. 6, pp. 7475(1–9).
DOI: 10.1038/ncomms8475

15. Gurevich Yu.G., Logvinov G.N. Physics of thermoelectric cooling. *Semicond. Sci. Technol.*, 2005, vol. 20, no. 12, pp. R57–R64.
DOI: 10.1088/0268-1242/20/12/R01

16. Lu N., Li L., Liu M. A review of carrier thermoelectric-transport theory in organic semiconductors. *Phys. Chem. Chem. Phys.*, 2016, vol. 18, no. 29, pp. 19503–19525. **DOI:** 10.1039/C6CP02830F

17. Masood K.B., Kumar P., Singh R.A., Singh J. Odyssey of thermoelectric materials: foundation of the complex structure. *J. Phys. Commun.*, 2018, vol. 2, no. 6, pp. 062001(1–34). **DOI:** 10.1088/2399-6528/aab64f

18. Tomczak J.M. Thermoelectricity in correlated narrow-gap semiconductors. *J. Phys.: Condens. Matter*, 2018, vol. 30, no. 18, pp. 183001(1–70).
DOI: 10.1088/1361-648X/aab284

19. Recatala-Gomez J., Suwardi A., Nandhakumar I., Abutaha A., Hippalgaonkar K. Toward accelerated thermoelectric materials and process discovery. *ACS Appl. Energy Mater.*, 2020, vol. 3, no. 3, pp. 2240–2257.
DOI: 10.1021/acsaem.9b02222

20. DiSalvo F.J. Thermoelectric cooling and power generation. Science, 1999, vol. 285, no. 5428, pp. 703–706. **DOI:** 10.1126/science.285.5428.703

21. Vining C.B. Semiconductors are cool. *Nature*, 2001, vol. 413, no. 6856, pp. 577–578.
DOI: 10.1038/35098159

22. Stafeev V.I. Thermoelectric and other phenomena in structures with nonequilibrium charge carriers and nanoparticles. *Semiconductors*, 2009, vol. 43, no. 10, pp. 1280–1287. **DOI:** 10.1134/S1063782609100054

23. Blakemore J.S. Electron capture and emission for midgap centers. *J. Phys. Chem. Solids*, 1988, vol. 49, no. 6, pp. 627–631.
DOI: 10.1016/0022-3697(88)90193-X

24. Wilson A.H. Solid state physics 1925-33: opportunities missed and opportunities seized. *Proc. R. Soc. Lond. A*, 1980, vol. 371, no. 1744, pp. 39–48.
DOI: 10.1098/rspa.1980.0054

25. Shockley W. Electrons and Holes in Semiconductors with Applications to Transistor Electronics. Princeton, D. Van Nostrand Co., Inc., 1950, xxiv+558 p.

26. Ross I.M. The invention of the transistor. *Proc. IEEE.*, 1998, vol. 86, no. 1, pp. 7–28.
DOI: 10.1109/5.658752

27. Kilby J.S. Turning potential into reality: The invention of the integrated circuit, in Nobel Lectures, Physics 1996–2000, ed. G. Ekspong. Singapore, World Scientific, 2002, pp. 474–485. **DOI:** 10.1142/4973

28. Smith G.E. Nobel Lecture: The invention and early history of the CCD. *Rev. Mod. Phys.*, 2010, vol. 82, no. 3, pp. 2307–2312.
DOI: 10.1103/RevModPhys.82.2307

29. Boyle W.S. Nobel Lecture: CCD–An extension of man's view. *Rev. Mod. Phys.*, 2010, vol. 82, no. 3, pp. 2305–2306. **DOI:** 10.1103/RevModPhys.82.2305

30. Alferov Z.I. Nobel Lecture: The double heterostructure concept and its applications in physics, electronics, and technology. *Rev. Mod. Phys.*, 2001, vol. 73, no. 3, pp. 767–782. **DOI:** 10.1103/RevModPhys.73.767

31. Kroemer H. Nobel Lecture: Quasielectric fields and band offsets: teaching electrons new tricks. *Rev. Mod. Phys.*, 2001, vol. 73, no. 3, pp. 783–793.
DOI: 10.1103/RevModPhys.73.783

32. Seebauer E.G., Kratzer M.C. Charged point defects in semiconductors. *Mater. Sci. Eng. R*, 2006, vol. 55, no. 3–6, pp. 57–149.
DOI: 10.1016/j.mser.2006.01.002

33. Zhang Y. Electronic structures of impurities and point defects in semiconductors. *Chin. Phys. B*, 2018, vol. 27, no. 11, pp. 117103(1–14).
DOI: 10.1088/1674-1056/27/11/117103

34. Oyama K., Ri S.-G., Kato H., Takeuchi D., Makino T., Ogura M., Tokuda N., Okushi H., Yamasaki S. Carrier transport of diamond p^+-i-n^+ junction diode fabricated using low-resistance hopping p^+ and n^+ layers. *Phys. Status Solidi A*, 2011, vol. 208, no. 4, pp. 937–942.
DOI: 10.1002/pssa.201026490

35. Poklonski N.A., Vyrko S.A., Poklonskaya O.N., Kovalev A.I., Zabrodskii A.G. Ionization equilibrium at the transition from valence-band to acceptor-band migration of holes in boron-doped diamond. *J. Appl. Phys.*, 2016, vol. 119, no. 24, pp. 245701(1–10).
DOI: 10.1063/1.4954281

36. Bulyarskii S.V., Svetukhin V.V., L'vov P.E. Thermodynamics of complex formation and defect clustering in semiconductors. *Semiconductors*, 2000, vol. 34, no. 4, pp. 371–375. **DOI:** 10.1134/1.1187990

37. Coates R., Mitchell E.W.J. The optical and electrical effects of high concentrations of defects in irradiated crystalline gallium arsenide. *Adv. Phys.*, 1975, vol. 24, no. 5, pp. 593–644.
DOI: 10.1080/00018737500101471

38. Radiation Effects in Semiconductors, ed. by K. Iniewski. Boca Raton, CRC Press, 2011. xvi+415 p.
DOI: 10.1201/9781315217864

39. Brudnyi V.N. Charge neutrality in semiconductors: defects, interfaces, surface. *Russ. Phys. J.*, 2013, vol. 56, no. 7, pp. 754–756.
DOI: 10.1007/s11182-013-0095-4

40. Aronov D.A., Knigin P.I., Korolev Yu.S., Rubinov V.V. Exclusion effect in semiconductors with non-injecting contacts. *Phys. Status Solidi A*, 1984, vol. 81, no. 1, pp. 11–45. **DOI:** 10.1002/pssa.2210810102

41. Blank T.V., Gol'dberg Y.A. Mechanisms of current flow in metal–semiconductor ohmic contacts. Semiconductors, 2007, vol. 41, no. 11, pp. 1263–1292. **DOI:** 10.1134/S1063782607110012

42. Poklonski N.A., Kovalev A.I., Gorbachuk N.I., Shpakovski S.V. [Calculation of static parameters of silicon diode containing δ-layer of point triple-charged defects in symmetric *p–n*-junction]. *Devices and Methods of Measurements*, 2018, vol. 9, no. 2, pp. 130–141 (in Russian). **DOI:** 10.21122/2220-9506-2018-9-2-130-141

43. Madelung O. Semiconductors: Data Handbook. Berlin, Springer, 2004, xiv+692 p. **DOI:** 10.1007/978-3-642-18865-7

44. Poklonski N.A., Vyrko S.A., Zabrodskii A.G. Electrostatic models of insulator–metal and metal–insulator concentration phase transitions in Ge and Si crystals doped by hydrogen-like impurities. *Phys. Solid State*, 2004, vol. 46, no. 6, pp. 1101–1106. **DOI:** 10.1134/1.1767252

45. Poklonski N.A., Stelmakh V.F. Screening of electrostatic fields in crystalline semiconductors by electrons hopping over defects. *Phys. Status Solidi B*, 1983, vol. 117, no. 1, pp. 93–99. **DOI:** 10.1002/pssb.2220880266

46. Poklonski N.A., Vyrko S.A., Poklonskaya O.N., Zabrodskii A.G. Transition temperature from band to hopping direct current conduction in crystalline semiconductors with hydrogen-like impurities: Heat versus Coulomb attraction. *J. Appl. Phys.*, 2011, vol. 110, no. 12, pp. 123702(1–7). **DOI:** 10.1063/1.3667287

47. Poklonski N.A., Vyrko S.A., Dzeraviaha A.N. Thermal ionization energy of hydrogen-like impurities in semiconductor materials. *Journal of the Belarusian State University. Physics*, 2020, no. 2, pp. 28–41 (in Russian). **DOI:** 10.33581/2520-2243-2020-2-28-41

48. Kuz'min L.S. Supersensitive cold-electron bolometers in studies of dark matter and dark energy. *Phys. Usp.*, 2005, vol. 48, no. 5, pp. 519–525. **DOI:** 10.1070/PU2005v048n05ABEH002128

49. Rogalski A. Progress in focal plane array technologies. *Prog. Quant. Electron.*, 2012, vol. 36, no. 2–3, pp. 342–473. **DOI:** 10.1016/j.pquantelec.2012.07.001

50. Kiselev V.A. Covalent–ionic transition, and activity of metal–semiconductor interfaces. *Sov. Phys. Solid State*, 1991, vol. 33, no. 10, pp. 3070–3076.

51. McPherson M. Fermi level pinning in irradiated silicon considered as a relaxation-like semiconductor. *Physica B*, 2004, vol. 344, no. 1–4, pp. 52–57. **DOI:** 10.1016/j.physb.2003.07.006

52. Poklonski N.A., Vyrko S.A., Zabrodskii A.G. Field effect and capacitance of silicon crystals with hopping conductivity over point radiation defects pinning the Fermi level. *Semiconductors*, 2007, vol. 41, no. 11, pp. 1300–1306. **DOI:** 10.1134/S1063782607110048

53. Poklonski N.A. Disordered semiconductor materials. Int. Winter School on Semiconductor Physics 2019: Scientific Programme and Abstracts, St. Petersburg – Zelenogorsk, Feb. 28–Mar. 4, 2019, SPb., Ioffe Institute, 2019, pp. 40–44 (in Russian).

54. Mott N. The mobility edge since 1967. *J. Phys. C: Solid State Phys.*, 1987, vol. 20, no. 21, pp. 3075–3102. **DOI:** 10.1088/0022-3719/20/21/008

55. Kozub V.I., Rudin A.M. Transport of nonequilibrium phonons in disordered systems (review). *Phys. Solid State*, 1996, vol. 38, no. 2, pp. 189–208.

56. Smolyakov B.P., Khaimovich E.P. Dynamic processes in dielectric glasses at low temperatures. *Sov. Phys. Usp.*, 1982, vol. 25, no. 2, pp. 102–115. **DOI:** 10.1070/PU1982v025n02ABEH004500

Фемтосекундная лазерная система с импульсной накачкой генератора и усилителя при использовании одного силового блока

С.А. Тихомиров

Институт физики имени Б.И. Степанова Национальной академии наук Беларуси,
пр-т Независимости, 68, Минск 220072, Беларусь

Поступила 28.01.2021
Принята к печати 01.03.2021

Уже на протяжении нескольких десятилетий развитие методов генерации сверхкоротких импульсов является самостоятельной актуальной научно-технической задачей. Идёт постоянное совершенствование как способов получения импульсов, так и методов их использования. Целью данной работы являлось исследование возможности реализации согласованной работы двух принципиально разных типов лазеров накачки фемтосекундного генератора и усилителя на одном одноламповом квантроне и создание на этой основе компактной мощной фемтосекундной лазерной системы с импульсной накачкой и одним силовым блоком.

Осуществлена практическая реализация на одном квантроне с двумя активными элементами и одной лампой накачки двух типов импульсных лазеров (нано- и пикосекундного, работающих, соответственно, в режиме модулированной добротности и синхронизации мод). Получены требуемая синхронизация во времени момента формирования импульса накачки фемтосекундного усилителя и области квазистационарной генерации импульсов в выходном излучении фемтосекундного Ti:сапфирового генератора и необходимые взаимосогласованные энергетические параметры выходного излучения лазеров накачки фемтосекундного генератора и усилителя.

На этой основе разработана компактная импульсная моноблочная лазерная система, способная обеспечить генерацию фемтосекундных импульсов длительностью 50–150 фс с энергией до 1 мДж и достаточно высокой частотой повторения импульсов (вплоть до 1 кГц, что определяется типом используемых квантрона и блока накачки). В лазерной системе использована компактная совмещённая схема стретчера-компрессора с одной общей дифракционной решёткой.

Лазерные системы подобного типа, характеризуемые относительно низкой стоимостью за счёт использования одного силового блока питания для одновременной накачки усилителя и генератора, а также более низкими требованиями к качеству оптических элементов и условиям эксплуатации благодаря импульсному режиму работы, представляются достаточно практичными. Они могут найти применение как в научных исследованиях в области сверхскоростной кинетической спектроскопии и нелинейной оптике, так и в многочисленных технических приложениях, в частности в прецизионной обработке материалов, как оптические имитаторы воздействия тяжёлых заряженных частиц при проведении испытаний радиационной стойкости интегральных микросхем и электронных модулей.

Ключевые слова: фемтосекундные лазеры, импульсная синхронная накачка, гибридная синхронизация мод.

DOI: 10.21122/2220-9506-2021-12-1-23-29

Адрес для переписки:
Тихомиров С.А.
Институт физики имени Б.И. Степанова НАН Беларуси,
пр-т Независимости, 68, Минск 220072, Беларусь
e-mail: s.tik@ifanbel.bas-net.by

Address for correspondence:
Tikhomirov S.A.
B.I. Stepanov Institute of Physics of the National Academy of Sciences of Belarus,
Nezavisimosty Ave., 68, Minsk 220072, Belarus
e-mail: s.tik@ifanbel.bas-net.by

Для цитирования:
С.А. Тихомиров.
Фемтосекундная лазерная система с импульсной накачкой генератора и усилителя при использовании одного силового блока.
Приборы и методы измерений.
2020. – Т. 11, № 4. – С. 23–29.
DOI: 10.21122/2220-9506-2020-11-4-23-29

For citation:
S.A. Tikhomirov.
[Femtosecond System with Pulse Pumping of Seed Laser and Amplifier by Using a Single Power Unit].
Devices and Methods of Measurements.
2020, vol. 11, no. 4, pp. 23–29 (in Russian).
DOI: 10.21122/2220-9506-2020-11-4-23-29

Femtosecond System with Pulse Pumping of Seed Laser and Amplifier by Using a Single Power Unit

S.A. Tikhomirov

*B.I. Stepanov Institute of Physics of the National Academy of Sciences of Belarus,
Nezavisimosty Ave., 68, Minsk 220072, Belarus*

Received 28.01.2021
Accepted for publication 01.03.2021

Abstract

For several decades development of methods for generating ultrashort pulses has been an independent urgent scientific and technical problem. There is a constant improvement both in the methods of such pulses receiving and in methods of their use. The aim of this work was to investigate the possibility of realizing the coordinated operation of two fundamentally different types of pump lasers for the femtosecond oscillator and amplifier based on one single-lamp laser head and to create on this basis a compact high-power femtosecond system with pulsed pumping and one power unit.

The practical implementation of two types of pulsed lasers (nano- and picosecond ones operating, respectively, in Q-switch and modelock regime) on a single laser head with two active elements and one pump lamp is carried out. The required synchronization in time the pump pulse femtosecond amplifier formation and quasi-stationary region of generated pulses in the output radiation of a femtosecond Ti:sapphire is obtained.

On this basis a compact, pulse pumped monoblock laser system has been developed that can generate femtosecond pulses with a duration of 50–150 fs with an energy up to 1 mJ and a high enough pulse repetition rate (up to 1 kHz which is determined by the type of laser head and pump unit used). In the developed laser system a compact scheme of a stretcher-compressor with a single common diffraction grating is used.

Laser systems of this type characterized by a relatively low cost due to the use of a single power supply unit for simultaneous pumping of the amplifier and oscillator, as well as lower requirements for the quality of optical elements and usage conditions due to the pulse mode of operation, are quite practical and can be used both in scientific research in the field of ultra-high-speed kinetic spectroscopy and nonlinear optics, as well as in numerous technical applications, particular in the precision processing of materials, as optical simulators of the action of heavy charged particles in testing the radiation resistance of integrated circuits and electronic modules.

Keywords: femtosecond lasers, pulsed synchronous pumping, hybrid modelocking.

DOI: 10.21122/2220-9506-2021-12-1-23-29

Адрес для переписки:
Тихомиров С.А.
Институт физики имени Б.И. Степанова НАН Беларуси,
пр-т Независимости, 68, Минск 220072, Беларусь
e-mail: s.tik@ifanbel.bas-net.by

Address for correspondence:
Tikhomirov S.A.
B.I. Stepanov Institute of Physics of the National Academy of Sciences of Belarus,
Nezavisimosty Ave., 68, Minsk 220072, Belarus
e-mail: s.tik@ifanbel.bas-net.by

Для цитирования:
С.А. Тихомиров.
Фемтосекундная лазерная система с импульсной накачкой генератора и усилителя при использовании одного силового блока.
Приборы и методы измерений.
2020. – Т. 11, № 4. – С. 23–29.
DOI: 10.21122/2220-9506-2020-11-4-23-29

For citation:
S.A. Tikhomirov.
[Femtosecond System with Pulse Pumping of Seed Laser and Amplifier by Using a Single Power Unit].
Devices and Methods of Measurements.
2020, vol. 11, no. 4, pp. 23–29 (in Russian).
DOI: 10.21122/2220-9506-2020-11-4-23-29

Введение

В настоящее время фемтосекундные лазеры широко используются как для научных исследований, так и в сфере технологий. Задающий генератор практически всех современных фемтосекундных систем обычно представляет собой полностью твердотельный (волоконный) непрерывно накачиваемый лазер [1–7]. Для накачки используются либо непрерывные твердотельные лазеры, либо прямая диодная накачка. Существует также, реализованный нами [8], метод генерации фемтосекундных импульсов при синхронной накачке титан-сапфирового лазера второй гармоникой импульсного Nd:YAG лазера с гибридной синхронизацией мод. На основе данного оригинального генератора фемтосекундных импульсов был создан фемтосекундный спектрометр [9], успешно эксплуатируемый в Институте физики НАН Беларуси уже на протяжении достаточно длительного времени. Система характеризуется относительно низкой стоимостью, естественной совместимостью генератора и усилителя, работающих в импульсном режиме с одинаковой частотой повторения, простотой в обслуживании.

Во всех предыдущих схемах реализации метода использовались два независимых импульсных Nd:YAG лазера: пикосекундный лазер с гибридной синхронизацией мод для синхронной накачки фемтосекундного титан-сапфирового генератора и моноимпульсный, работающий в режиме модуляции добротности и генерирующий наносекундные импульсы для накачки фемтосекундного усилителя. В то же время привлекательной представлялась идея организации работы двух принципиально разных типов лазеров на одном квантроне с двумя активными элементами и одной лампой накачки. В виду различных режимов работы данных лазеров и необходимости при этом одновременно обеспечить согласованные амплитудные и временные параметры генерируемых ими импульсов с требуемой синхронизацией во времени это являлось самостоятельной задачей, требующей экспериментальной проверки возможности её решения. В случае положительного результата предоставлялась возможность существенно упростить всю систему, снизить стоимость и, соответственно, повысить коммерческую привлекательность данного метода генерации фемтосекундных импульсов. Конечной целью работы было создание на этом принципе фемтосекундной лазерной системы.

Основная часть

На рисунке 1 приведена оптическая схема разработанной фемтосекундной лазерной системы. В квантроне размещены два активных цилиндрических элемента (Nd:YAG), одновременно накачиваемые одной импульсной лампой. В состав лазера накачки (II) фемтосекундного генератора входит активный элемент с размерами 5×60 мм, 2 плоских «глухих» зеркала, линза (f = 14 см), размещённая перед концевым глухим зеркалом, электронно-оптическая схема отрицательной обратной связи, выходное зеркало на клиновой подложке с коэффициентом отражения 35 %, а также зеркало с насыщающимся поглотителем (*SESAM*), обеспечивающее совместно с электрооптическим затвором гибридную синхронизацию мод. Общая база резонатора ≈ 150 см. Линза устанавливается таким образом, чтобы обеспечить работу лазера вблизи внешней границы области стабильности на нулевой поперечной моде. Изменяя положение зеркала *SESAM* вдоль оси резонатора, можно регулировать интенсивность внутрирезонаторного поля в области насыщающего поглотителя. Оптимальное положение данного зеркала подбирается экспериментально.

Ключевую роль в обеспечении требуемого режима генерации играет электрооптическая отрицательная обратная связь (ООС). Она образована поляризатором, электрооптическим кристаллом и электронной схемой с быстрым фотодиодом. Обратная связь вносит потери, пропорциональные световому полю внутри резонатора. В результате интенсивность поля внутри активной среды ограничивается на заданном уровне. Запасённая инверсия расходуется за более длительное время, в течение которого происходит дополнительная подкачка инверсии населённости в активном кристалле. В результате, время непрерывной генерации увеличивается до требуемых 50–80 мкс, причём данное время легко регулируется глубиной обратной связи. Вторая функция ООС – регенеративная синхронизация мод. Поскольку ООС срабатывает на периодический сигнал внутри резонатора (шумовой выброс), она создаёт потери с периодом, равным времени обхода по резонатору. Для обеспечения синхронизации мод необходимо, чтобы воздействие обратной связи происходило в нужной фазе, что достигается либо подбором длины резонатора, либо изменением задержки прихода оптического сигнала на фотодиод. Длительность импульсов, полученных с помощью регенеративной синхронизации мод, составляет несколько сотен пикосекунд. Нелинейный фильтр позволяет сократить длительность генерируемых импульсов до десятков пикосекунд и повысить эффективность преобразования излучения во вторую гармонику.

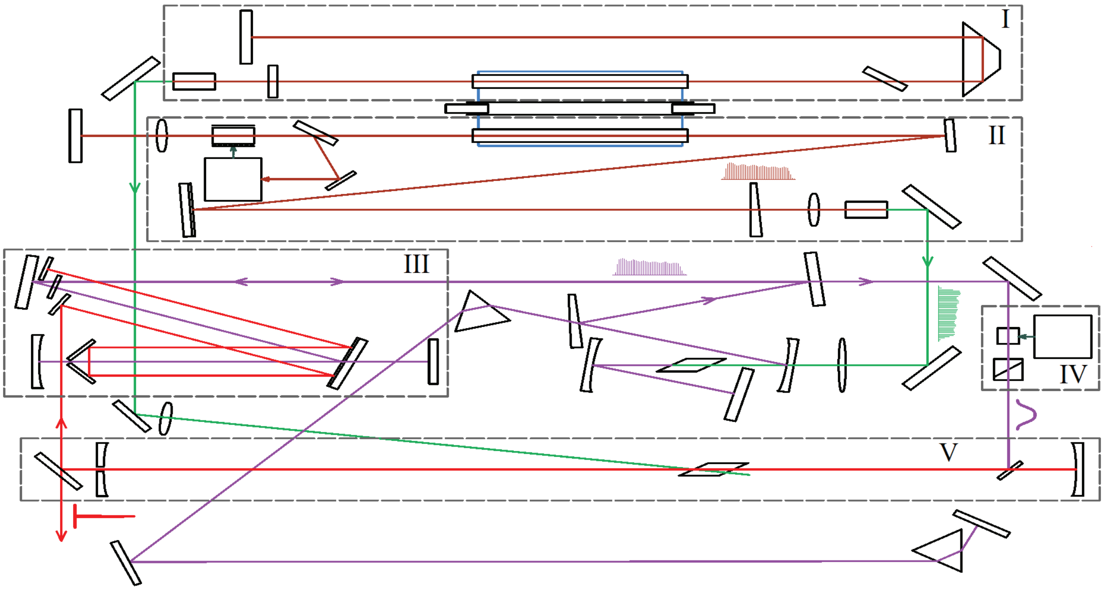

Рисунок 1 – Оптическая схема фемтосекундной лазерной системы: I – наносекундный лазер накачки усилителя; II – пикосекундный лазер накачки фемтосекундного генератора; III – стретчер-компрессор; IV – схема выделения одиночного импульса; V – многопроходный усилитель

Figure 1 – Optical scheme of a femtosecond laser system: I – nanosecond pump laser of the amplifier; II – picosecond pump laser of the femtosecond generator; III – stretcher-compressor scheme; IV – single pulse extraction circuit; V – multi-pass amplifier

С оптимизированными параметрами резонатора, обратной связи и накачки Nd:YAG лазер генерирует высокостабильные цуги пикосекундных импульсов на длине волны 1,054 мкм общей длительностью до 60 мкс и энергией порядка 3 мДж, способные обеспечить энергию второй гармоники в цуге (рисунок 2*a*), оптимальную для синхронной накачки фемтосекундного генератора. Частота повторения циклов генерации составляла 10 Гц.

Резонатор фемтосекундного генератора образован четырьмя плоскими и двумя сферическими высокоотражающими в спектральной области 740–840 нм зеркалами. Квазисолитонный механизм формирования фемтосекундных импульсов обеспечивается призменной парой, создающей необходимую отрицательную дисперсию групповой скорости. Для эффективности синхронной накачки резонатор сделан сильно несимметричным. Наиболее оптимальные условия для генерации фемтосекундных импульсов создаются при работе на внешнем краю зоны стабильности. При таких параметрах резонатора наблюдается старт керровского механизма синхронизации мод и стабильная генерация фемтосекундных импульсов в квазистационарном режиме во временном диапазоне порядка 40 мкс (рисунок 2*b*). Вывод излучения из резонатора осуществляется с помощью тонкой клиновой подложки.

В разработанной лазерной системе в сравнении с ранними реализациями метода использована компактная схема стретчера-компрессора фемтосекундных импульсов с одной общей дифракционной решёткой, при этом при разводке лучей в стретчере используется верхняя половина решётки, а в компрессоре – нижняя (рисунок 1, III). Таким образом, все элементы компрессора расположены ниже элементов стретчера. Кроме того, по горизонтали стретчер и компрессор также использует разные части решётки: стретчер – центральную, компрессор – боковые. В результате удаётся разместить на одной площадке оба устройства, так, чтобы их оптомеханические узлы не мешали друг другу. Благодаря такой компоновке, во-первых, экономится пространство.

Во-вторых, экономятся финансовые ресурсы, так как необходим один комплект дифракционной решётки и оптомеханического крепления к ней вместо двух. Кроме того, за счёт использования одной решётки автоматически решается задача согласования решёток стретчера и компрессора.

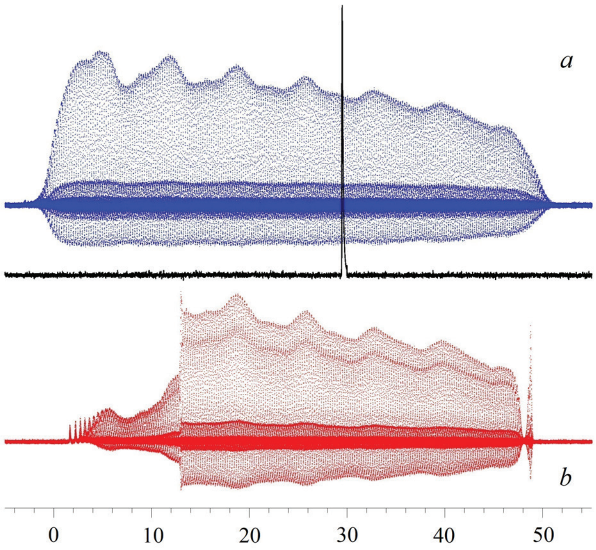

Рисунок 2 – Осциллограммы излучения второй гармоники пикосекундного лазера (*a*) и излучения синхронно накачиваемого титан-сапфирового лазера в режиме генерации фемтосекундных импульсов (*b*). Чёрная линия – осциллограмма импульса второй гармоники наносекундного лазера на гранате, накачивающей титан сапфировый усилитель

Figure 2 – Oscillograms of the second harmonic radiation of a picosecond laser (*a*) and the radiation of a synchronously pumped titanium-sapphire laser in the femtosecond pulse generation operating mode (*b*). The black line is the oscillogram of the second harmonic pulse of a nanosecond Nd:YAG laser pumping the titanium sapphire amplifier

Накачка активной среды усилителя производится излучением второй гармоники наносекундного лазера (рисунок 1, I), сформированного по стандартной схеме на втором активном элемент Nd:YAG размером 6×60, размещённом в том же квантроне, что и активный элемент пикосекундного лазера. Принципиальной задачей является синхронизация времени формирования импульса накачки усилителя с областью устойчивой генерации фемтосекундных импульсов, из которой происходит выделение усиливаемого импульса, т. е. обеспечение подачи усиливаемого импульса в многопроходный усилитель в момент создания максимальной инверсии населённости в активном элементе, создаваемой наносекундным импульсом второй гармоники гранатового лазера. Основной возможностью осуществления такой синхронизации в нашем варианте является варьирование (уменьшение) добротности резонатора пикосекундного лазера, поскольку процесс синхронизации мод и формирования ультракоротких импульсов существенно (десятки микросекунд) в обычных условиях опережает формирование наносекундного импульса в лазере с модулированной добротностью. Для обеспечения необходимого уровня добротности использовалась плавная отстройка электрооптического кристалла ООС путём регулировки степени отклонения отражения юстировочного лазера от грани кристалла по биссектрисе прямого угла в рабочей четверти. Как оказалось, данная операция, помимо решения основной задачи – получения требуемой синхронизации во времени импульса накачки усилителя и усиливаемого фемтосекундного импульса, способствует работе всей системы отрицательной обратной связи в наиболее благоприятном линейном режиме.

На рисунке 2 приведены соответствующие осциллограммы, иллюстрирующие обеспечение требуемого согласования во времени участка квазистационарной генерации фемтосекундных импульсов и сформированного импульса накачки фемтосекундного усилителя. Область резкого увеличения амплитуды генерации на осциллограмме соответствует старту и установлению процесса синхронизации мод за счёт керровской линзы и квазисоллитонного механизма.

После стретчера и схемы выделения (IV) одиночный импульс из области цуга, примерно соответствующей по положению центру участка квазистационарной генерации фемтосекундных импульсов, направляется в многопроходный усилитель (V), в котором организовано 10 проходов усиливаемого импульса через активную среду (титан-сапфировый кристалл). На рисунке 3 приведена фотография разводки лучей поступающего в усилитель излучения на выходном сферическом зеркале многопроходного усилителя. Десятый луч проходит через отверстие в зеркале.

В результате 10 разведенных в вертикальной плоскости проходов через область активной среды, накачиваемую наносекундным импульсом второй гармоники лазера на гранате с энергией порядка 7 мДж, импульс усиливается более чем в 10^6 раз и направляется в компрессор, собранный на той же дифракционной решётке, что и стретчер. На выходе компрессора получаем одиночный фемтосекундный импульс с энергией до 1 мДж и задаваемой частотой повторения, определяемой типом используемого силового блока.

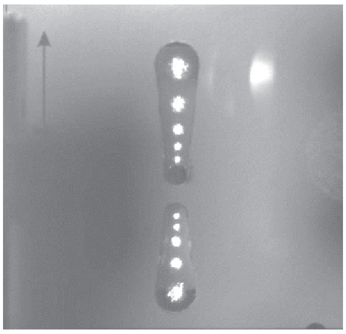

Рисунок 3 – Разводка лучей усиливаемого импульса титан-сапфирового лазера на выходном зеркале усилителя

Figure 3 – Distribution of the beams of the amplified pulse of a titanium-sapphire laser on the output mirror of the amplifier

На рисунке 4 представлен спектр и автокорреляционная функция усиленного импульса.

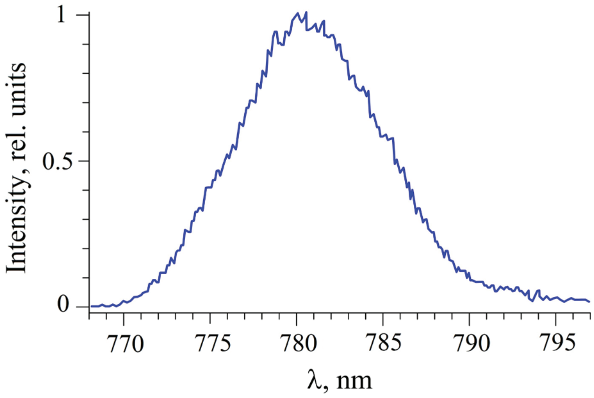

a

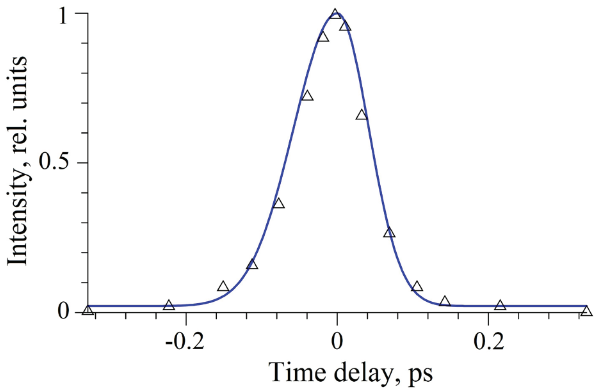

b

Рисунок 4 – Спектр (*a*) и автокореляционная функция (*b*) усиленного фемтосекундного импульса

Figure 4 – Spectrum (*a*) and autocorrelation function (*b*) of the amplified femtosecond pulse

Длительность сжатого импульса составила порядка 70 фс при ширине спектра на полувысоте 10 нм.

Заключение

Разработана компактная моноблочная лазерная система, способная обеспечить генерацию фемтосекундных импульсов длительностью 50–150 фс с энергией до 1 мДж и достаточно высокой частотой повторения импульсов (вплоть до 1 кГц, что определяется типом используемых квантрона и блока накачки). Имеется возможность оперативной перестройки основной частоты в спектральном диапазоне 760–830 нм.

Фемтосекундные лазерные системы подобного типа, характеризуемые относительно низкой стоимостью за счёт использования одного силового блока питания для одновременной накачки усилителя и генератора, а также более низкими требованиями к качеству оптических элементов и условиям эксплуатации вследствие импульсного режима работы, представляются достаточно практичными. Они могут найти применение как в научных исследованиях в области сверхскоростной кинетической спектроскопии и нелинейной оптики, так и в многочисленных технических приложениях, в частности в прецизионной обработке материалов, как оптические имитаторы воздействия тяжелых заряженных частиц при проведении испытаний радиационной стойкости интегральных микросхем и электронных модулей и др.

Список использованных источников

1. *Keller U.* Recent developments in compact ultrafast lasers / *U. Keller* // Nature. – 2003. – Vol. 424(6950). – Pp. 831–838.

2. *Крюков П.Г.* Лазеры ультракоротких импульсов / П.Г. Крюков // Квантовая электроника. – 2001. – Т. 31. – С. 95–119.

3. *Spence D.E., Kean P.N., Sibbett W.* 60-fsec pulse generation from a self-mode-locked Ti:sapphire laser / D.E. Spence, P.N. Kean, W. Sibbett // Opt. Lett. – 1991. – Vol. 16, iss. 1. – Pp. 42–44.
DOI: 10.1364/OL.16.000042

4. *Ell R.* Generation of 5-fs pulses and octave-spanning spectra directly from a Ti:sapphire laser / R. Ell [et al.] // Opt. Lett. – 2001. – Vol. 26, iss. 6. – Pp. 373–375. **DOI:** 10.1364/OL.26.000373

5. *Kisel V.E.* Femtosecond pulse generation with a diode-pumped Yb^{3+}:YVO_4 laser / V.E. Kisel [et al.] // Opt.

Lett. – 2005. – Vol. 30, iss. 10. – Pp. 1150–1152.
DOI: 10.1364/OL.30.001150

6. *Gürel K.* Green-diode-pumped femtosecond Ti:sapphire laser with up to 450 mW average power / K. Gürel [et al.] // Optics express. – 2015. – Vol. 23, no. 23. – Pp. 30043–30048. **DOI:** 10.1364/OE.23.030043

7. *Sell A.* 8-fs pulses from a compact Er:fiber system: quantitative modeling and experimental implementation / A. Sell [et al.] // Opt. Exp. – 2009. – Vol. 17. – P. 10.

8. *Борисевич Н.А.* Квантовая электроника / Н.А. Борисевич [и др.]. – 1999. – Т. 28, № 3. – С. 225–231.

9. *Stsiapura V.I.* Charge transfer process determines ultrafast excited state deactivation of thioflavin T in low-viscosity solvents / V.I. Stsiapura [et al.] // J. Phys. Chem. A. – 2010. – Vol. 114, no. 32. – Pp. 8345−8350. **DOI:** 10.1021/jp105186z

References

1. Keller U. Recent developments in compact ultrafast lasers. *Nature*, 2003, vol. 424, pp. 831–838.

2. Kryukov P.G. [Ultrashort pulse lasers]. *Kvantovaya elektronika* [Quantum Electronics], 2001, vol. 31, no. 2, pp. 95–119 (in Russian).

3. Spence D.E., Kean P.N., Sibbett W. 60-fsec pulse generation from a self-mode-locked Ti:sapphire laser. *Optics Letters*, 1991, vol. 16, iss. 1, pp. 42–44.
DOI: 10.1364/OL.16.000042

4. Ell R., Morgner U., Kärtner F.X., Fujimoto J.G., Ippen E.P., Scheuer V., Angelow G., Tschudi T. Lederer M.J., Boiko A., Luther-Davies B. Generation of 5-fs pulses and octave-spanning spectra directly from a Ti:sapphire laser. *Optics Letters*, 2001, vol. 26, iss. 6, pp. 373–375. **DOI:** 10.1364/OL.26.000373

5. Kisel V.E., Troshin A.E., Shcherbitsky V.G., Kuleshov N.V., Matrosov V.N., Matrosova T.A., Kupchenko M.I., Brunner F., Paschotta R., Morier-Genoud F., Keller U. Femtosecond pulse generation with a diode-pumped Yb^{3+}:YVO_4 laser. *Optics Letters*, 2005, vol. 30, iss. 10, pp. 1150–1152. **DOI:** 10.1364/OL.30.001150

6. Gürel K., Wittwer V.J., Hoffmann M., Saraceno C.J., Hakobyan S., Resan B., Südmeyer T. Green-diode-pumped femtosecond Ti:sapphire laser with up to 450 mW average power. *Optics express*, 2015, vol. 23, iss. 23, pp. 30043–30048.
DOI: 10.1364/OE.23.030043

7. Sell A., Krauss G., Scheu R., Huber R., Leitenstorfer A. 8-fs pulses from a compact Er:fiber system: quantitative modeling and experimental implementation. *Optics express*, 2009, vol. 17, iss. 2, pp. 1070–1077.

8. Borisevich N.A., Buganov O.V., Tikhomirov S.A., Tolstorozhev G.B., Shkred G.L. [Passive mode locking of a femtosecond Ti:sapphire laser with pulsed synchronous pumping by a limited train of picosecond pulses]. *Kvantovaya elektronika* [Quantum Electronics], 1999, vol. 28, no. 3, pp. 225–231 (in Russian).

9. Stsiapura V.I., Maskevich A.A., Tikhomirov S.A., Buganov O.V. Charge transfer process determines ultrafast excited state deactivation of thioflavin T in low-viscosity solvents. *J. Phys. Chem. A*., 2010, vol. 114, no. 32, pp. 8345−8350. **DOI:** 10.1021/jp105186z

Optimization of the Emitting Coil of a Hardware-Software Complex for Study of Low-Frequency Electromagnetic Radiation's Shielding Effectiveness

O.D. Kanafyev[1], A.V. Trukhanov[1], T.I. Zubar[1], S.A. Chizhik[2], S.S. Grabchikov[1]

[1]Scientific and Practical Materials Research Center of the National Academy of Sciences of Belarus, P. Brovki str., 19, Minsk 220072, Belarus

[2]National Academy of Sciences of Belarus, Nezavisimosty Ave., 66, Minsk 220072, Belarus

Received 14.12.2020
Accepted for publication 22.02.2021

Abstract

Optimization of the radiation coil of the hardware-software complex for studying the effectiveness of shielding of low-frequency electromagnetic radiation will make it possible to assess the effectiveness of shielding coatings at a higher level. This fact will make it possible to develop coatings with improved characteristics. The purpose of this work was to determine the optimal characteristics of the emitting coil which will ensure its stable operation and magnetic field strength in the frequency range up to 100 kHz.

The parameters of the manufactured samples, such as inductance (L), active (R) and total resistance (Z), were obtained using an *MNIPI E*7-20 emittance meter. In practice, the coils with the optimal parameters calculated theoretically were connected to a current source and amplifier. To detect electromagnetic radiation, a multilayer inductor connected to a *UTB-TREND* 722-050-5 oscilloscope was used as a signal receiver.

The results of measurements showed that the resistance of multilayer coils is approximately 1000 times higher than that of single-layer coils. Also, for multilayer coils, an avalanche-like increase in total resistance is observed starting from a frequency of 10 kHz, while for single-layer coils there is a uniform increase in total resistance over the entire frequency range up to 100 kHz.

The paper presents results of research on the correlation of the performance of single-layer and multilayer inductors depending on their parameters in the frequency range from 20 Hz to 100 kHz. Values of the voltage required to provide the magnetic field strength of 1, 5, 20 Oe at 25 Hz and 100 kHz have been calculated. After analyzing the data obtained, the optimal parameters of the inductor were found which ensure stable performance in the frequency range up to 100 kHz.

Keywords: inductor coil, shielding, electromagnetic emitting.

DOI: 10.21122/2220-9506-2021-12-1-30-37

Адрес для переписки:
Канафьев О.Д.
НПЦ НАН Беларуси по материаловедению,
ул. П. Бровки, 19, г. Минск 220072, Беларусь
e-mail: olegkan96@mail.ru

Address for correspondence:
Kanafyev O.D.
Scientific and Practical Materials Research Center of the National Academy of Sciences of Belarus,
P. Brovki str., 19, Minsk 220072, Belarus
e-mail: olegkan96@mail.ru

Для цитирования:
O.D. Kanafyev, A.V. Trukhanov, T.I. Zubar, S.A. Chizhik, S.S. Grabchikov.
Optimization of the Emitting Coil of a Hardware-Software Complex for Study of Low-Frequency Electromagnetic Radiation's Shielding Effectiveness.
Приборы и методы измерений.
2021. – Т. 12, № 1. – С. 30–37.
DOI: 10.21122/2220-9506-2021-12-1-30-37

For citation:
O.D. Kanafyev, A.V. Trukhanov, T.I. Zubar, S.A. Chizhik, S.S. Grabchikov.
Optimization of the Emitting Coil of a Hardware-Software Complex for Study of Low-Frequency Electromagnetic Radiation's Shielding Effectiveness.
Devices and Methods of Measurements.
2021, vol. 12, no. 1, pp. 30–37.
DOI: 10.21122/2220-9506-2021-12-1-30-37

Devices and Methods of Measurements
2021, vol. 12, no. 1, pp. 30–37
O.D. Kanafyev et al.

Оптимизация излучающей катушки программно-аппаратного комплекса для исследования эффективности экранирования низкочастотного электромагнитного излучения

О.Д. Канафьев[1], А.В. Труханов[1], Т.И. Зубарь[1], С.А.Чижик[2], С.С. Грабчиков[1]

[1]Научно-практический центр Национальной академии наук Беларуси по материаловедению, ул. П. Бровки, 19, г. Минск 220072, Беларусь

[2]Национальная Академия наук Беларуси, пр-т Независимости, 66, г. Минск 220072, Беларусь

Поступила 14.12.2020
Принята к печати 22.02.2021

Оптимизация излучающей катушки программно-аппаратного комплекса для исследования эффективности экранирования низкочастотного электромагнитного излучения позволит на более качественном уровне оценивать эффективность экранирующих покрытий. Данный факт даст возможность разрабатывать покрытия с улучшенными характеристиками. Целью данной работы являлось определение оптимальных характеристик излучающей катушки, которые обеспечат её стабильную работу и напряжённость магнитного поля в частотном диапазоне до 100 кГц.

Параметры изготовленных образцов, такие как индуктивность, активное и общее сопротивление, были получены, используя измеритель иммитанса МНИПИ Е7-20. На практике катушки с оптимальными параметрами, вычисленными теоретически, были подключены к источнику и усилителю тока. Для детектирования электромагнитного излучения в качестве приёмника сигнала использовалась многослойная катушка индуктивности, подключённая к осциллографу *UTB- TREND* 722-050-5.

Результаты измерений показали, что сопротивление многослойных катушек приблизительно в 1000 раз больше сопротивления однослойных. Также у многослойных катушек наблюдается лавинообразный рост общего сопротивления, начиная с частоты 10 кГц, в то время как у однослойных катушек происходит равномерный рост общего сопротивления на всём диапазоне частот до 100 кГц.

Представлены результаты исследований корреляции рабочих характеристик однослойных и многослойных катушек индуктивности в зависимости от их параметров в частотном диапазоне от 20 Гц до 100 кГц. Рассчитаны значения напряжения, необходимого для обеспечения напряжённости магнитного поля 1, 5, 20 Э при 25 Гц и 100 кГц. Проанализировав полученные данные, найдены оптимальные параметры катушки индуктивности, обеспечивающие стабильные рабочие характеристики в диапазоне частот до 100 кГц.

Ключевые слова: катушка индуктивности, экранирование, электромагнитное излучение.

DOI: 10.21122/2220-9506-2021-12-1-30-37

Адрес для переписки:
Канафьев О.Д.
НПЦ НАН Беларуси по материаловедению,
ул. П. Бровки, 19, г. Минск 220072, Беларусь
e-mail: olegkan96@mail.ru

Address for correspondence:
Kanafyev O.D.
Scientific and Practical Materials Research Center of the National Academy of Sciences of Belarus,
P. Brovki str., 19, Minsk 220072, Belarus
e-mail: olegkan96@mail.ru

Для цитирования:
O.D. Kanafyev, A.V. Trukhanov, T.I. Zubar, S.A. Chizhik, S.S. Grabchikov.
Optimization of the Emitting Coil of a Hardware-Software Complex for Study of Low-Frequency Electromagnetic Radiation's Shielding Effectiveness.
Приборы и методы измерений.
2021. – Т. 12, № 1. – С. 30–37.
DOI: 10.21122/2220-9506-2021-12-1-30-37

For citation:
O.D. Kanafyev, A.V. Trukhanov, T.I. Zubar, S.A. Chizhik, S.S. Grabchikov.
Optimization of the Emitting Coil of a Hardware-Software Complex for Study of Low-Frequency Electromagnetic Radiation's Shielding Effectiveness.
Devices and Methods of Measurements.
2021, vol. 12, no. 1, pp. 30–37.
DOI: 10.21122/2220-9506-2021-12-1-30-37

Introduction

A great threat to the security of information on electronic devices, sensitive elements of various devices, biological objects is created by electromagnetic radiation of various nature. Sources of electromagnetic radiation in everyday life are household appliances, electric vehicles, mobile phones and other electronic devices [1, 2]. To protect against electromagnetic radiation, there are active and passive methods [3]. The passive method is to use screens that absorb or reflect electromagnetic radiation (EMR). For passive protection materials with high magnetic permeability are used. With the help of passive screens it is possible to protect certain sensitive elements of the device, and these screens are easy to use and more profitable in economic terms. However, at the moment there is no unified method for analyzing the effectiveness of shielding. Most scientific papers consider the effect of low-frequency EMR on living organisms and plants without affecting the analysis of the effectiveness of screens.

Analysis of information on the topic of this work shows that there are no standardized generally accepted methods for assessing the effectiveness of shielding [5–7]. To assess the shielding properties of various materials a device or apparatus with a sufficiently powerful emitter of electromagnetic radiation is required which stably operates both with direct and alternating currents of various frequencies. Inductors [8] can be used as such as an emitter, varying the parameters of which the required result can be achieved.

The purpose of this work was to manufacture inductor coils with different parameters, study their characteristics, and determine a sample that provides stable electromagnetic radiation in the frequency range from 25 Hz to 100 kHz. The sample coil with optimal parameters will be used in the hardware-software complex as an emitter and will allow to obtain new, unique data on the shielding efficiency of magnetic coatings and multilayer structures based on them, as well as to compare the previously obtained data on the shielding efficiency in a constant magnetic field with new data that will be obtained with alternating electromagnetic radiation.

Measurement technique

Single-layer and multi-layer inductors were manufactured as prototypes. For the manufacture of single-layer inductors copper wire with a cross section of 1 and 2 mm was used. The inner diameter (d) of the coils was 7 and 15 mm, the number of turns (N) was from 6 to 41, and the length (l) was from 15 to 65 mm. Multilayer coils were made from copper wire with a diameter of 0.1; 0.18 and 0.35 mm. The coils diameter was 6 mm, the number of turns was from 1000 to 6000, and the length was from 20 to 120 mm. Detailed information about the samples′ parameters is presented in Table 1.

Table 1

Parameters of inductors

№	Coil designation	d, mm	N	l, mm	t, mm
	Single layer coils				
1	*SL_N*6*_t*2*_d*7	7	6	15	2
2	*SL_N*11*_t*2*_d*7	7	11	25	
3	*SL_N*14*_t*2*_d*7	7	14	35	
4	*SL_N*18*_t*2*_d*7	7	18	45	
5	*SL_N*28*_t*2*_d*7	7	28	65	
6	*SL_N*6*_t*2*_d*15	15	6	15	
7	*SL_N*11*_t*2*_d*15	15	11	25	
8	*SL_N*13*_t*2*_d*15	15	13	35	
9	*SL_N*18*_t*2*_d*15	15	18	45	
10	*SL_N*27*_t*2*_d*15	15	27	65	
	Multilayer coils				
1	*N*4-*t*.1-*d*6	6	4000	20	0.1
2	*N*1-*t*.18-*d*6	6	1000	19.6	0.18
3	*N*8-*t*.15-*d*6	6	8000	22	0.15
4	*N*2-*t*.35-*d*6	6	2000	70	0.35
5	*N*4-*t*.35-*d*6	6	4000	100	0.35
6	*N*6-*t*.35-*d*6	6	6000	120	0.35

The manufactured samples′ parameters, such as inductance (L), active (R) and total resistance (Z) were obtained using an *MNIPI E*7-20 emittance meter. In practice, the coils with the optimal parameters calculated theoretically were connected to a current source and amplifier. To detect electromagnetic radiation a multilayer inductor connected to a *UTB-TREND* 722-050-5 oscilloscope was used as a signal receiver.

Results and discussion

As can be seen from the graphs (Figure 1), the *SL_N*6*_t*2*_d*7 coil has the lowest inductance among the coils with an inner diameter of 7 mm. Among the coils with an inner diameter of 15 mm, the *SL_N6_t2_d15* coil has the smallest inductance. The inductance of the first sample increases from 0.1 to 0.2 μH in the frequency range from 25 Hz to 100 kHz, while the inductance of the second sample is stable over the entire frequency range and equals 0.5 μH. Despite the large inductance the *SL_N6_t2_d15* coil looks preferable to the *SL_N6_t2_d7* one, because it has a constant inductance value over the entire frequency range.

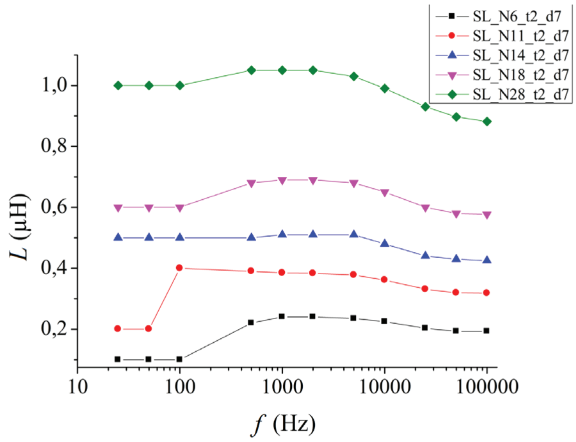

a

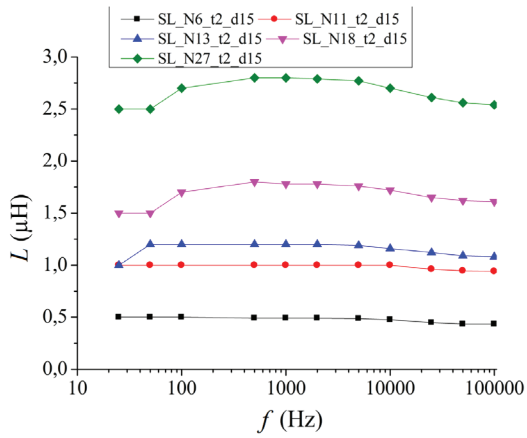

b

Figure 1 – Dependence of the inductance of single-layer coils on the current frequency: *a* – coil diameter 7 mm; *b* – coil diameter 15 mm

Figure 2 shows that all samples with an inner diameter of 7 and 15 mm have constant resistance values *R* at frequencies from 25 Hz to 5 kHz. After 5 kHz a sharp increase in resistance is observed in almost all samples, with the exception of samples *SL_N6_t2_d7*, *SL_N11_t2_d7* and *SL_N6_t2_d15*. This is most likely due to the skin effect [9] which consists in the fact that the currents flowing on the surface of the wire screen the inner layers, as a result of which almost all current is concentrated in a thin surface layer. The proximity effect also contributes, the essence of which is that eddy currents arise in the coil wire under the influence of a magnetic field from adjacent turns [10].

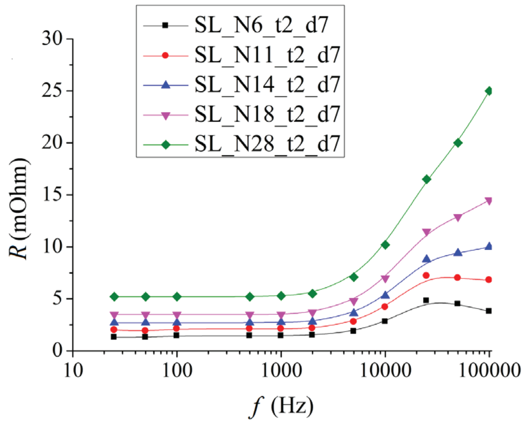

a

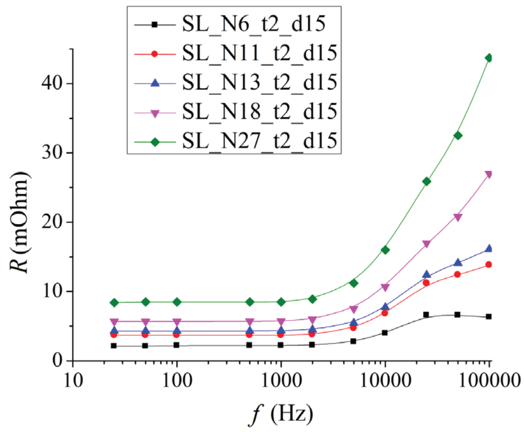

b

Figure 2 – Dependence of the resistance of single-layer coils on the current frequency: *a* – coil diameter 7 mm; *b* – diameter of coils 15 mm

Figure 3 shows that the total resistance of all coils increases linearly. Coils *SL_N6_t2_d7* and *SL_N6_t2_d15* have the lowest total resistance. This is probably due to the fact that these coils have fewer turns, respectively, in their manufacture, a shorter wire length is used compared to the rest of the samples.

These graphs show that the inductance *L* for coils with a diameter of 7 mm and a wire thickness of 2 mm does not change significantly at 100 Hz. For coils with a diameter of 15 mm and a wire thickness of 2 mm, as well as for coils with a diameter of 7 mm and a wire thickness of 1 mm, the inductance L practically does not change at frequencies up to 100 kHz.

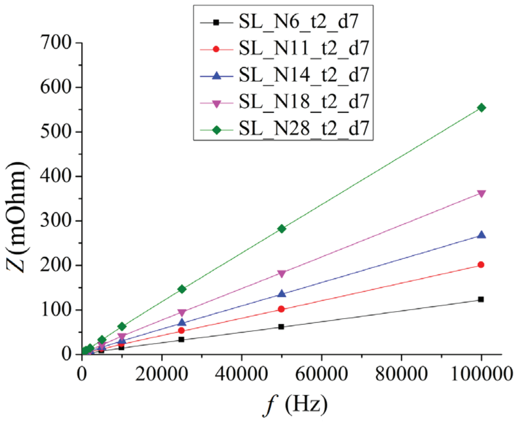

a

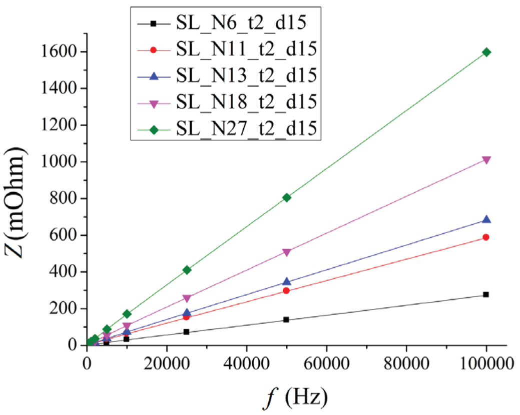

b

Figure 3 – Graphs of the dependence of the total resistance of single-layer coils on the current frequency: *a* – coil diameter 7 mm; *b* – coil diameter 15 mm

Coils with a diameter of 7 and 15 mm and a wire thickness of 2 mm have less resistance than coils with a diameter of 7 mm and a wire thickness of 1 mm. At the same time, for all coils a slight increase in resistance is observed over the entire frequency range up to 100 kHz. The total resistance of all single-layer coils increases linearly with increasing emitting frequency.

Figure 4 shows that some of the multilayer coils have constant inductance values over the entire frequency sample. The second part of the samples shows unpredictable inductance values. It can be assumed that this is due to the large number of turns in the coils, some of which may have insulation defects.

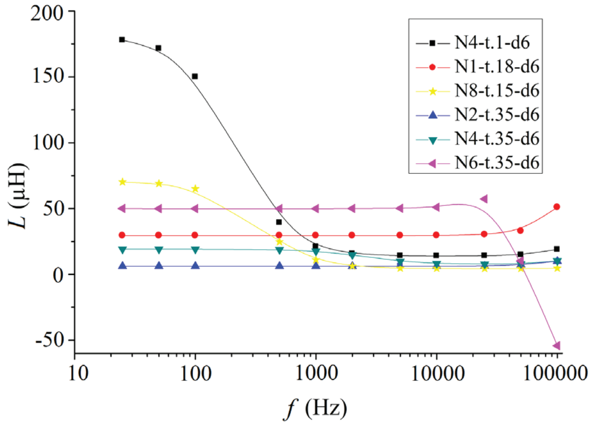

Figure 4 – Graph of the dependence of the inductance of multilayer coils on the current frequency

As seen in Figure 5, the resistance of multilayer coils is constant from 25 Hz to 10 kHz. After 10 kHz, an avalanche-like increase in resistance occurs. Coils *N*4-*t*.1-*d*6 and *N*1-*t*.18-*d*6 come into resonance due to the presence of skin and proximity effects. Parasitic capacitances also increase strongly at high frequencies. These capacitances, in combination with the high inductance of the coil, transform it into a whole chain of oscillatory circuits with resonances falling within the operating range or even below it, and then the coil acquires capacitive resistance.

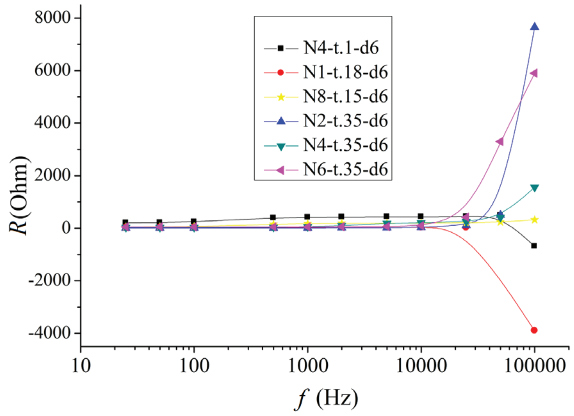

Figure 5 – Dependence of the resistance of multilayer coils on the frequency of the current

Figure 6 presents that the total resistance of all samples has a constant value from 25 Hz to 5 kHz, after 5 kHz there is a rapid increase in the total resistance. This is due to the presence of a skin effect and a proximity effect. These effects are much more pronounced with multilayer coils, due to the longer winding length and also due to the large number of turns.

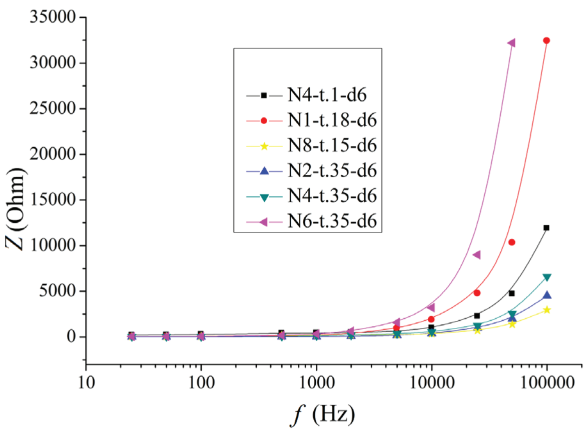

Figure 6 – Dependence of the total resistance of multilayer coils on the frequency of the current

Analyzing the graphs, we can conclude that all multilayer coils for the entire frequency sample have a constant inductance, except for two samples. At an electromagnetic field frequency of up to 10 kHz, multilayer coils have constant resistance. At a current frequency above 50 kHz, the resistance of all samples begins to increase sharply. The total resistance of the coils begins to increase when the frequency of the electromagnetic field is over 10 kHz.

The values of the magnetic field strength inside the cylindrical coil $H(E)$ for the manufactured samples of inductance coils were calculated by the formula:

$$I = \frac{In}{l},$$

where I – the current in the coil; n – the number of turns of the coil; l – the length of the coil;

$$I = \frac{U}{Z},$$

where U – the voltage applied to the circuit section; Z – impedance measured with an RLC meter.

Table 2

Calculation results of the voltage required to ensure the magnetic field strength of 1, 5, 20 Oe for single-layer coils

№	Coil designation	$U_{1\ \mathrm{Oe}}$, V		$U_{5\ \mathrm{Oe}}$, V		$U_{20\ \mathrm{Oe}}$, V	
		25 Hz	10 kHz	25 Hz	10 kHz	25 Hz	10 kHz
1	*SL_N6_t2_d7*	0.00026	0.0245	0.0013	0.1225	0.005174	0.48755
2	*SL_N11_t2_d7*	0.00042	0.04002	0.0021	0.2001	0.0084	0.8004
3	*SL_N14_t2_d7*	0.00054	0.05346	0.0027	0.2673	0.0108	1.0692
4	*SL_N18_t2_d7*	0.0007	0.07256	0.0035	0.3628	0.01323	1.371384
5	*SL_N28_t2_d7*	0.000988	0.105374	0.004836	0.515778	0.01924	2.05202
6	*SL_N6_t2_d15*	0.00042	0.05468	0.0021	0.2734	0.0084	0.2734
7	*SL_N11_t2_d15*	0.000648	0.10548	0.003276	0.53326	0.013104	2.13304
8	*SL_N13_t2_d15*	0.000946	0.150194	0.004644	0.737316	0.01849	2.93561
9	*SL_N18_t2_d15*	0.00114	0.2028	0.0057	1.0142	0.0228	4.0568
10	*SL_N27_t2_d15*	0.00042	0.05468	0.002016	0.262464	0.008085	1.05259

For the stable operation of the electromagnetic radiation at different frequencies, it is required to vary the values of the emitting supplied to the coils. The tables above show the voltage values calculated to provide magnetic field strengths of 1, 5, 20 Oe in the frequency range from 25 Hz to 100 kHz, for single-layer and multi-layer coils.

Table 3

Calculation results of the voltage required to ensure the magnetic field strength of 1, 5, 20 Oe multilayer coils

№	Coil designation	$U_{1\text{ Oe}}$, V		$U_{5\text{ Oe}}$, V		$U_{20\text{ Oe}}$, V	
		25 Hz	10 kHz	25 Hz	10 kHz	25 Hz	10 kHz
1	$N4$-t.1-$d6$	0.08424	4.76	0.4212	23.8	1.6848	95.2
2	$N1$-t.18-$d6$	0.04680	5.13	0.23648	59.2	0.94592	136.8
3	$N2$-t.35-$d6$	0.038136	12.6	0.19068	63	0.76272	252
4	$N4$-t.35-$d6$	0.05794	13.22	0.2897	66.1	1.1588	264.4
5	$N6$-t.35-$d6$	0.08352	42.24	0.4176	211.2	1.6704	844.8

Analyzing the data obtained, we can say that to ensure the operation of multilayer coils, a much higher voltage is required compared to single-layer coils. This is due to the high values of the inductance of multilayer coils as well as the presence of skin and proximity effects. Single-layer coils are also subject to these disadvantages but to a much lesser extent. In addition the voltage values required to operate at 20 Oe of multilayer coils are likely to be critical. Difficulties also arise with the selection of a voltage source operating in such a wide range of values.

Conclusion

Investigations of single-layer and multilayer inductors with different parameters have been carried out.

It was found that it is preferable to use single-layer inductors as a source of electromagnetic radiation operating in the frequency range up to 100 kHz. At a frequency from 10 to 100 kHz, an avalanche-like increase in total resistance begins in multilayer inductors; when measuring the active resistance, some samples enter into resonance. This is due to the presence of skin and proximity effects, which are pronounced in multilayer samples, due to a much larger number of turns, as well as their tightness. The inductance of multilayer coils is 1000 times higher than single-layer coils, as a result of which parasitic capacitances increase significantly. The combination of the factors given above transform a multilayer coil into a chain of oscillatory circuits with resonances often falling into the operating range or below it.

Due to the use of a wire with a cross section of 2 mm for winding single-layer coils, the active resistance of these samples is approximately 1000 times less than that of multilayer coils. Also, due to this fact, much lower values of the applied voltage are required to provide a power of electromagnetic radiation similar to multilayer samples.

Measurements have shown that when the current frequency reaches 5 kHz, a sharp increase in resistance is observed in almost all samples of single-layer coils, with the exception of samples with 6 turns and inner diameters of 7 and 15 mm. It can be assumed that these coils are less susceptible to negative effects due to the fewer turns. A coil with 6 turns and a 7 mm diameter has the lowest inductance value at a current frequency of 100 kHz. However, a sample with 6 turns and a 15 mm diameter has a constant inductance value over the entire frequency range from 25 Hz to 100 kHz. This fact makes the choice in favor of this coil preferable, because the difference in the voltage values required to provide a magnetic field strength of 20 Oe is insignificant.

Reel with optimal parameters planned use as a source of electromagnetic radiation in the hardware and software complex to study the effectiveness of shielding electromagnetic radiation. This hardware and software complex will have a unique structure and characteristics and will allow high-precision studies of the correlation of the chemical composition, structure, and shielding efficiency of a wide range of materials.

In the future, it is planned to conduct research on the influence of various types of cores on the performance of emitting inductors.

References

1. Zhang C., Han Y., Zhang P., Song G., Zhou C. Research on modern radar emitter modeling technique under complex electromagnetic environment. *The Journal of Engineering*, 2019, vol. 2019, iss. 20, pp. 7134–7138.
DOI: 10.1049/joe.2019.0579

2. Kechiev L.N., Akbashev B.B., Stepanov P.V. Shielding of technical means and shielding systems. M.: Iz-in. ITD Group Publ., 2010, 470 p.

3. Hawking M., Vasaktasari V., Sidki P. Metal and ceramic coatings: production, properties and application. Tr. from English M.: Mir Publ., 2000, 516 p.
DOI: 10.1016/0032-0633(59)90029-7

4. McLean J.S. Electric field generator incorporating a slow-wave structure. United States Patent. Appl. No.: 11/274.652. Date of Patent: Feb. 2, 2010. Patent No.: US 7,656,167 B1

5. Vaiser L.V., Kokorin B.I. Generator of electric and magnetic fields, a corresponding field detector, and a sample analyzer and treatment apparatus incorporating the field generator and/or field detector. Appl. No.: 10/396,440. Date of Patent: Aug. 3, 2004. Patent No.: US 6,770,023 B2

6. Gizatullin Z.M. Investigation of the effectiveness of shielding the body of a personal computer under intentional electromagnetic influences. *Bulletin of the Kazan State Technical University. AN Tupolev*, 2008, no. 1, pp. 28–31.

7. Shatalov D.P. A device for creating a powerful high-frequency alternating magnetic field. Invention patent. Application: 2008135378/09 from 03.09.2008. Published: 10.12.2009. Patent number: RU 2375722 C1.

8. Fadeev S.A. Inductor. Utility model patent. Application: 2011119668/07 dated 16.05.2011. Published: 10.01.2012. Patent number: RU 112496 U1.

9. Rysin A.V., Rysin O.V., Boykachev V.N., Nikiforov I.K. The paradox of the skin effect. *Sciences of Europe*, 2018, no. 28, pp. 52–61.

10. Kryukov A.V., Zakaryukin V.P., Sokolov V.Yu. Modeling of power supply systems with powerful busbars. Ed. A.V. Kryukov. Irkutsk: IrGUPS Publ., 2010, pp. 4–5.

Development of Executive Equipment Design for Implementing the Process of Generating of Drops of Micro- and Nanoscale Range

M.A. Kuznetsov[1], D.P. Ilyaschenko[1,2], A.V. Kryukov[1], S.A. Solodsky[1], E.V. Lavrova[3], E.V. Verkhoturova[4]

*[1]Yurga Institute of Technology National Research Tomsk Polytechnic University,
Leningradskaya str., 26, Yurga 652055, Russia*

*[2]Institute of Strength Physics and Materials Science of Siberian Branch Russian Academy of Sciences,
Academic Ave., 2/4, Tomsk 634055, Russia*

*[3]Priazovskyi State Technical University,
Universitetska str., 7, Mariupol 87500, Ukraine*

*[4]Irkutsk National Research Technical University,
Lermontova str., 83, Irkutsk 664074, Russia*

*Received 30.11.2020
Accepted for publication 15.02.2021*

Abstract

Modeling of velocities and temperatures processes distribution in the plasma-forming channel determining the design features and optimal parameters of the plasma torch nozzle is one of promising directions in development of plasma technologies. The aim of this work was to simulate the processes of velocities and temperature distribution in the plasma-forming channel and to determine the design features and optimal geometric parameters of the plasmatron nozzle which ensures the formation of necessary direction of plasma flows for generation of surface waves on the surface of a liquid metal droplet under the influence of the investigated instabilities.

One of the main tasks is to consider the process of plasma jet formation and the flow of electric arc plasma. For obtaining small-sized particles one of the main parameters is the plasma flow velocity. It is necessary that the plasma outflow velocity be close to supersonic. An increase of the supersonic speed is possible due to design of the plasmatron nozzle especially the design feature and dimensions of the gas channel in which the plasma is formed. Also the modeling took into account dimensions of the plasma torch nozzle, i. e. the device should provide a supersonic plasma flow with the smallest possible geometric dimensions.

As a result models of velocities and temperatures distribution in the plasma-forming channel at the minimum and maximum diameters of the channel were obtained. The design features and optimal geometric parameters of the plasmatron have been determined: the inlet diameter is 3 mm, the outlet diameter is 2 mm.

The design of the executive equipment has been developed and designed which implements the investigated process of generating droplets of the micro- and nanoscale range. A plasmatron nozzle was manufactured which forms the necessary directions of plasma flows for the formation of surface waves on the metal droplet surface under the influence of instabilities. An algorithm has been developed for controlling of executive equipment that implements the process of generating drops of micro- and nanoscale range.

Keywords: modeling, arc plasma, plasma torch nozzle, geometric parameters, control algorithm.

DOI: 10.21122/2220-9506-2021-12-1-38-45

Адрес для переписки:
*Ильященко Д.П.
Югринский технологический институт (филиал) Национального исследовательского Томского политехнического университета,
ул. Ленинградская, 26, г. Юрга 652055, Россия
e-mail: mita8@rambler.ru*

Address for correspondence:
*Ilyaschenko D.P.
Yurga Institute of Technology National Research Tomsk Polytechnic University,
Leningradskaya st., 26, 652055, Yurga, Russia
e-mail: mita8@rambler.ru*

Для цитирования:
M.A. Kuznetsov, D.P. Ilyaschenko, A.V. Kryukov, S.A. Solodsky, E.V. Lavrova, E.V. Verkhoturova.
Development of Executive Equipment Design for Implementing the Process of Generating of Drops of Micro- and Nanoscale Range.
Приборы и методы измерений.
2021. – Т. 12, № 1. – С. 38–45.
DOI: 10.21122/2220-9506-2021-12-1-38-45

For citation:
M.A. Kuznetsov, D.P. Ilyaschenko, A.V. Kryukov, S.A. Solodsky, E.V. Lavrova, E.V. Verkhoturova.
Development of Executive Equipment Design for Implementing the Process of Generating of Drops of Micro- and Nanoscale Range.
Devices and Methods of Measurements.
2021, vol. 12, no. 1, pp. 38–45.
DOI: 10.21122/2220-9506-2021-12-1-38-45

Devices and Methods of Measurements
2021, vol. 12, no. 1, pp. 38–45
M.A. Kuznetsov et al.

Разработка конструкции исполнительного оборудования, реализующего процесс генерации капель микро- и нанодиапазона

М.А. Кузнецов[1], Д.П. Ильященко[1,2], А.В. Крюков[1], С.А. Солодский[1], Е.В. Лаврова[3], Е.В. Верхотурова[4]

[1]*Юргинский технологический институт (филиал) Национального исследовательского Томского политехнического университета,*
ул. Ленинградская, 26, г. Юрга 652055, Россия

[2]*Институт физики прочности и материаловедения Сибирского отделения Российской академии наук,*
пр-т Академический, 2/4, г. Томск 634055, Россия

[3]*Приазовский государственный технический университет,*
ул. Университетская, 7, г. Мариуполь 87500, Украина

[4]*Иркутский национальный исследовательский технический университет,*
ул. Лермонтова, 83, г. Иркутск 664074, Россия

Поступила 30.11.2020
Принята к печати 15.02.2021

Моделирование процессов распределения скоростей и температур в плазмообразующем канале, определение конструктивных особенностей и оптимальных параметров сопла плазмотрона является одним из перспективных направлений в развитии плазменных технологий. Целью данной работы являлось моделирование процессов распределения скоростей и температур в плазмообразующем канале и определение конструктивных особенностей и оптимальных геометрических параметров сопла плазмотрона, которое должно обеспечивать формирование необходимых направлений плазменных потоков для образования на поверхности капли жидкого металла поверхностных волн под действием исследуемых неустойчивостей.

Одной из главных задач является рассмотрение процесса формирования плазменной струи и течения электродуговой плазмы. Для получения мелкоразмерных частиц одним из главных параметров является скорость течения плазмы. Необходимо, чтобы скорость истечения плазмы была близка к сверхзвуковой. Увеличение скорости до сверхзвуковой возможно добиться за счёт конструкции сопла плазмотрона, а именно конструктивной особенностью и размерами газового канала, в котором образуется плазма. Также при моделировании учитывались размеры сопла плазмотрона, т. е. устройство должно обеспечивать сверхзвуковое течение плазмы при возможно меньших геометрических размерах.

В результате исследований получены модели процессов распределения скоростей и температур в плазмообразующем канале при минимальных и максимальных диаметрах канала. Определены конструктивные особенности и оптимальные геометрические параметры сопла плазмотрона: диаметр на входе 3 мм, диаметр выходной 2 мм.

Разработана и спроектирована конструкция исполнительного оборудования, реализующая исследуемый процесс генерации капель микро- и наноразмерного диапазона. Изготовлено сопло плазмотрона, формирующее необходимые направления плазменных потоков для образования на поверхности капли жидкого металла поверхностных волн под действием исследуемых неустойчивостей. Разработан алгоритм управления исполнительным оборудованием, реализующем процесс генерации капель микро- и наноразмерного диапазона.

Ключевые слова: моделирование, плазма дуги, сопло плазмотрона, геометрические параметры, алгоритм управления.

DOI: 10.21122/2220-9506-2021-12-1-38-45

Адрес для переписки:
Ильященко Д.П.
Юргинский технологический институт (филиал) Национального исследовательского Томского политехнического университета,
ул. Ленинградская, 26, г. Юрга 652055, Россия
e-mail: mita8@rambler.ru

Address for correspondence:
Ilyaschenko D.P.
Yurga Institute of Technology National Research Tomsk Polytechnic University,
Leningradskaya st., 26, 652055, Yurga, Russia
e-mail: mita8@rambler.ru

Для цитирования:
M.A. Kuznetsov, D.P. Ilyaschenko, A.V. Kryukov, S.A. Solodsky, E.V. Lavrova, E.V. Verkhoturova.
Development of Executive Equipment Design for Implementing the Process of Generating of Drops of Micro- and Nanoscale Range.
Приборы и методы измерений.
2021. – Т. 12, № 1. – С. 38–45.
DOI: 10.21122/2220-9506-2021-12-1-38-45

For citation:
M.A. Kuznetsov, D.P. Ilyaschenko, A.V. Kryukov, S.A. Solodsky, E.V. Lavrova, E.V. Verkhoturova.
Development of Executive Equipment Design for Implementing the Process of Generating of Drops of Micro- and Nanoscale Range.
Devices and Methods of Measurements.
2021, vol. 12, no. 1, pp. 38–45.
DOI: 10.21122/2220-9506-2021-12-1-38-45

Introduction

Currently, one of the most promising areas for the implementation of various technological processes is mathematical modeling. It is based on the construction of a model created by means of computer simulation of various physical and technological processes [1–7]. Development of various models that are as similar as possible to natural processes is very important in the case when setting up a natural experiment is impossible, very difficult or very expensive. Development of computer technology creates good prospects for application of rather complex models reflecting the multifactor nature and interconnection of various physical processes and phenomena. One of the most powerful modeling tools is the *COMSOL Multiphysics* software package which is designed to simulate various physical processes, systems and their interconnection [8, 9].

In literary sources [1–7], the authors provide data on modeling of various technological processes: the model of the effect of a shielding gas on heat distribution in the welding zone [1, 2], the model of temperature fields and resistance to deformation in cylindrical billets during heating [3], the model of optimization of remelting mode parameters of tungsten-inert gas with nanomodification of the surface layer [4], the model of the molten pool, when welding with a consumable electrode in shielding gas [5], the model of the influence of the input parameters of the laser welding mode on the quality of the weld [6], the model of welding technology for high-strength steel sheets [7]. The disintegration of a liquid jet into droplets is a common phenomenon both in industrial processes and in natural phenomena. Droplets are formed due to disturbances and a certain type of instability on the surface of the liquid jet. The resulting surface waves with different amplitudes are a prerequisite for the formation of drops [10–12].

The work is aimed at the experimental determination of technological conditions for creating a technology for the formation of micro- and nanodroplets under conditions of exposure to the transfer of the electrode metal by concentrated plasma energy flows. The paper proposes a mechanism for the formation of droplets of nano- and micrometer sizes, based on the appearance and development of a thin liquid interlayer of the micro- and nanometer range on the surface of a liquid metal under the action of heterogeneous plasma flows. This phenomenon occurs when a metal wire is fed into the heterogeneous plasma zone of an electric arc.

The aim of the work was to simulate the processes of distribution of velocities and temperatures in the plasma-forming channel and to determine the design features and optimal geometric parameters of the plasmatron nozzle which should provide the formation of the necessary directions of plasma flows for the formation of surface waves on the surface of a liquid metal droplet under the influence of the instabilities under study.

Mathematical problem statement

To develop the design of the executive equipment that implements the process of droplets′ generating of the micro- and nanoscale range we simulated the process of obtaining small-sized particles using plasma spraying.

One of the main tasks is to consider the process of a plasma jet formation and the flow of electric arc plasma. For obtaining of small-sized particles one of the main parameters is the plasma flow velocity. It is necessary for plasma outflow velocity to be close to supersonic. An increase in speed to supersonic can be achieved due to the design of the plasma torch nozzle, namely, the design feature and dimensions of the gas channel in which the plasma is formed. Also, the modeling took into account dimensions of the plasma torch nozzle, i. e. the device should provide a supersonic plasma flow with the smallest possible geometric dimensions.

When formulating the problem the following boundary conditions were established in the *COMSOL Multiphysics* software package:

– the gas flow is laminar;
– the effect of gravity is not taken into account;
– an axisymmetric problem is considered;
– thermodynamic and transport properties of gas depend on temperature.

The developed model is described by the following basic equations:

1. Maxwell's equations:

$$\begin{cases} \boldsymbol{J} = \left(\sigma + \varepsilon\varepsilon_0 \dfrac{\partial}{\partial \boldsymbol{t}} \right) \boldsymbol{E}; \\ \boldsymbol{E} = -\nabla V; \\ \sigma \dfrac{\partial \boldsymbol{A}}{\partial t} + \nabla \times \boldsymbol{H} = \boldsymbol{J}; \\ \boldsymbol{B} = \nabla \times \boldsymbol{A}, \end{cases}$$

where ***J*** – current density; ***E*** – electric field strength; ***A*** – magnetic vector potential; ***B*** – magnetic induction vector; ***H*** – vector of magnetic intensity; *V* – electric potential; σ – electrical conductivity; ε – relative permittivity.

2. Energy balance equation:

$$\rho Cp\frac{\partial T}{\partial t}+\rho Cp\boldsymbol{u}\cdot\nabla T=\nabla\cdot(k\nabla T)+Q;$$

$$Q=E\cdot J+Q_{rad},$$

where ρ – density; *Cp* – heat capacity; *k* – thermal conductivity; *EJ* – Joule heating; Q_{rad} – radiation losses; ***u*** – velocities field.

3. Equation of motion:

$$\rho\frac{\partial u}{\partial t}+\rho(u\cdot\nabla)\cdot u=\nabla\cdot\left[-pI+\mu\cdot\left(\nabla u+(\nabla u)^T\right)\right]+F;$$

$$F=\frac{1}{2}\mathrm{Re}(J\times B),$$

where *F* – Lorentz force; *p* – pressure; *T* – temperature; μ – dynamic viscosity; ρ – the density; the relative magnetic permeability; Re – Reynolds number.

4. The continuity equation:

$$\rho\frac{\partial \boldsymbol{u}}{\partial t}+\nabla(\rho\boldsymbol{u})=0,$$

where ***u*** – instantaneous velocities field at time *t*.

Modeling of the process of obtaining small-sized particles was carried out using plasma spraying in the *COMSOL Multiphysics* software package. For the operation of the plasmatron, the geometric dimensions of the gas channel in which the plasma is formed are important. An image of the structural elements of the plasmatron gas channel is shown in Figure 1.

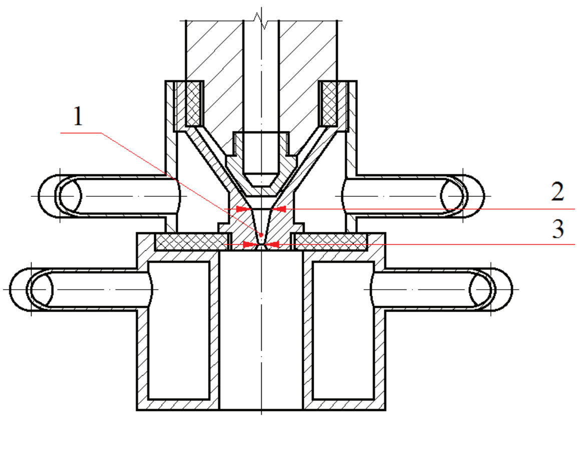

Figure 1 – The main structural elements of the plasmatron: 1 – gas channel; 2 – inlet diameter; 3 – outlet diameter

In order to optimize the geometry of the nozzle and the parameters of the plasmatron mode, the process of the plasmatron operation was simulated. The computational domain of the problem is the gas channel of the designed plasmatron and is shown in Figure 2. Various values of the inlet and outlet diameters of the supersonic nozzle and its length were considered. The hydrodynamic flow of the arc plasma jet depends on the geometric parameters (diameter and shape) of the gas channel of the plasmatron.

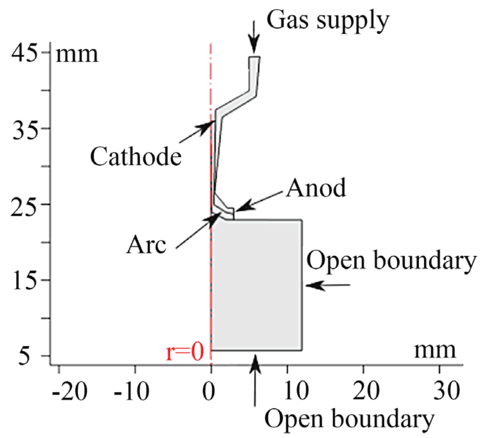

Figure 2 – Calculation area

Varying the input parameters when modeling the nozzle of the plasmatron was carried out in the ranges shown in Table.

Table

Parameters for the production of micro- and nanoscale range powders

Gas consumption, *l*/min	10...40
Current, A	100...200
Outlet diameter, mm	2…4
Nozzle length, mm	10...30
Inlet diameter, mm	3...10

Results and discussion

Figure 3 shows the results of modeling of the plasmatron nozzle with the following input parameters: gas flow rate 20 *l*/min, current 150 A, nozzle length 20 mm. The values of the gas velocity in the throat of the jet nozzle and the temperature distribution in the flow were considered (Figure 3*a*, *b* at maximum channel diameters: outlet diameter 4 mm, inlet diameter 10 mm; Figure 3*c*, *d* at minimum channel diameters: outlet diameter 2 mm, diameter at the inlet 3 mm). In this case, the design

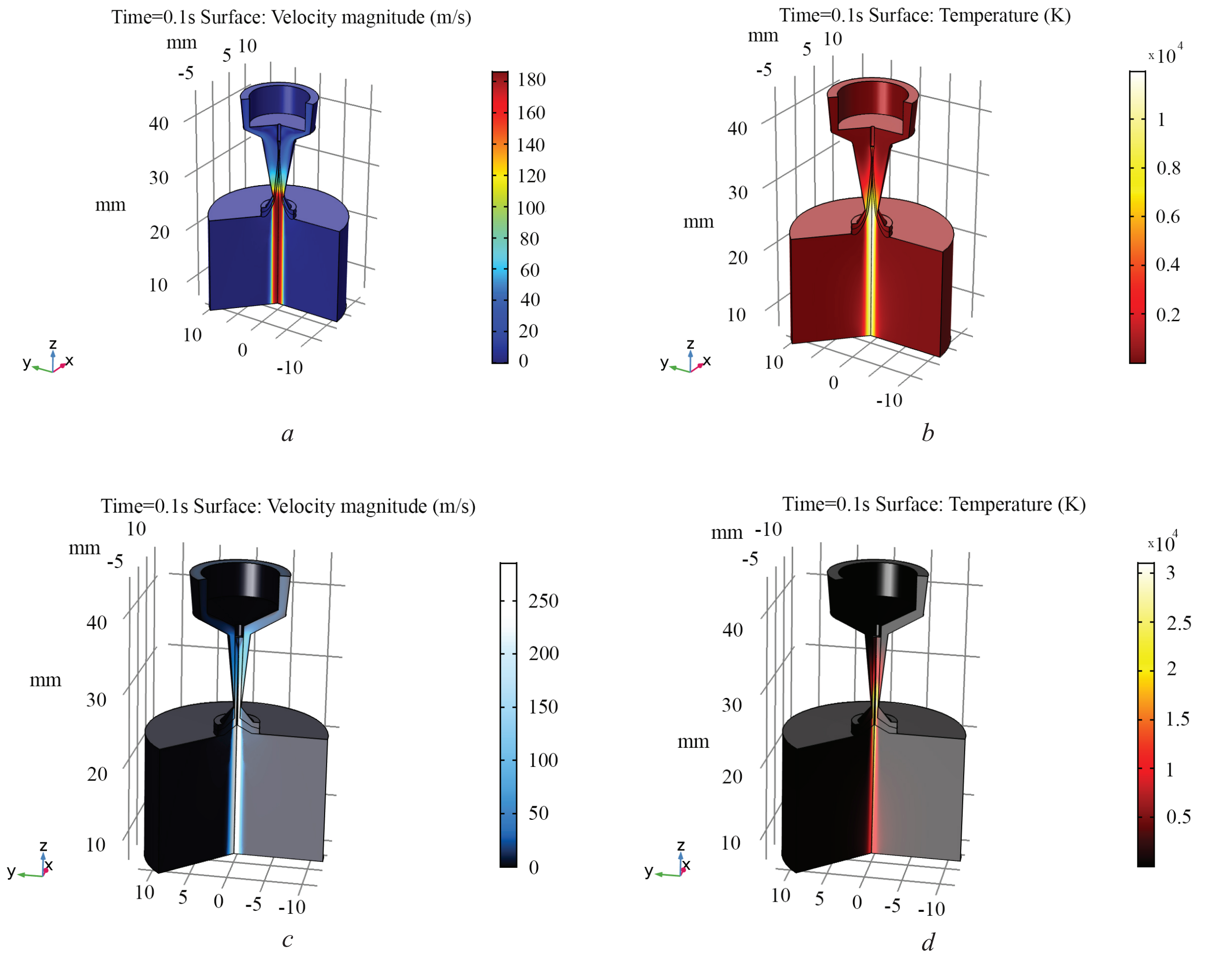

Figure 3 – Distribution of velocities and temperatures in the plasma-forming channel: *a* – velocity distribution at the maximum channel diameter; *b* – temperature distribution at the maximum channel diameter; *c* – velocity distribution at the minimum channel diameter; *d* – temperature distribution at the minimum channel diameter

features and optimal dimensions of the gas channel should ensure effective melting of the filler material and it's crushing into particles.

Based on the simulation results a plasmatron nozzle was developed (Figure 4) with design features and optimal geometric parameters: inlet diameter – 3 mm, outlet diameter – 2 mm, which provide a plasma flow rate close to supersonic, and the formation of the necessary direction of plasma flows for the formation on the liquid metal drop surface waves under the influence of the investigated instabilities.

The size and chemical composition of the obtained micro- and nanoscale range powders depends on the plasmatron operating mode: amperage, gas consumption, wire: diameter (from 0.8 to 1.2 mm) and chemical composition.

The developed nozzle (Figure 4) will be one of the main details of the laboratory equipment being created for the production of micro- and nanosized powders, the block diagram of which is shown in Figure 5.

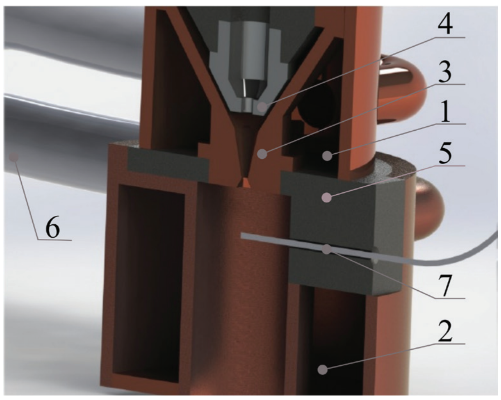

Figure 4 – Plasmatron nozzle model: 1 – upper body; 2 – lower body; 3 – nozzle; 4 – tip; 5 – insulator; 6 – water supply pipes; 7 – wire

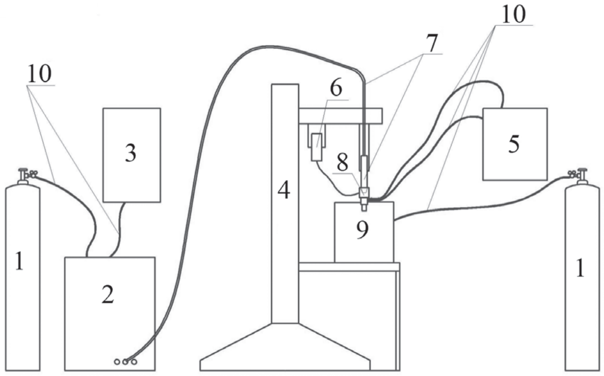

Figure 5 – Equipment block diagram: 1 – inert gas cylinder; 2 – plasma power supply; 3 – compressor; 4 – rack; 5 – chiller (industrial cooler); 6 – wire spool; 7 – plasmatron; 8 – nozzle; 9 – particle catcher; 10 – hose

The work of the equipment for the production of micro- and nanoscale range powders is as follows: the plasma power supply 2 and the compressor 3 are turned on; a cylinder with inert gas 1 is opened. The inert gas (argon, helium) is selected depending on the chemical composition of the wire from which the powders are obtained. Then we turn on the chiller 5 and open the cylinder with inert gas 1. We start the wire feeder, which feeds the wire from the spool 6 to the nozzle 8, located on the stationary stand 4. The diameter and chemical composition of the wire is selected depending on the size and chemical composition of the powders obtained. The wire, entering the nozzle 6, passes through a high-temperature section; a drop of molten metal is formed at the end of the wire. In nozzle 6, plasma flows move at a high speed, the directions of which contribute to the formation of surface waves on the surface of a liquid metal droplet under the influence of the instabilities under study. Under the action of high-frequency ultrasonic action on the wire and, accordingly, on a drop of molten metal from its surface, the plasma flow tears off liquid objects several microns in size or less. Liquid objects torn off from the surface are accelerated to high speeds in a nozzle, additionally crushed, take a spherical shape under the influence of surface forces, condense in a particle catcher in an inert gas atmosphere and form micro- and nanoscale range powders. The dispersion of the resulting powder granules was determined by the method of simulation and visualization [13].

The equipment control algorithm (Figure 5) is shown in Figure 6.

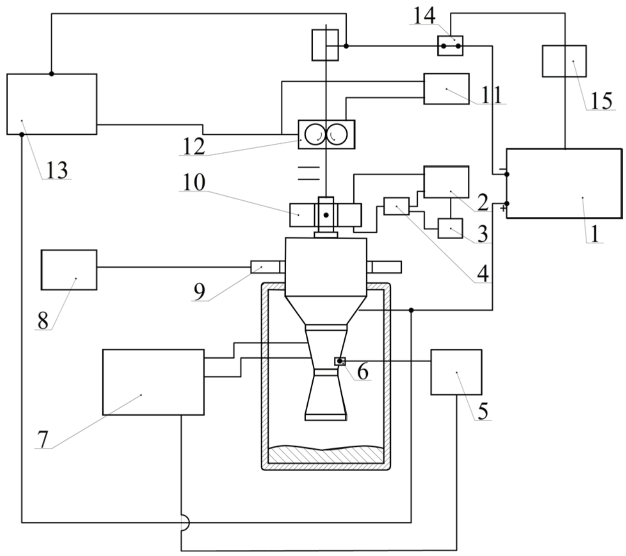

Figure 6 – The scheme of the equipment control algorithm: 1 – plasma power source; 2 – ultrasonic generator; 3 – frequency matching and correction unit; 4 – resonance sensor; 5 – temperature control unit; 6 – thermal sensor; 7 – chiller; 8 – arc stabilizer control unit; 9 – arc stabilizer; 10 – magnetostrictive inertialess solenoid; 11 – wire feed control unit; 12 – wire feeder; 13 – arc gap length control unit; 14 – current sensor; 15 – block of comparison and correction of current; 16 – arc plasmatron; 17 – particle catcher; 18 – gas cylinder

The control algorithm of the installation shown in Figure 6 is as follows:

– the feed mechanism (12), controlled by the wire feed control unit (11), feeds the wire into the arc plasmatron (16), where it melts. The formation of the Kelvin–Helmholtz [14, 15] and Marangoni instabilities on a drop of molten metal is carried out due to the special design of the plasmatron, which transfers the rotation of plasma streams formed from the plasma-forming gas (18). High-frequency oscillations are used to detach the formed instabilities from the droplet surface. To generate high-frequency vibrations, the wire pass through a magnetostrictive inertialess solenoid (10) controlled by an ultrasonic generator (2), while an ultrasonic wave is formed in the wire due to the effect of magnetostriction. An ultrasonic wave forms Rayleigh waves on a drop of molten metal, causing particles to detach. The resulting particles enter the particle catcher (17). The resonant frequency of oscillations is set via the feedback channel through the frequency matching and correction unit (3) and the resonance sensor (4);

– additional rotation of the arc and stabilization of plasma flows occurs due to the arc stabilizer (9), controlled by the arc stabilization control unit (8);

– to ensure the stabilization of the preset operating temperature in the laboratory setup, a thermal sensor (6) is installed on the nozzle. Temperature control and regulation is carried out by the chiller (7) through feedback channels through the temperature control unit (5);

– to control the size of the received particles in the installation there is an automatic regulation of the arc length. The arc length is controlled by the voltage of the arc gap and is controlled by feedback channels through the arc gap length control unit (13);

– automatic maintenance of the current of the specified parameters, carried out by the plasma power supply (1) through the feedback channels, including through the current sensor (14) and the unit for comparison and current correction (15).

Thus, the control system of the installation automatically regulates four main parameters: the frequency of ultrasonic vibrations, the current in the plasmatron, the length of the arc gap, and the operating temperature in the nozzle, the change of which makes it possible to control the size of the particles obtained.

Conclusion

Models of the processes of distribution of velocities and temperatures in the plasma-forming channel at the minimum and maximum diameters of the channel are obtained.

The design features and optimal geometric parameters of the plasmatron nozzle have been determined: the inlet diameter is 3 mm; the outlet diameter is 2 mm. The design of the executive equipment has been developed and designed, which implements the investigated process of generating droplets of the micro- and nanoscale range. A plasmatron nozzle was manufactured, which forms the necessary directions of plasma flows for the formation of surface waves on the surface of a liquid metal droplet under the influence of the investigated instabilities.

An algorithm has been developed for controlling the executive equipment that implements the process of generating drops of micro- and nanoscale range. Thus, the control system of the laboratory facility automatically regulates four main parameters: the frequency of ultrasonic vibrations, the current in the plasma torch, the length of the arc gap and the operating temperature in the nozzle change of which allows you to control the size of the particles obtained.

In contrast to the existing electric arc plasmatrons, which are designed for metal processing, this development has a different purpose and is designed to produce powders of the micro- and nanoscale range.

Acknowledgments

The study was performed by a grant from the Russian Science Foundation (Project № 18-79-10035).

References

1. Chinakhov D.A., Vorobjev A.V., Tomchik A.A. Simulation of Active Shielding Gas Impact on Heat Distribution in the Weld Zone. *Materials Science Forum*, 2013, no. 762, pp. 717–721.
DOI: 10.4028/www.scientific.net/MSF.762.717

2. Chinakhov D.A., Vorobjev A.V., Gotovshchik Y.M. Simulation of wind Influence on the thermal processes in gas-shielded welding. *Applied Mechanics and Materials*, 2014, no. 682, pp. 91–95.
DOI: 10.4028/www.scientific.net/AMM.682.91

3. Temlyancev M.V., Starikov V.S., Kondrat'ev V.G. [Modeling of temperature fields and the deformation resistance in cylindrical billets during heating from a hot fit for rolling]. *Izvestiya vysshih uchebnyh zavedenij. CHernaya metallurgiya*. [Proceedings of higher educational institutions. Ferrous metallurgy], 2000, no. 6, pp. 51–54 (in Russian).

4. Tashev P, Koprinkova-Hristova P, Petrov T, Kirilov L, Lukarski Y.J. Mathematical Modeling and Optimization of Parameters of the Mode for Tungsten-Inert Gas Remelting with Nanomodification of the Surface Layer. *Journal of Materials Science and Technology*, 2016, vol. 24, no. 4, pp. 230–243.

5. Peng J, Yang L. Mathematical model on characteristics of V groove molten pool during MIG welding. CIESC J., 2016, no. 67 (S1), pp. 117–126.
DOI: 10.11949/j.issn.0438-1157.20160625

6. Kumar N., Bandyopadhyay A. Simulation of the Effects of Input Parameters on Weld Quality in Laser Transmission Welding (LTW) Using a Combined Response Surface Methodology (RSM)-Finite Element Method (FEM) Approach. *Lasers in Engineering*, 2017, vol. 36, no. 4, pp. 225–243.

7. Bilenko G.A., Khaibrakhmanov R.U., Korobov Y.S. Computer Simulation in Developing the Technology of Welding High-Tensile Steel Sheets. Metallurgist, 2017, no. 61(3–4), pp. 265–270.
DOI: 10.1007/s11015-017-0487-8

8. Kuznetsov M.A., Solodsky S.A., Kryukov A.V., Ilyaschenko D.P., Verkhoturova E.V. Study of the Effect

of Shielding Gas on the Plasma Flow of an Electric Arc and on the Droplet of a Molten Metal. *Plasma Physics Reports*, 2021, no. 1, pp. 11–17.
DOI: 10.1134/S1063780X21010098

9. Kuznetsov M.A., Zernin E.A., Danilov V.I., Zhuravkov S.P., Kryukov A.V. Optimization of the Modification Parameters of a Deposited Metal by Nanostructural Fibers of the Aluminium Oxyhydroxide. *Nanotechnologies in Russia*, 2019, vol. 13, no. 9–10, pp. 521–530.
DOI: 10.1134/S1995078018050087

10. Eggers J., Villermaux E. Physics of liquid jets. *Reports on Progress in Physics*, 2008, no. 71(3), pp. 036601. **DOI:** 10.1088/0034-4885/71/3/036601

11. Hornung J., Zikin A., Pichelbauer K., Kalin M., Kirchgaßner M. Influence of cooling speed on the microstructure and wear behaviour of hypereutectic Fe-Cr-C hardfacings. *Materials Science and Engineering A*, 2013, no. 576, pp. 243–251.
DOI: 10.1016/j.msea.2013.04.029

12. Katsich C., Badisch E., Roy M., Heath G.R., Franek F. Erosive wear of hardfaced Fe-Cr-C alloys at elevated temperature. *Wear*, 2009, no. 267(11), pp. 1856–1864. **DOI:** 10.1016/j.wear.2009.03.004

13. Ilyaschenko D.P., Kryukov A.V., Lavrova E.V., Kuznetsov M.A., Verkhoturova E.V. Determination of the Parameters of Transported Drops of Electrode Metal by Simulation and Visualization. *Devices and Methods of Measurements*, 2020, vol. 11, no. 3, pp. 122–131.
DOI: 10.21122/2220-9506-2020-11-3-222-227

14. Kuznetsov M.A., Solodsky S.A., Kryukov A.V., Ilyaschenko D.P., Verkhoturova E.V. Study of the effect of shielding gas on the plasma flow of an electric arc and on the drop of a molten metal. *Applied Physics*, 2020, no. 1, pp. 11–17.

15. Sarychev V.D., Nevskiy S.A., Kuznetsov M.A., Solodsky S.A., Ilyaschenko D.P., Verkhoturova E.V. Kelvin-Helmholtz instability and magneto-hydrodynamic instability of a cylindrical column. *Applied Physics*, 2020, no. 3, pp. 5–10.

Algorithm for Control of Unmanned Aerial Vehicles in the Process of Visual Tracking of Objects with a Variable Movement's Trajectory

A.A. Adnastarontsau[1], D.A. Adnastarontsava[1], R.V. Fiodortsev[1], D.V. Katser[2], A.Y. Liavonau[2], D.V. Romanov[2], D.N. Tcherniakovski[1,3], A.O. Mikhailau[1,3]

[1]LLC "NTLab-IS",
Surganova str., 41, Minsk 220013, Belarus
[2]JSC "Peleng",
Makayonka str., 25, Minsk 220114, Belarus
[3]LLC "NTLab-Systems",
Surganova str., 41, Minsk 220013, Belarus

Received 20.01.2021
Accepted for publication 04.03.2021

Abstract

The purpose of the research was to create an algorithm for determining and correcting the output parameters of the navigation module and the flight-navigation complex of unmanned aerial vehicles which provides control of an aviation gyro-stabilized platform with a multispectral optoelectronic system during flight and tracking various objects of observation.

Principles of control of an aviation technical vision system located on an unmanned aerial vehicle on a two-degree gyro-stabilized platform with the possibility of full turn around two perpendicular axes along the course and pitch are considered. Stability of tracking of observation objects at a distance of up to 10000 m is ensured by the use of a multispectral optoelectronic system including a rangefinder, thermal imaging and two visual channels.

Analysis of the object of observation and the method of its support are carried out. An algorithm is proposed for integrating a Global Navigation Satellite System and a strapdown inertial navigation system based on the extended Kalman filter which includes two stages of calculations, extrapolation (prediction) and correction. Specialized software in the *FreeRTOS* v9.0 environment has been developed to obtain a navigation solution: latitude, longitude and altitude of the unmanned aerial vehicle in the *WGS*-84 coordinate system, as well as the pitch, heading and roll angles; north, east and vertical components of velocities in the navigation coordinate system; longitudinal, vertical and transverse components of free accelerations and angular velocities in the associated coordinate system based on data from the receiving and measuring module of the Global Navigation Satellite System and data from the 6-axis MEMS sensor *STIM*300.

Keywords: aviation technical vision system, optoelectronic system, algorithm, orientation angles, navigation module.

DOI: 10.21122/2220-9506-2021-12-1-46-57

Адрес для переписки:
Фёдорцев Р.В.
ООО «НТЛаб-ИС»,
ул. Сурганова, 41, г. Минск 220013, Беларусь
e-mail: feod@gmail.com

Address for correspondence:
Fiodortsev R.V.
LLC "NTLab-IS",
Surganova str., 41, Minsk 220013, Belarus
e-mail: feod@gmail.com

Для цитирования:
A.A. Adnastarontsau, D.A. Adnastarontsava, R.V. Fiodortsev, D.V. Katser, A.Y. Liavonau, D.V. Romanov, D.N. Tcherniakovski, A.O. Mikhailau.
Algorithm for Control of Unmanned Aerial Vehicles in the Process of Visual Tracking of Objects with a Variable Movement's Trajectory.
Приборы и методы измерений.
2021. – Т. 12, № 1. – С. 46–57.
DOI: 10.21122/2220-9506-2021-12-1-46-57

For citation:
A.A. Adnastarontsau, D.A. Adnastarontsava, R.V. Fiodortsev, D.V. Katser, A.Y. Liavonau, D.V. Romanov, D.N. Tcherniakovski, A.O. Mikhailau.
Algorithm for Control of Unmanned Aerial Vehicles in the Process of Visual Tracking of Objects with a Variable Movement's Trajectory.
Devices and Methods of Measurements.
2021, vol. 12, no. 1, pp. 46–57.
DOI: 10.21122/2220-9506-2021-12-1-46-57

Алгоритм управления беспилотными летательными аппаратами в процессе визуального сопровождения объектов с изменяемой траекторией движения

А.А. Одностороньцев[1], Д.А. Одностороньцева[1], Р.В. Фёдорцев[1], Д.В. Кацер[2], А.Ю. Леонов[2], Д.В. Романов[2], Д.Н. Черняковский[1,3], А.О. Михайлов[1,3]

*[1]ООО «НТЛаб-ИС»,
ул. Сурганова, 41, г. Минск 220013, Беларусь*
*[2]ОАО «Пеленг»,
ул. Макаёнка, 25, г. Минск 220114, Беларусь*
*[3]ООО «НТЛаб-Системы»,
ул. Сурганова, 41, г. Минск 220013, Беларусь*

*Поступила 20.01.2021
Принята к печати 04.03.2021*

Целью проводимых исследований являлось создание алгоритма определения и коррекции выходных параметров модуля навигации и пилотажно-навигационного комплекса беспилотных летательных аппаратов, обеспечивающего управление авиационной гиростабилизированной платформой с мультиспектральной оптико-электронной системой в процессе полёта и сопровождения различных объектов наблюдения.

Рассмотрены принципы управления авиационной системой технического зрения, размещённой на беспилотном летательном аппарате на двухстепенной гиростабилизированной платформе с возможностью полного разворота вокруг двух перпендикулярных осей по курсу и тангажу. Устойчивость сопровождения объектов наблюдения на расстоянии до 10000 м обеспечивается применением мультиспектральной оптико-электронной системы, включающей дальномерный, тепловизионный и два визуальных канала.

Выполнен анализ объекта наблюдения и методика его сопровождения. Предложен алгоритм интеграции спутниковой радионавигационной системы и бесплатформенной инерциальной навигационной системы на основе интегрального фильтра Калмана, предусматривающей две стадии вычислений: экстраполяцию (предсказание) и коррекцию. В модуль навигации встроено специализированное программное обеспечение для многозадачной операционной системы реального времени *FreeRTOS*, обеспечивающее получение навигационного решения: широты, долготы и высоты беспилотного летательного аппарата в системе координат *WGS*-84, а также углов крена тангажа и курса; северной, восточной и вертикальной составляющих скоростей в навигационной системе координат; продольной, вертикальной и поперечной составляющих свободных ускорений и угловых скоростей в связанной системе координат на основе данных от приёмо-измерительного модуля спутниковой радионавигационной системы и данных от 6-осевого МЭМС-датчика *STIM*300.

Ключевые слова: система технического зрения авиационная, оптико-электронная система, алгоритм, углы ориентации, модуль навигации.

DOI: 10.21122/2220-9506-2021-12-1-46-57

Адрес для переписки:
*Фёдорцев Р.В.
ООО «НТЛаб-ИС»,
ул. Сурганова, 41, г. Минск 220013, Беларусь
e-mail: feod@gmail.com*

Address for correspondence:
*Fiodortsev R.V.
LLC "NTLab-IS",
Surganova str., 41, Minsk 220013, Belarus
e-mail: feod@gmail.com*

Для цитирования:
A.A. Adnastarontsau, D.A. Adnastarontsava, R.V. Fiodortsev, D.V. Katser, A.Y. Liavonau, D.V. Romanov, D.N. Tcherniakovski, A.O. Mikhailau.
Algorithm for Control of Unmanned Aerial Vehicles in the Process of Visual Tracking of Objects with a Variable Movement's Trajectory.
Приборы и методы измерений.
2021. – Т. 12, № 1. – С. 46–57.
DOI: 10.21122/2220-9506-2021-12-1-46-57

For citation:
A.A. Adnastarontsau, D.A. Adnastarontsava, R.V. Fiodortsev, D.V. Katser, A.Y. Liavonau, D.V. Romanov, D.N. Tcherniakovski, A.O. Mikhailau.
Algorithm for Control of Unmanned Aerial Vehicles in the Process of Visual Tracking of Objects with a Variable Movement's Trajectory.
Devices and Methods of Measurements.
2021, vol. 12, no. 1, pp. 46–57.
DOI: 10.21122/2220-9506-2021-12-1-46-57

Introduction

Airborne vision and navigation systems of an aircraft are a combination of various devices: a radar station (radar), a thermal imager, a television (TV) camera, a laser locator (lidar), etc., which ensure the performance of various tasks related to observing objects in difficult weather conditions as well as in poor visibility conditions. Each of the sensors represents specific characteristics of the environment (brightness, thermal, radar, or optical-location contrasts of objects), but separately does not provide enough information about the underlying surface. The use of information coming simultaneously from several sensors requires solving a number of auxiliary mathematical problems. One of them is associated with the fact that images from different sensors are generally formed in different coordinate systems [1]. The concept of a multispectral vision system also makes it possible to improve flight safety by automatically correcting the current coordinates of the location of the aircraft in space, taking into account the terrain.

Modern trends in the creation of systems for tracking objects in multipurpose aircraft provide for software and hardware integration of onboard equipment in the form of container reconnaissance complexes. For example, the Russian development of the "Sych" family includes a three-level container complex:

– multispectral optical-electronic complex (*UKR-OE*) (TV/IR/low-level ranges);

– X-band surface radar reconnaissance complex (*UKR-RL*/*BKR*-3), represented by a two-way small-element radar system (radar) with a passive phased antenna array (PFAR) "Pika-M" with a resolution of about 0.3 m in *SAR*/*ISAR* and instrumental range of more than 300 km;

– a multi-band passive radio-technical reconnaissance complex (*UKR-RT*), which allows detecting and analyzing the frequency parameters of enemy radio-emitting sources (modern enemy airborne radars of *AN*/*APG*-77/79/81 types in aisle tracking and even LPI modes, active radar homing heads (GOS) air combat missiles and anti-aircraft missiles (SAMs), as well as surveillance radars and illumination radars) [2].

One of the important directions for improving onboard avionics is the development of hardware and software systems for "enhanced vision" (*Enhanced Flight Vision Systems*, EFVS). According to the functional characteristics of the systems of improved vision are divided into three typical classes [3]:

– Enhanced Vision System (EVS);

– Synthetic Vision System (SVS);

– Automated Vision System (AVS).

In papers [4–5], basic algorithms for the functioning of strapdown inertial navigation systems (SINS) are considered.

The purpose of the research was to create an algorithm for determining and correcting the output parameters of the navigation module and the flight-navigation complex of unmanned aerial vehicles (UAVs), which ensures the control of an aviation gyro-stabilized platform with a multispectral optoelectronic system during flight and tracking various objects of observation.

Multispectral optical-electronic system of technical vision based on an aviation gyro-stabilized platform

When using UAVs, the task often arises of tracking an object of interest for a long period of time. There may also be additional requirements for observation parameters:

– providing a given viewpoint;

– keeping the object of interest in the center of the frame, and for adjusting the circular flight path and transferring the coordinates of the circle center to the flight and navigation complex (FNC);

– maintaining a given angle of inclination in terms of distance to the object, etc.

To fulfill these parameters, it is not enough to control only the position of the sighting axis of the aviation technical vision system (STZA), but it is also required to issue corrective signals to the autopilot.

Let's consider the options for solving this problem in more detail. Multichannel STZA as part of the UAV allows not only to consider objects of interest in the visible and infrared ranges of the spectrum, but also to determine their geographical coordinates in the selected frame of reference, as well as the speed and direction of movement, if any.

There are two options for solving this problem.

The first is the constant delivery of the coordinates of the object of interest to the flight-navigation complex [6–9]. In this case, all the functionality of these parameters is implemented in the flight and navigation complex.

The second option is the transfer of the required flight trajectory to the flight and navigation complex. In this embodiment, the functionality of the observation parameters is implemented in the STZA (Table).

Table

Main technical characteristics of the «Sych» aviation technical vision system

Parameter name	STZA-1	STZA-2
A variant of the implementation of a gyro-stabilized optoelectronic platform (GOES)	two-stage, single-circuit	double-degree, double-circuit in azimuth
Root mean square error of stabilization	50 mrad	25 mrad
Interfaces: – management – transmission of video information	RS422/485, Ethernet, CAN Ethernet, HD-SDI	
Guidance speed (maximum)	300°/s	60°/s
Working temperature	от –40 °C до +50 °C	
Power consumption	150 watt	
Overall dimensions (diameter × height)	250×340 mm	
The weight	12.8 kg	16 kg
Visible camera – 1 (TV channel)		
resolution	1920 × 1080 pix. (RGB)	
field of view	2.3°–63.7°	
optical zoom	30×	
digital zoom	12×	
Visible camera – 2		
resolution	1920 × 1080 pix. (RGB)	1920 × 1080 pix. (RGB)
field of view	4.0°; 8.0°	2.4°; 4.8
optical zoom	2×	2×
Detection/recognition range (visible range cameras 1 and 2): – person – vehicle	 6200/2500 m 10000/5000 m	 6900/2600 m 10000/5800 m
Laser rangefinder		
working wavelength	1.53…1.57 μm	
measurement range	100…10000 m	
Measurement accuracy, not less	±5 m	
Thermal imager		
detector type	refrigerated	
resolution	640 × 512 pix.	
spectral range	3…5 μm	
field of view	2°…27°	
optical zoom	12×	
digital zoom	2×	
Detection/recognition range: – person – vehicle	 4200/1700 m 10000/4000 m	

The composition of the "Sych" STZA includes a gyro-stabilized platform with a useful opto-electronic load: two cameras of the visible range of a wide and a narrow field of view; thermal imaging module for working with objects of observation in the night mode; laser rangefinder module with a receiving and transmitting channel; built-in navigation system (*GPS*, *GLONASS*) (Figure 1) [10]. In the extended version, the STZA can be connected to a ground-based hardware and software complex.

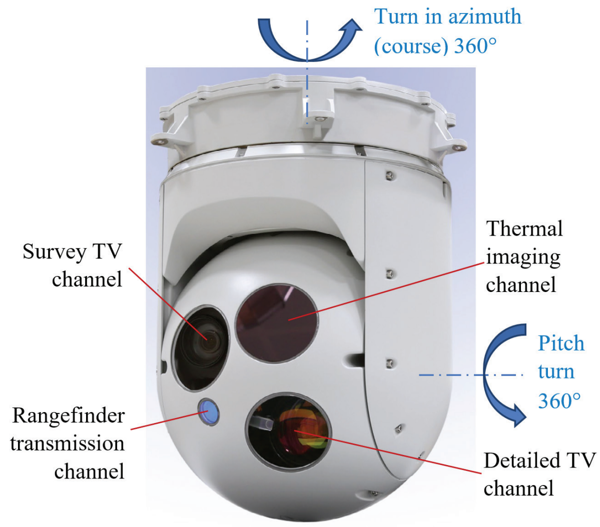

Figure 1 – Layout of the main modules of the aviation technical vision system on a gyro-stabilized platform

In the process of work, the monitoring object is automatically tracked; determination of the direction and speed of movement of the object; determination of the distance to the object and its characteristics (location coordinates and overall dimensions). For the convenience of transmission over the radio channel, hardware-software compression of video information is carried out. When accompanying an object during flight, a picture-in-picture display mode is possible for observation at different distances. If it is temporarily impossible to transmit a signal via a radio channel, recording of video information is provided in the built-in memory of the device in an equivalent volume of 20 hours of flight.

Analysis of the object of observation and the method of its support

An object of observation can be understood as any object resolved by an optoelectronic system under specific conditions. The tracking algorithm built into it allows updating the reference image, allowing you to continuously observe the object from different angles and distances. Partial overlap of the object (up to 50 % of the area) is not an obstacle to continuous tracking. Short-term full coverage is also possible, for example when driving behind trees, poles or road infrastructure. The vision system is capable of tracking objects moving in a tangential direction at a speed of more than 100 km/h at a distance of at least 60 m. The maximum flight altitude is limited by the tactical and technical characteristics of the UAVs.

The coordinates of the object are calculated by the STZA on-board computer with access to the signals of the global navigation satellite system. If the signal from the satellites is noisy, distorted or absent altogether, then for a limited period of time the correct operation of the device is still possible if an inertial module with a magnetic sensor is used as part of it.

Determination of the position of the observed object is based on solving a direct geodetic problem. The reference point is the UAVs coordinates received from the navigation module (Figure 2).

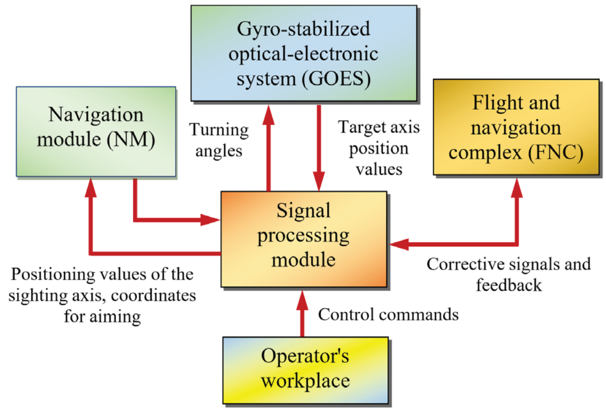

Figure 2 – Scheme of information exchange when implementing the control algorithm for unmanned aerial vehicles in the tracking mode

To calculate the azimuth and spherical distance to the object, it is necessary to convert the line of sight vector from the body coordinate system to the global one. The starting vector is determined by the gimbal/camera rotation angles.

The orientation angles of the inertial module define the transition matrix from one basis to another. The resulting line of sight vector allows you to find the azimuth and angle of the observation point in the global coordinate system. These angles are referenced to the object relative to the north direction and the local horizon, respectively. Knowing the vertical angle and height of the UAVs above the ellipsoid, you can find the spherical distance to the point of intersection of the line of sight with the ellipsoid.

However, the object is rarely located strictly at zero height. For decoupling from the ellipsoid, a special elevation map is used.

Observation of the object is carried out during the capture by the automatic tracking machine. After capturing an object for tracking, the reference image of the object is the frame area corresponding to the capture rectangle. In this case, it is not necessary that the entire object falls into the rectangle. The capture algorithm works on any contrasting part belonging to the object. The tracking rectangle may not always be in the center of the video frame. A special algorithm allows you to move from the line of sight of the camera to the object anywhere in the frame.

The calculation of the speed and direction of movement is based on the change in the obtained coordinates of the object in time. Smoothing values is based on a linear approximation of the trajectory in a sliding window. The window size adjusts to the speed of movement. It is assumed that at high speeds the maneuverability of ground objects is limited. Therefore, the averaging window increases, reducing the effect of the random component of the error. When driving at low speeds, significant changes in direction are possible, so the averaging window decreases.

Used coordinate systems and their relationship

Providing the specified functionality of the navigation unit of the combined anti-jamming multisystem inertial-satellite navigation receiver is implemented by establishing the initial relationship between the following coordinate systems (CS): geocentric inertial (*i-frame*), geocentric (geodesic) rectangular connected to the Earth (*e-frame*), navigation (*n-frame*) and asso-ciated (*b-frame*).

An inertial coordinate system is an ideal reference frame in which ideal inertial sensors (accelerometers and gyroscopes) have zero readings. The inertial CS $X^iY^iZ^i$ has its origin in the center of the Earth and axes that do not rotate with respect to distant galaxies. Its Z^i axis is parallel to the Earth's axis of rotation and is directed towards the North Pole. The X^i axis is directed to the vernal equinox, and the Y^i axis forms a right orthogonal triple of vectors with the first two. The projections of vectors on the axis of this CS have a superscript *i* (*inertial*).

The geodetic coordinate system $X^eY^eZ^e$ has its origin at the center of mass of the Earth and an axis whose position is fixed in relation to the Earth. The axis X^e is directed to the midpoint of the reference meridian. The axis Z^e is parallel to the Earth's axis of rotation and is directed to the North Pole, and the axis Y^e forms with the first two a right orthogonal triple of vectors. The projections of vectors on the axis of this CS have the superscript *e* (*earth*). Geodetic coordinates are used to determine the position of an object on the Earth's surface. The position of a point is specified by latitude *B*, longitude *L* and altitude *H*. Latitude is determined by the angle formed by the normal to the Earth's reference ellipsoid and the equatorial plane. Reference ellipsoid is an approximation of the shape of the Earth's surface by an ellipsoid of revolution, used on a certain area of the earth's surface. Longitude is measured by the dihedral angle between the plane of the meridian passing through the point and the plane of the reference meridian.

The *WGS*-84 CS will be used as a geodetic. The radii of curvature of the reference ellipsoid CS *WGS*-84 R_M and R_N are calculated from the following relations:

$$R_M = a/(1-e^2\sin^2 B)^{1/2};$$

$$R_N = a(1-e^2)/(1-e^2\sin^2 B)^{3/2},$$

where $a = 6378137$ m – equatorial radius of the Earth; $e^2 = 6{,}694379990141\times10^{-3}$ – the square of the eccentricity of the earth ellipsoid; *B* – latitude of the point at which the radii of curvature of the reference ellipsoid are calculated.

The navigation coordinate system $X^nY^nZ^n$ is a local CS with a vertex aligned with the center of mass of the object. The axis X^n is directed to the north along a tangent to the meridian, the axis Y^n is directed to the parallel to the east. The axis Z^n is orthogonal to the reference ellipsoid and directed downward. Thus, the navigation CS is formed by the axes directed north-east-down (*north*, *east*, *down* – NED). The projections of vectors on the axis of this CS have a superscript *n* (*navigation*). The navigation CS rotates in the geodesic space with an angular velocity, associated with the rates of change in latitude *B* and longitude *L*, caused by the movement of the object relative to the quasi-elliptical surface of the Earth.

A coordinate system is a Cartesian coordinate system $X^bY^bZ^b$, the axes of which are directed along the construction axes of the object. The axis X^b

Devices and Methods of Measurements
2021, vol. 12, no. 1, pp. 46–57
A.A. Adnastarontsau et al.

coincides with the longitudinal axis of the object and is directed towards the front part, the axis Y^bcoincides with the transverse axis of the object and is directed to the right side, the axis Z^b is perpendicular to the plane X^bY^b and complements the CS to the right triplet (directed downward). The projections of vectors on the axis of this CS have the superscript *b* (*body*). The position of a body coordinate system relative to the navigation coordinate system is defined by three angles called roll, pitch, and heading angles. Heading angle Ψ – the angle measured in the horizontal plane X^nY^n from the axis X^n clockwise, to the projection of the longitudinal axis of the object on this plane. The pitch angle θ is measured in the vertical plane between the axis X^b and its projection onto the horizontal plane X^nY^n. The roll angle γ is measured in the transverse plane between the axis Y^n and the line of intersection of the specified plane with the horizon plane. When the right side of the object is below the horizontal plane, the roll is considered positive.

Algorithm for the integration of Global Navigation Satellite System and Strapdown Inertial Navigation System

Integration of Global Navigation Satellite System (GNSS) and Strapdown Inertial Navigation System (SINS) is carried out according to a loosely coupled scheme, when they work independently of each other, but contains a block that processes and corrects data from both systems. This is done using an extended Kalman filter (KF) [12–15].

The input of the KF receives the difference between the values of the velocities and coordinates obtained using the SINS and GNSS algorithm. The Kalman filter estimates errors in determining angular orientation, velocities and coordinates. These estimates are used to correct the values of the corresponding parameters in the SINS algorithm. The corrected values are fed to the system output (Figure 3).

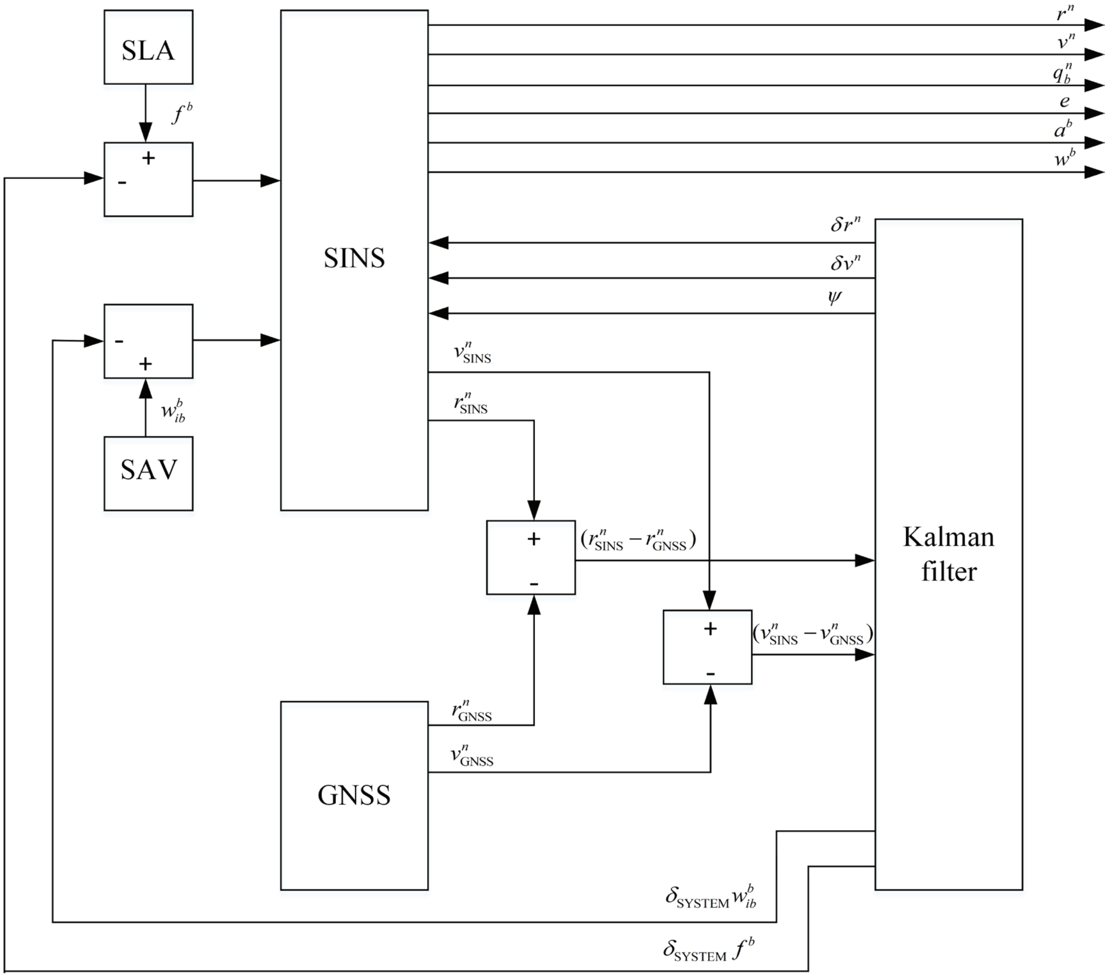

Figure 3 – Block diagram of the integration of a Strapdown Inertial Navigation System and Global Navigation Satellite System

The KF also makes it possible to evaluate the systematic components of the errors of inertial sensors, which makes it possible to correct the readings of the linear acceleration sensors (SLA) (accelerometer) and the angular velocity sensor (SAV) (gyroscope).

The refined values of the navigation parameters are used for subsequent calculations of the KF matrices.

The algorithm used for the loosely coupled inertial satellite navigation system is based on the error compensation scheme of the SINS algorithm.

To determine the errors of the SINS algorithm, difference measurements are used, obtained on the basis of data from both systems (SINS and GNSS). These measurements are formed by subtracting from the vectors of geodetic coordinates $\boldsymbol{r}^n_{\text{SINS}}$ and speed $\boldsymbol{v}^n_{\text{SINS}}$ of the same vectors obtained from the GNSS – $\boldsymbol{r}^n_{\text{GNSS}}$ and $\boldsymbol{v}^n_{\text{GNSS}}$.

The obtained difference measurements are processed by a discrete Kalman filter in accordance with Figure 3.

The KF state vector (output) has the following form:

$$\boldsymbol{x} = [(\delta\boldsymbol{r}^n)^T \cdot (\delta\boldsymbol{v}^n)^T \cdot (\psi)^T \cdot (\delta_{\text{SYSTEM}}\boldsymbol{w}^b_{ib}b^b)^T \cdot (\delta_{\text{SYSTEM}}\boldsymbol{f}^b)^T]^T,$$

where $\delta\boldsymbol{r}^n$ – vector of errors in determining coordinates using the SINS algorithm, size 3×1;

$\delta\boldsymbol{v}^n$ – vector of errors in determining the speed using the SINS algorithm, size 3×1;

$\boldsymbol{r}^n = [B, L, H]^T$ – vector-column of *WGS*-84 coordinates, where B – latitude, L – longitude, H – height (unit of measurement – [rad, rad, m], respectively);

$\boldsymbol{v}^n = [v_n, v_e, v_d]^T$ – column vector of velocity in the accompanying CS (unit of measurement – [m/s]);

$\boldsymbol{\psi}$ – vector of the final rotation of the azimuthal error and errors of constructing the vertical by the SINS algorithm, the size 3×1;

$\delta_{\text{SYSTEM}}\boldsymbol{w}^b_{ib}$ – vector of systematic components of gyroscope errors, size 3×1;

$\delta_{\text{SYSTEM}}\boldsymbol{f}^b$ – vector of systematic components of accelerometer errors, size 3×1;

$\boldsymbol{w}^b_{ib} = [w^b_{ibx}, w^b_{iby}, w^b_{ibz}]^T$ – vector-column of indications of a 3-axis SAV (unit of measurement – [rad/s]);

$\boldsymbol{f}^b = [f^b_x, f^b_y, f^b_z]^T$ – vector-column of readings of a 3-axis SLA (unit of measurement – [m/s^2]).

The KF measurement vector (input) has the following structure:

$$\boldsymbol{Z} = [(\boldsymbol{r}^n_{\text{SINS}} - \boldsymbol{r}^n_{\text{GNSS}})^T \cdot (\boldsymbol{v}^n_{\text{SINS}} - \boldsymbol{v}^n_{\text{GNSS}})^T]^T.$$

Each iteration of the KF is divided into two phases: extrapolation (prediction) and correction.

At the first stage, the state of the system is estimated at each moment of time based on the data of the previous iteration and the given dynamic model of the system (taking into account its inaccuracy).

The KF prediction stage is as follows:

$$\widehat{\boldsymbol{x}}_{k|k-1} = F_k\widehat{\boldsymbol{x}}_{k-1|k-1};$$
$$F_k = I_{15\times15} + A_k dt_k;$$
$$P_{k|k-1} = F_k P_{k-1|k-1} F_k^T + Q_k;$$
$$\tilde{A}_k = G_k dt_k;$$
$$Q_k = \tilde{A}_k Q \tilde{A}_k^T;$$
$$Q = \text{diag}(\sigma^2_f, \sigma^2_\omega),$$

where k – filtering step number;

$\widehat{\boldsymbol{x}}_{k|k}$ – predicted value of the KF state vector at the k-th moment of time, size 15×1;

F_k – the fundamental matrix of the state of the KF, size 15×15, describing the dynamic model of the system;

$P_{k|k-1}$ – the covariance matrix of the predicted vector of the state of the system at the current step k, size 15×15;

$\tilde{A}$ – transient perturbation matrix of the KF, size 15×6;

Q – process covariance matrix (model noise), size 6×6.

At the second stage (correction), based on new measurements, the predicted value is corrected (also taking into account the inaccuracy and noisiness of this information). The initial conditions at the current iteration of the functioning of the KF algorithm are the assessment of the system state (observation matrix) and the error in the assessment of the previous iteration. The estimation error is the measurement noise covariance matrix R_k, in which the variances of the corresponding vector components are found on the diagonal.

After calculating the matrix of gains K_k, the system estimate is updated: the KF state vector $\widehat{\boldsymbol{x}}_{k|k}$ and the covariance error matrix $P_{k|k}$ are updated for the current and subsequent iterations.

The stage of KF correction is as follows:

$$R_k = \mathrm{diag}(\sigma^2_{rkGNSS}, \sigma^2_{vkGNSS});$$
$$\tilde{\boldsymbol{y}}_k = \boldsymbol{z}_k - H_k \hat{\boldsymbol{x}}_{k|k-1};$$
$$K_k = P_{k|k-1} H_k^T (H_k P_{k|k-1} H_k^T + R)^{-1};$$
$$\hat{\boldsymbol{x}}_{k|k} = \hat{\boldsymbol{x}}_{k|k-1} + K_k \tilde{\boldsymbol{y}}_k;$$
$$P_{k|k} = (I_{15\times15} - K_k H_k) P_{k|k-1},$$

where σ_{rGNSS} – Root mean square (RMS) vector of errors in determining geodetic coordinates using an GNSS receiver;

σ_{vGNSS} – RMS vector of the errors in determining the speed using the GNSS receiver;

$\tilde{\boldsymbol{y}}$ – vector of deviation of the measurement result from the extrapolation result, size 6×1;

$\hat{\boldsymbol{x}}_{k|k}$ – estimate of the state vector of the KF at the k-th moment of time, size 15×1;

$P_{k|k}$ – covariance matrix of the system state vector estimate, size 15×15.

In the proposed algorithm, the system of linearized differential equations of errors of the SINS algorithm is used as the equations of state of the system in the KF. The error equations set the relationship between the errors of the elements and the inaccurate input of the initial conditions, on the one hand, and the errors of the SINS output data, on the other. This choice made it possible to estimate not only the coordinate and velocity errors of the SINS, but also the angular errors and systematic errors of the inertial sensors, based on the difference signals of coordinates and velocities. That is, despite the absence of direct information about these errors in the measurement vector, the information about the object's orientation in space is corrected.

The operation algorithm of the navigation unit is shown in Figure 4.

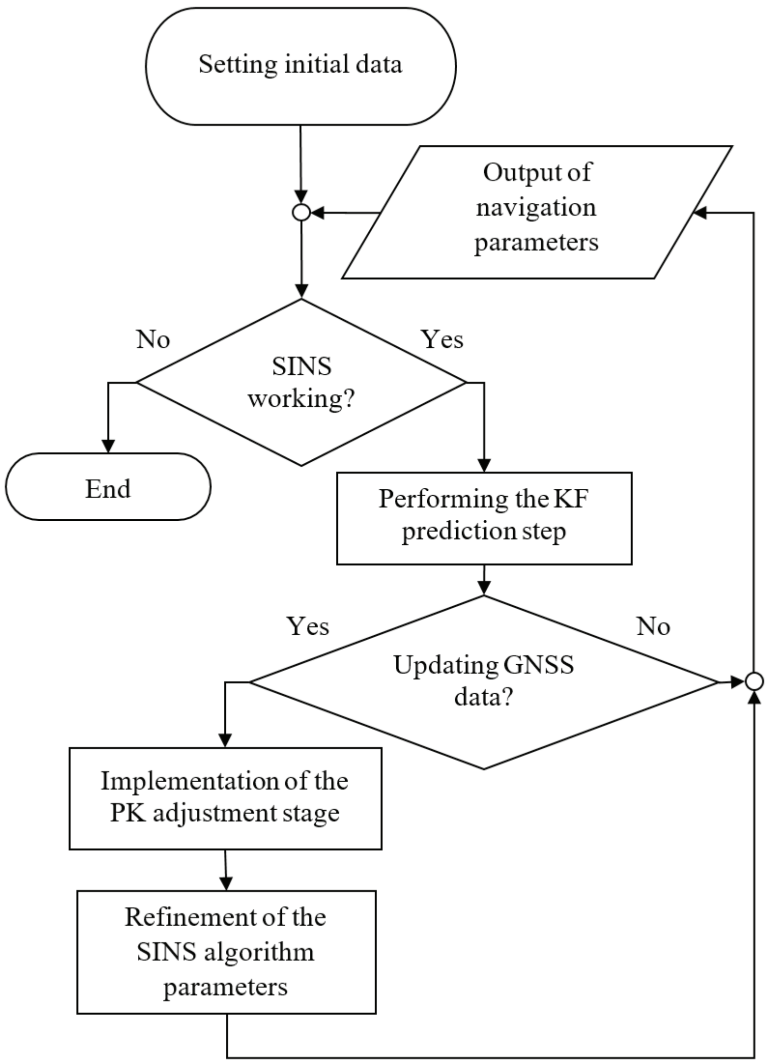

Figure 4 – Block diagram of the navigation block algorithm

Despite the fact that the frequency of the navigation solution issuance by the GNSS receiver is lower than the SINS operating frequency, the use of the KF algorithm made it possible not to carry out additional interpolation of navigation information from the GNSS receiver. This is achieved due to the fact that the KF prediction stage is performed with the frequency of receiving information from the SINS. And the stage of correction is performed upon receipt of the GNSS measurements. Thus, at the moments of arrival of information from the GNSS, both prediction based on the given dynamics of the system and the vector of measurements are used to estimate the state vector. At other times, the state vector is estimated only on the basis of the given dynamics of the system. Calculation results are issued on request via the *RS*485 interface.

Navigation solution software

The navigation module has built-in specialized software for the *FreeRTOS* real-time multitasking operating system, which provides the formation of a navigation solution (coordinates, speed, orientation) based on data from the receiving and measuring module of the Global Navigation Satellite System and data from the 6-axis MEMS sensor *STIM*300, as well as determining the orientation of the object and the possibility of information exchange (receiving data and control commands, issuance of navigation parameters and data on technical condition).

After turning on the power supply (about 0.5 s), a rough alignment of the initial parameters for SINS is carried out. At the stage of rough alignment, the roll and pitch angles are determined according to the readings of SLA and SAV. In this case, the initial coordinates and the heading angle take the values set by default, the velocity components are equal to zero. If an alignment by GNSS is used, the rough alignment timer must be set for more than 1 min (time sufficient to initialize the GNSS receiver) (Figure 5).

At the stage of exact alignment, the roll and pitch orientation angles are specified. It is recommended to set the exact alignment timer in the range of 10–20 s.

The input data for the program are:

– SLA and SAV data received from *STIM*300, which are received via the *UART* interface and have a binary representation. For a description of the data format, see the *STIM*300 documentation. Data is transmitted at 250 Hz without request. Data decoding is done in the *STIMParser* class;

– data of the GNSS-receiver. The data is received via the *UART* interface and has a binary representation. Data is transmitted at a frequency of 1 Hz, processed by *NTLBinaryParser* drivers.

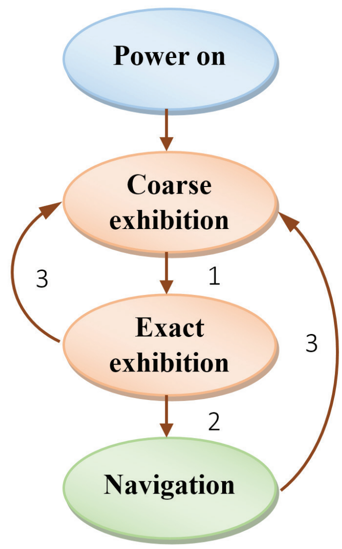

Figure 5 – Graph of states of the navigation module: 1 – activation of the rough exhibition timer; 2 – triggering of the exact exhibition timer; 3 – command options: "Alignment on Global Navigation Satellite System", "Alignment on known coordinates", "Alignment on known coordinates and course", "Alignment on Global Navigation Satellite System and course"

The general structure of the program is shown in Figure 6.

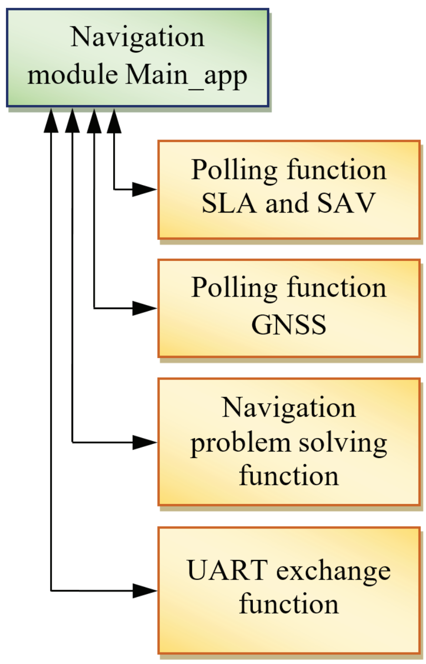

Figure 6 – Software structure of the navigation module

SLA and SAV polling function (*stimChanByteRx*) – a function for controlling the *STIM*300 module. Provides initialization of *STIM*300, reception of data of angular velocities and linear accelerations and their return through variables of the *STIMParser* (*stim*300*_parser.h*).

GNSS polling function (*nt*1058*_A_ByteRx*, *nt*1058*_B_ByteRx*) – a function for controlling the GNSS receiver module. Implements receiving and returning data through the *nav_sol_t* structure (*ntlbinary_parser.h*).

Function for solving the navigation problem (*sinsUpdate*) – provides the calculated data through the nav_data_t structure (*common_data.h*).

UART exchange functions (*navChanByteRx*, *navChanTx*) – a set of functions that implement the information exchange protocol via the *UART* interface (*RS*485).

The output is a navigation solution:

– latitude *WGS*-84;

– longitude *WGS*-84;

– height *WGS*-84;

– roll angle;

– pitch angle;

– heading angle;

– northern, eastern and vertical components of velocities in the navigation coordinate system;

– longitudinal, vertical and transverse components of free accelerations in a bound coordinate system;

– longitudinal, vertical and transverse components of angular velocities in the associated coordinate system.

– the quaternion of transformation from the associated coordinate system to the navigation one.

The output data is transmitted on request via the *RS*485 interface, in accordance with the communication protocol.

Conclusion

The proposed multispectral optical-electronic system of technical vision based on an aviation gyro-stabilized platform with two degrees of mobility and a two-loop stabilization system provides stable detection and tracking of objects at a distance of up to 10000 m in the visible and infrared ranges of the spectrum.

The tracking algorithm allows updating the reference image, allowing you to continuously observe the object from different angles and distances. Partial overlap of the object (up to 50 % of the area) is possible, as well as its short-term full coverage with other objects.

An algorithm for the integration of a Global Navigation Satellite System and a Strapdown Inertial Navigation System based on the extended Kalman filter has been developed, through which the errors in determining the angular orientation, velocities and coordinates are estimated. These estimates are further used to correct the values of the corresponding parameters in the algorithm of the Strapdown Inertial Navigation System.

Specialized software has been developed in the *FreeRTOS* environment, which provides the calculation of a navigation solution (coordinates, speed, orientation) based on data from the receiving and measuring module of the Global Navigation Satellite System and data from the 6-axis MEMS sensor *STIM*300.

References

1. *Obrabotka izobrazheniy v aviatsionnykh sistemakh tekhnicheskogo zreniya* [Image processing in aeronautical vision systems]. Ed. Kostyashkina L.N., Nikiforova M.B. M.: FIZMATLIT Publ., 2016, 234 p.

2. Damantsev Ye. *Neraskrytyye vozmozhnosti proyekta "Sych". Unikal'nyy udarno-razvedyvatel'nyy kompleks na baze Su-34. "Voyennoye obozreniye". Analitika.* [Undiscovered Possibilities of the "Sych" Project. A unique strike and reconnaissance complex based on the Su-34. "Military Review". Analytics]. 31.01.2020 (in Russian).

3. Advisory Circular AC №:20-167A. U.S. Department of Transportation Federal Aviation Administration. 12.06.2016, 104 p.

4. David H. Titterton, John L. Weston. Strapdown Inertial Navigation Technology, 2004, 2nd ed., *Radar, sonar, navigations & avionics*, 594 p.

5. Paul G. Savage. Strapdown Associates, 2000, vol. 1, 2nd edition, 1556 p.

6. Volkov V.G. *Vertolotnyye optiko-elektronnyye sistemy nablyudeniya i razvedki* [Helicopter optoelectronic surveillance and reconnaissance systems]. *Journal "Special Technique"*, 2001, no. 3 (in Russian). Available at: http://www.bnti.ru/showart.asp?aid=510&lvl=09.01.&p=1 (accessed 22.02.2021).

7. Makarchenko O.F., Makarchenko F.I., Nilov A.V., Rumyantsev G.N., Sukhov S.V. *Sposob uvelicheniya diapazona uglov povorota izdeliya otnositel'no girostabilizirovannoy platformy, ustanovlennoy na izdelii v kardannovom podvese* [A method of increasing the range of angles of rotation of the product relative to the gyro-stabilized platform installed on the product in a gimbal]. Patent RF, no. 2552857, 2015.

8. Burets G.A., Gorokhov M.M., Denisov R.N., Nuzhin A.V., Pleshanov Y.V., Puysha A.E. *Optiko-elektronnyy sledyashchiy koordinator* [Optoelectronic tracking coordinator]. Patent RF, no. 2476826, 2013.

9. Amelin K.S. A method of orienting an ultralight UAVs with a rare update of its position data [*Metod oriyentirovaniya sverkhlogkogo BPLA pri redkom obnovlenii dannykh o yego mestopolozhenii*]. Saint Petersburg State University, 2014, pp. 3–14 (in Russian). Available at: https://www.math.spbu.ru/user/gran/soi10_2/Am10_2.pdf (accessed: 22.02.2021).

10. *Sozdaniye sistemy tekhnicheskogo zreniya aviatsionnoy, shifr "Sych"* [Creation of an aviation technical vision system, code "Sych"]. JSC "Peleng". State rubricator of scientific and technical information SRSTI:59.14.29. from 21.08.2017. Register of scientific research, experimental design and experimental technological work registered in 2017 / ed. A.G. Shumilina. Minsk: State Institution "BelISA" Publ., 2018, 109 p.

11. Lukatsevich K. *Tochno na tsel'. Pritsel'nyye kompleksy OAO «Peleng» sootvetstvuyut samym vysokim trebovaniyam. Oboronno-promyshlennyy kompleks Rossii* [Right on target. The sighting systems of JSC "Peleng" meet the highest requirements. Defense industrial complex of Russia]. Special information and analytical project. № 2(23), July 2020, 70 p.

12. Bagmut I.A. *Nastroyka fil'tra Kalmana v zadache korrektsii inertsial'nykh izmereniy v integrirovannoy navigatsionnoy sisteme* [Adjusting the Kalman filter in the problem of correcting inertial measurements in an integrated navigation system]. Bulletin of the National Technical University "KhPI": collection of scientific papers. Thematic issue: Dynamics and strength of machines. Kharkov: NTU "KhPI" Publ., 2011, no. 63, pp. 13–21 (in Russian).

13. Mkrtchyan V.I. *Nastroyka fil'tra Kalmana dlya otsenivaniya oshibki BINS po kursu* [Adjusting the Kalman filter for estimating the SINS error at the rate]. *Modern science: actual problems of theory and practice. Series: Natural and Technical Sciences*,2018, no. 6, pp. 24–28 (in Russian).

14. N. Al Bitar, Gavrilov A.I. *Sravnitel'nyy analiz algoritmov kompleksirovaniya v slabosvyazannoy inertsial'no-sputnikovoy sisteme na osnove obrabotki real'nykh dannykh* [Comparative analysis of integration algorithms in a loosely coupled inertial-satellite system based on real data processing]. *Gyroscopy and navigation*, 2019, vol. 27, no. 3(106), pp. 31–52 (in Russian).
DOI: 10.17285/0869-7035.0001

15. Benkafo A.S., Lobaty A.A. *Osobennosti primeneniya fil'trov Kalmana-B'yusi v kompleksakh oriyentatsii i navigatsii* [Features of Kalman-Bucy filters application in orientation and navigation complexes]. Belarusian State University of Informatics and Radioelectronics (BSUIR) reports, 2013, no. 5(75), pp. 67–71 (in Russian).

Evaluation of Nonuniformity of Elastic Properties of Sheets Made from Closed-Cell Polyolefin Foams by Acoustic Method

O.P. Bogdan[1], D.V. Zlobin[1], O.V. Murav'eva[1,2], S.M. Molin[2], A.V. Platunov[1]

[1]*Kalashnikov Izhevsk State Technical University,
Studencheskaya str., 7, Izhevsk 426069, Udmurt Republic, Russia*

[2]*Udmurt Federal Research Center, Ural Branch of the Russian Academy of Sciences,
Tatiana Baramzina str., 34, Izhevsk 426067, Udmurt Republic, Russia*

Received 19.12.2020
Accepted for publication 17.02.2021

Abstract

The widespread use of polyolefin foams in strategically important industries is due to their high thermal, sound and vibration insulation properties. The aim of the work was to evaluate the non-uniformity of elastic properties over the area of sheets of polyolefin foams of various types using the acoustic non-contact shadow amplitude method of testing and confirmation by the structural analysis method.

The article presents the developed installation and a new method of non-contact acoustic testing of sheets made of closed-cell polyolefin foams based on recording the amplitude of the pulse that passed through the sheet and allowing to assess to the unevenness of its elastic properties during scanning. Studies of uneven elastic properties were carried out on sheets of closed-cell polyolefin foams of the *ISOLON* 500 and *ISOLON* 300 brands which differ in material and manufacturing technology (technique of cross-linking, method and multiplicity of foaming).

It is shown that the absolute amplitude of the signal and its spread relative to the average value is affected by the structure of the foam polyolefin material and its heterogeneity over the area of the studied sheet determined by the production technology which is confirmed visually using microscopy.

Studies have shown the effect on the indications unevenness of the method of obtaining and the apparent density of the material. It is shown that the most uneven elastic properties and structure belong to sheets of polyolefin foam obtained by chemical cross-linking technology (the unevenness of Δ was 6.5 %). Among the physically cross-linked sheets of polyolefin foam the most uniform in structure and elastic properties are samples made of ethylene vinyl acetate with Δ = 3.8 %, as well as sheets with a high foaming rate (Δ = 3.9 %). The unevenness of structure of the studied sheets of polyolefin foams was confirmed by optical microscopy of sections in two mutually perpendicular directions.

Keywords: polyolefin foam, elastic properties, acoustic shadow method, unevenness, structure.

DOI: 10.21122/2220-9506-2021-12-1-58-66

Адрес для переписки:
Богдан О.П.
Ижевский государственный технический университет имени М.Т. Калашникова,
ул. Студенческая, 7, г. Ижевск 426069, Россия
e-mail: Lelik_2005_05@mail.ru

Address for correspondence:
Bogdan O.P.
Kalashnikov Izhevsk State Technical University,
Studencheskaya str., 7, Izhevsk 426069,
Udmurt Republic, Russia
e-mail: Lelik_2005_05@mail.ru

Для цитирования:
O.P. Bogdan, D.V. Zlobin, O.V. Murav'eva, S.M. Molin, A.V. Platunov.
Evaluation of Nonuniformity of Elastic Properties of Sheets Made from Closed-Cell Polyolefin Foams by Acoustic Method.
Приборы и методы измерений.
2021. – Т. 12, № 1. – С. 58–66.
DOI: 10.21122/2220-9506-2021-12-1-58-66

For citation:
O.P. Bogdan, D.V. Zlobin, O.V. Murav'eva, S.M. Molin, A.V. Platunov.
Evaluation of Nonuniformity of Elastic Properties of Sheets Made from Closed-Cell Polyolefin Foams by Acoustic Method.
Devices and Methods of Measurements.
2021, vol. 12, no. 1, pp. 58–66.
DOI: 10.21122/2220-9506-2021-12-1-58-66

Devices and Methods of Measurements
2021, vol. 12, no. 1, pp. 58–66
O.P. Bogdan et al.

Оценка неравномерности упругих свойств листов из закрытоячеистых пенополиолефинов акустическим методом

О.П. Богдан[1], Д.В. Злобин[1], О.В. Муравьева[1,2], С.М. Молин[2], А.В. Платунов[1]

*[1]Ижевский государственный технический университет имени М.Т. Калашникова,
ул. Студенческая, 7, г. Ижевск 426069, Россия*

*[2]Удмуртский федеральный исследовательский центр Уральского отделения Российской академии наук,
ул. им. Татьяны Барамзиной, 34, г. Ижевск 426067, Россия*

*Поступила 19.12.2020
Принята к печати 17.02.2021*

Широкое использование пенополиолефинов в стратегически важных отраслях промышленности обусловлено их высокими тепло-, звуко- и виброизоляционными свойствами. Целью работы являлась оценка неравномерности упругих свойств по площади листов пенополиолефинов различных типов с использованием акустического бесконтактного теневого амплитудного метода контроля и подтверждением методом структурного анализа.

Разработаны установка и новая методика бесконтактного акустического контроля листов из закрытоячеистых пенополиолефинов, основанная на регистрации амплитуды импульса, прошедшего сквозь лист, и позволяющая оценить неравномерность его упругих свойств в процессе сканирования. Исследования неравномерности упругих свойств проведены на листах из закрытоячеистых пенополиолефинов марки *ISOLON* 500 и *ISOLON* 300, различающиеся материалом и технологией изготовления (способ сшивки, метод и кратность вспенивания).

Показано, что на абсолютную амплитуду сигнала и её разброс относительно среднего значения влияет структура материала пенополиолефина и её неоднородность по площади исследуемого листа, определяемая технологией производства, что подтверждено визуально с использованием микроскопии.

Исследования показали влияние на неравномерность показаний способа получения и кажущейся плотности материала. Показано, что наиболее неравномерные упругие свойства и структуру имеют листы из пенополиолефинов, полученных по технологии химической сшивки (неравномерность Δ составила 6,5 %). Из физически сшитых листов пенополиолефинов наиболее равномерными по структуре и упругим свойствам являются образцы, изготовленные из этиленвинилацетата с Δ = 3,8 %, а также листы с высокой кратностью вспенивания (Δ = 3,9 %). Неравномерность структуры исследованных листов пенополиолефинов подтверждена оптической микроскопией срезов в двух взаимно перпендикулярных направлениях.

Ключевые слова: пенополиолефин, упругие свойства, акустический теневой метод, неравномерность, структура.

DOI: 10.21122/2220-9506-2021-12-1-58-66

Адрес для переписки:
*Богдан О.П.
Ижевский государственный технический университет имени М.Т. Калашникова,
ул. Студенческая, 7, г. Ижевск 426069, Россия
e-mail: Lelik_2005_05@mail.ru*

Address for correspondence:
*Bogdan O.P.
Kalashnikov Izhevsk State Technical University,
Studencheskaya str., 7, Izhevsk 426069,
Udmurt Republic, Russia
e-mail: Lelik_2005_05@mail.ru*

Для цитирования:
O.P. Bogdan, D.V. Zlobin, O.V. Murav'eva, S.M. Molin, A.V. Platunov.
Evaluation of Nonuniformity of Elastic Properties of Sheets Made from Closed-Cell Polyolefin Foams by Acoustic Method.
Приборы и методы измерений.
2021. – Т. 12, № 1. – С. 58–66.
DOI: 10.21122/2220-9506-2021-12-1-58-66

For citation:
O.P. Bogdan, D.V. Zlobin, O.V. Murav'eva, S.M. Molin, A.V. Platunov.
Evaluation of Nonuniformity of Elastic Properties of Sheets Made from Closed-Cell Polyolefin Foams by Acoustic Method.
Devices and Methods of Measurements.
2021, vol. 12, no. 1, pp. 58–66.
DOI: 10.21122/2220-9506-2021-12-1-58-66

Introduction

Polyolefin foam is a cross-linked gas-filled polymer material with a closed or open cellular structure. Polyolefin foams are featured by low values of density, thermal conductivity, water absorption, vapor permeability, high chemical resistance, flexibility and elasticity, sound-absorbing properties, resistance to temperature and mechanical influences, as well as environmental safety. The non-uniformity of the elastic properties of polyolefin foams can lead to the fact that the latter will not meet the requirements of heat and sound insulation and vibration damping which is unacceptable for particularly important strategic objects.

Technical requirements for the production of polyolefin foams are defined by GOST R 56729-2015 (EN 14313: 2009)) which involves selective testing of characteristics. The main methods of studying the sound absorption of polyolefin foams are tests in a reverberation chamber [1] (GOST 31704-2011 (EN ISO 354: 2003)) and tests in an impedance tube with two or four microphones [2, 3]. None of the methods regulated by the state standards allows us to assess the uneven properties of the produced sheets of polyethin foams.

Due to the fact that most of the characteristics of polyethin foams are related to their mechanical properties, the acoustic method of research is the most physically justified since it uses elastic vibrations of the same physical nature. Therefore the study of the acoustic properties of polyolefin foams is of particular interest to scientific schools. Most studies of the acoustic properties of polyolefin foams are limited to the study of sound absorption under various conditions and its dependence on porosity, apparent density, tortuosity of pores, and radiation frequency [1–9]. A number of studies [1–9] show the possibility of improving the acoustic characteristics (sound absorption, sound attenuation, and vibration damping property) by optimizing the structure and synthetic formula with various inorganic and organic fillers [3, 10–13]. The influence of porosity and tortuosity of pores on the speed of sound, Poisson's ratio, elastic modulus, and radiation frequencies is studied [14–17].

The questions of the uniformity of the distribution of acoustic properties over the thickness of polyolefin foams are evaluated using the simulation of the macroscopic foaming process [18, 19]. There is information about studies of the uneven acoustic properties in gas pipeline metals, which characterize the tendency to failure [20, 21].

The aim of the work was to evaluate the non-uniformity of elastic properties over the area of sheets of polyolefin foams of various types using the acoustic non-contact shadow amplitude method of testing and confirmation by the structural analysis method.

Materials and methods

The object of the study was sheets of polyolefin foam, which is a hydrophobic polymer material obtained by chemical or physical cross-linking. Chemical cross-linking of polyolefin foam is realized by appending chemicals into the material, while the sheet has a rough surface and a closed fine-pored structure (pore size < 1 mm). Physical (radiation) cross-linking of polyolefin foam is realized by irradiating the material with an electron beam, while the sheet after processing has a smooth surface and a closed microporous structure. The pore size of polyolefin sheets depends on the multiplicity of foaming K of the material, which occurs in a special vertical or horizontal furnace and determines the apparent density of the material ρ (TI 2244-037-00203476-2012 Cross-linked polyethylenes of the *ISOLON* 500 and *ISOLON* 300 brands):

$$\rho = \frac{N}{K},$$

where $N = 1000$ kg/m^3.

The greater the multiplicity of foaming, the larger the size of the pores in the sheets of polyolefin foam and the lower their apparent density.

Studies to assess the uneven properties of polyolefin foam by the shadow acoustic method were carried out on closed-cell samples of the *ISOLON* brand, manufactured according to TI 2244-037-00203476-2012 with dimensions of 180×150×4 mm. The samples are made of polyethylene foam and ethylene vinyl acetate obtained by different methods (physically and chemically cross-linked, foamed in a horizontal and vertical furnace). The properties of the studied sheets of polyolefin foams are presented in Table 1.

The estimation of the unevenness of the samples of polyolefin foams is realized using the contactless acoustic amplitude shadow transmission method [22, 23], based on the registration of changes in the amplitude of the acoustic signal that passed through the sample.

Devices and Methods of Measurements
2021, vol. 12, no. 1, pp. 58–66
O.P. Bogdan et al.

Table 1

Properties of the studied sheets of polyolefin foams

Grade	Stock	Type of cross-linking	A method of producing	Thickness, mm	Foaming multiplicity K	Apparent density ρ, kg/m^3
ISOLON 500 3004 *AV W*	polyethylene foam	physically cross-linked	foamed on a vertical furnace	4	30	33
ISOLON 500 1004 *AV W*	polyethylene foam	physically cross-linked	foamed on a vertical furnace	4	10	100
ISOLON 500 1504 *SV W*	ethylene vinylacetate	physically cross-linked	foamed on a vertical furnace	4	15	66
ISOLON 500 2004 *AH B*	polyethylene foam	physically cross-linked	foamed on a horizontal furnace	4	20	50
ISOLON 300 2004 *AH D*	polyethylene foam	chemically cross-linked	foamed on a horizontal furnace	4	20	50

The block diagram of the experimental setup for the study of uneven sheets of foam is shown in Figure 1. An electric pulse from the probing pulse generator 1 is fed to the radiating acoustic converter 2. The emitted acoustic wave passes through a sheet of polyolefin foam (object of study 3) and is received by an acoustic transducer 4, which converts it into an electrical signal. The registered electrical pulse enters the processing unit 5, in which it is amplified and its amplitude is recorded using a peak detector, the value of which is transmitted to the ADC of the microcontroller 6. Data from the microcontroller is transmitted to a personal computer 7, on the screen of which the measurement results are displayed using specialized software. Using a microcontroller 6, powered by a personal computer 7, the probe pulse generator 1 is also controlled.

A mandatory requirement is the use of identical emitting 2 and receiving 4 acoustic transducers located coaxially on opposite sides of the object of study 3. To minimize the influence of acoustic noise and interference on the measurement results, to increase the accuracy and reliability of the measurement, the object of study 3, emitting 2 and receiving 4 acoustic transducers are acoustically isolated using a sound-proof chamber 8.

Main characteristics of the developed experimental setup:

– informative parameter-the amplitude of the transmitted signal;

– type of acoustic transducer-W-06A;

– operating frequency range: 7–15 kHz;

– applied voltage to the emitter – 20 V;

– amplification constant- not less than 40 dB;

– method of excitation-delta pulse;

– protection against air acoustic interference;

– installation power supply-from the USB port of the main computer (+5 V);

– the distance between the emitter and the receiver – 35 mm;

– the diameter of the acoustic transducer is 40 mm.

To assess the unevenness of the elastic properties, a transverse-longitudinal scan of the sheet surface is performed through transducers with a step of 30 mm, with the exception of 15 mm at the edges in order to avoid the appearance of an edge effect.

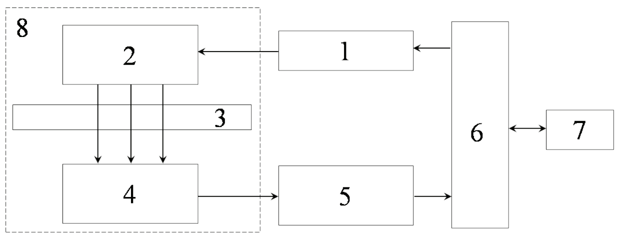

Figure 1 – Block diagram of the experimental setup: 1 – probe pulse generator; 2 – emitting acoustic transducer; 3 – object of study; 4 – receiving acoustic transducer; 5 – processing unit with amplifier and peak detector; 6 – microcontroller; 7 – personal computer; 8 – sound insulation chamber

The amplitude of the signal transmitted through the sheet of polyolefin foam depends on the structure and thickness of the object under study. In particular, for porous materials, acoustic energy losses will be affected by acoustic (elastic) properties (acoustic impedance, density, sound absorption, sound velocity, elastic modulus determined by the sheet structure – foaming coefficient, porosity, pore tortuosity coefficient, and other structural characteristics of the material [22, 23]. In this case, a local change in the elastic properties over the sample area leads to fluctuations in the amplitude of the transmitted signal during the scanning of the sheet. Thus, a local increase in the density of a sheet of polyolefin foam or a local decrease in the multiplicity of foaming (uneven foaming) leads to a decrease in the amplitude of the acoustic signal transmitted through the object relative to the average value.

In the case of an inhomogeneous porous layer, which includes a sheet of polyolefin foam, the coefficient of passage of an acoustic wave through the layer is more complex and can be described taking into account the Biot-Frenkel equation, the equation of the classical theory of elasticity for the case of two-phase media [16].

In addition to evaluating the uniformity of the properties of polyolefin foams, the developed method and experimental setup can be used to detect various defects in the production and operation of sheets, such as dents, cuts, foreign inclusions, and others [22].

Results and discussion

To assess the uniformity of the properties of the sheets of polyolefin foam during production, the amplitude of the transmitted signal through the object of study was measured. The measurements were carried out at 30 points over the area of the polyolefin sheet in two directions along the sheet (direction 1–6) and across the sheet (direction I–V). Average list penopoliuretana amplitudes of the transmitted signal are presented in Table 2. It is seen that the amplitude of the transmitted through the sheet signal is influenced by the type of stitching and the apparent sheet density at constant thickness of the sheet. For physically cross-linked sheets of polyolefin foam, a decrease in the amplitude of the transmitted signal is observed with an increase in the apparent density. Comparing sheets of polyolefin foam with the same apparent density (50 kg/m^3) obtained using a different type of cross-linking that affects the synthetic formula of the sample (physically cross-linked *ISOLON* 500 2004 *AH B* and chemically cross-linked *ISOLON* 300 2004 *AH D*), it can be concluded that chemically cross-linked polyolefin foam is more transparent to the acoustic wave, since it has a large amplitude of the transmitted signal in contrast to the physically cross-linked one, and therefore has worse sound-absorbing properties.

Table 2

The value of the average amplitude of the transmitted signal over a sheet of polyolefin foam

Grade	The average amplitude of the transmitted signal on the sheet $\bar{A}$, relative unit
ISOLON 500 3004 *AV W*	655
ISOLON 500 1004 *AV W*	236
ISOLON 500 1504 *SV W*	280
ISOLON 500 2004 *AH B*	262
ISOLON 300 2004 *AH D*	406

In order to make a comparative assessment of the degree of unevenness of the acoustic properties of the samples of polyolefin foam in a wide range of amplitudes, the measured values of the A_i amplitude of the transmitted signal were normalized by the average value of $\bar{A}$ for the studied sheet of polyolefin foam:

$$A_n = \frac{A_i}{\bar{A}}.$$

The results of scanning the studied sheets of polyolefin foam are presented in Figure 2 in the form of surfaces with isolines corresponding to a certain percentage of deviation from the average values. It can be seen that the most uneven in its pro-perties is the sheet of *ISOLON* 300 2004 *AH D* foam (Figure 2*e*) (chemically cross-linked foam, foamed on a horizontal furnace), for which the deviation of the normalized amplitude from the average value of the signal transmitted through the sheet reaches $\Delta = \pm 6.5$ %. In this case, the greatest deviation is observed along line I along the entire sheet (direction 1–6), as well as along line 5 in positions III–V.

The smallest deviation from the uniformity of pro-perties is observed in the samples *ISOLON* 500 3004 *AV W* (Figure 2*a*) $\Delta = \pm 3.9$ % (physically cross-linked foam, foamed on a vertical furnace), for which the value of $\Delta = \pm 3.9$ % and *ISOLON* 500 1504 *SV W* (Figure 2*c*) (ethylene vinyl acetate physically cross-linked, foamed on a vertical furnace, for which $\Delta = \pm 3.8$ %.

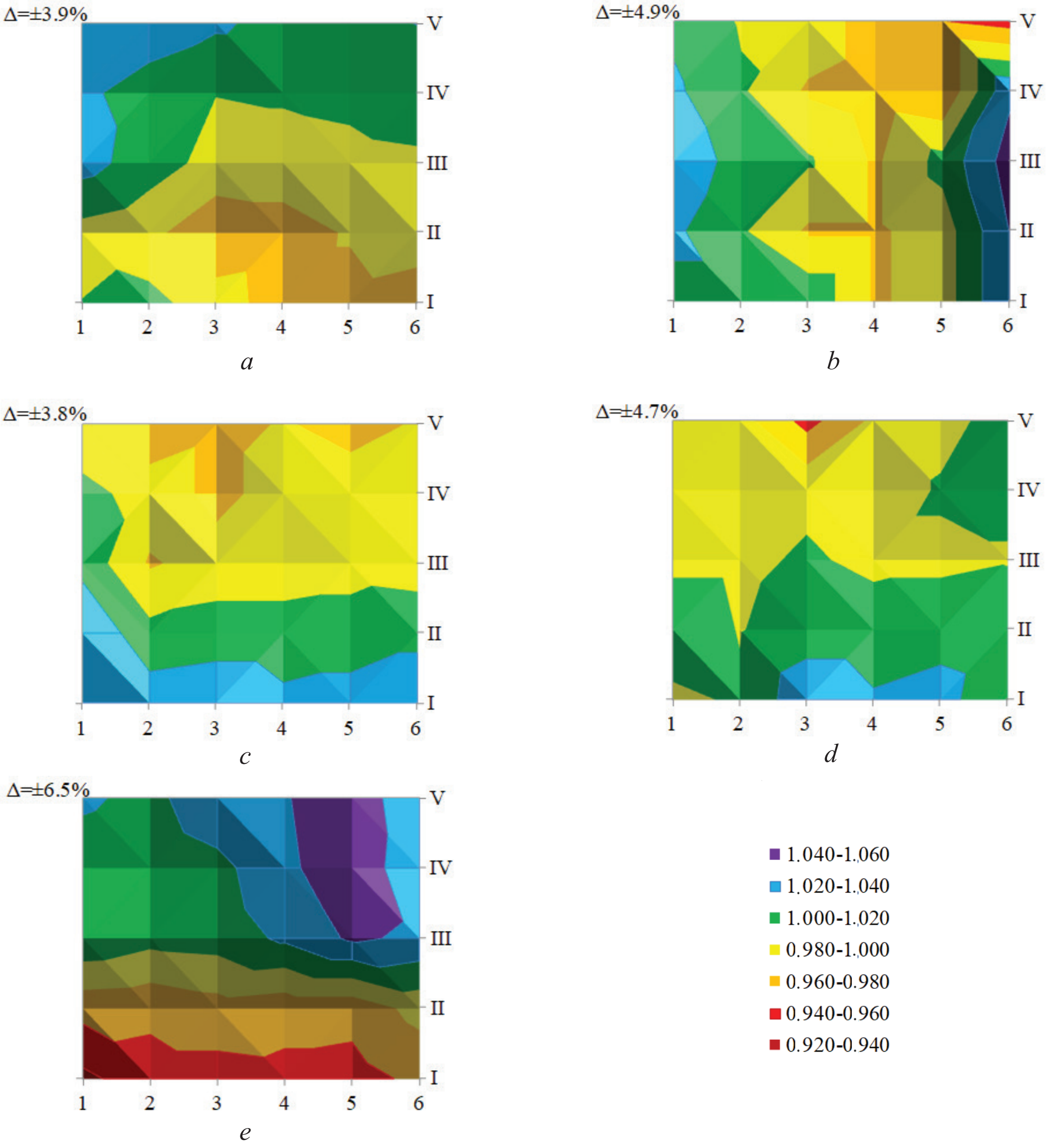

Figure 2 – Surfaces, describing the distribution of the normalized signal amplitude over the area of a sheet of polyolefin foam: *a* – *ISOLON* 500 3004 *AV W*; *b* – *ISOLON* 500 1004 *AV H*; *c* – *ISOLON* 500 1504 *SVJ*; *d* – *ISOLON* 500 2004 *A,B*; *e* – *ISOLON* 300 2004 *AH D*

Comparing the results of samples *ISOLON* 500 *AV* 3004 *W* (Figure 2*a*) and *ISOLON* 500 1004 *AV W* (Figure 2*b*), made of foam on one technology, but a different rate of expansion, and, consequently, the apparent density (Table 1), we can conclude that the increase in the multiplicity of foaming leads to a reduction in inequality in the worksheet, which made for a sample of *ISOLON* 500 *AV* 3004 *W* $\Delta = \pm 3.9$ %, and for *ISOLON* 500 1004 *AV* $\Delta = \pm 4.9$ %. This is due to the fact that at small values of the multiplicity of foaming, the spread of pore sizes in the sample is greater than at a large multiplicity of foaming.

The studied samples *ISOLON* 500 2004 *AH B* (Figure 2*d*) and *ISOLON* 300 2004 *AH D* (Figure 2*e*) are made of polyethylene foam foamed in a horizontal furnace, have the same foaming multiplicity of 20 and the same apparent density of 50 kg/m^3 (Table 1), but were produced using different cross-linking technologies (*ISOLON* 500 2004 *AH B* – physically cross-linked, *ISOLON* 300 2004 *AH D* – chemically cross-linked). All other things being equal, the chemical cross-linking of the polyethylene foam leads to an unevenness across the sheet of $\Delta = \pm 6.5$ %, while the physical cross-linking leads to $\Delta = \pm 4.7$ %.

To confirm the uneven foaming of the sheets of polyolefin foams, the structure was photographed using an Altami *MET* 1*M* metallographic microscope with a *WF*10*X*/22 mm eyepiece and a planachromatic

Devices and Methods of Measurements
2021, vol. 12, no. 1, pp. 58–66
O.P. Bogdan et al.

lens at infinity *PL L* 5*X*/0.12 with an increase of 50x and an operating distance of 26.10 mm with the following shooting parameters: the method of contrast in reflected light-polarization (polarized light), illumination – bar with light filter (blue light filter for samples *ISOLON* 500 3004 *AV W*, *ISOLON* 500 1004 *AV W*, *ISOLON* 500 1504 *SV W*, yellow light filter for samples *ISOLON* 500 2004 *AH B*, *ISOLON* 300 2004 *AH D*), image resolution – 1024×822. Photos of the structure of the sheets of polyolefin foams are shown in Figure 3.

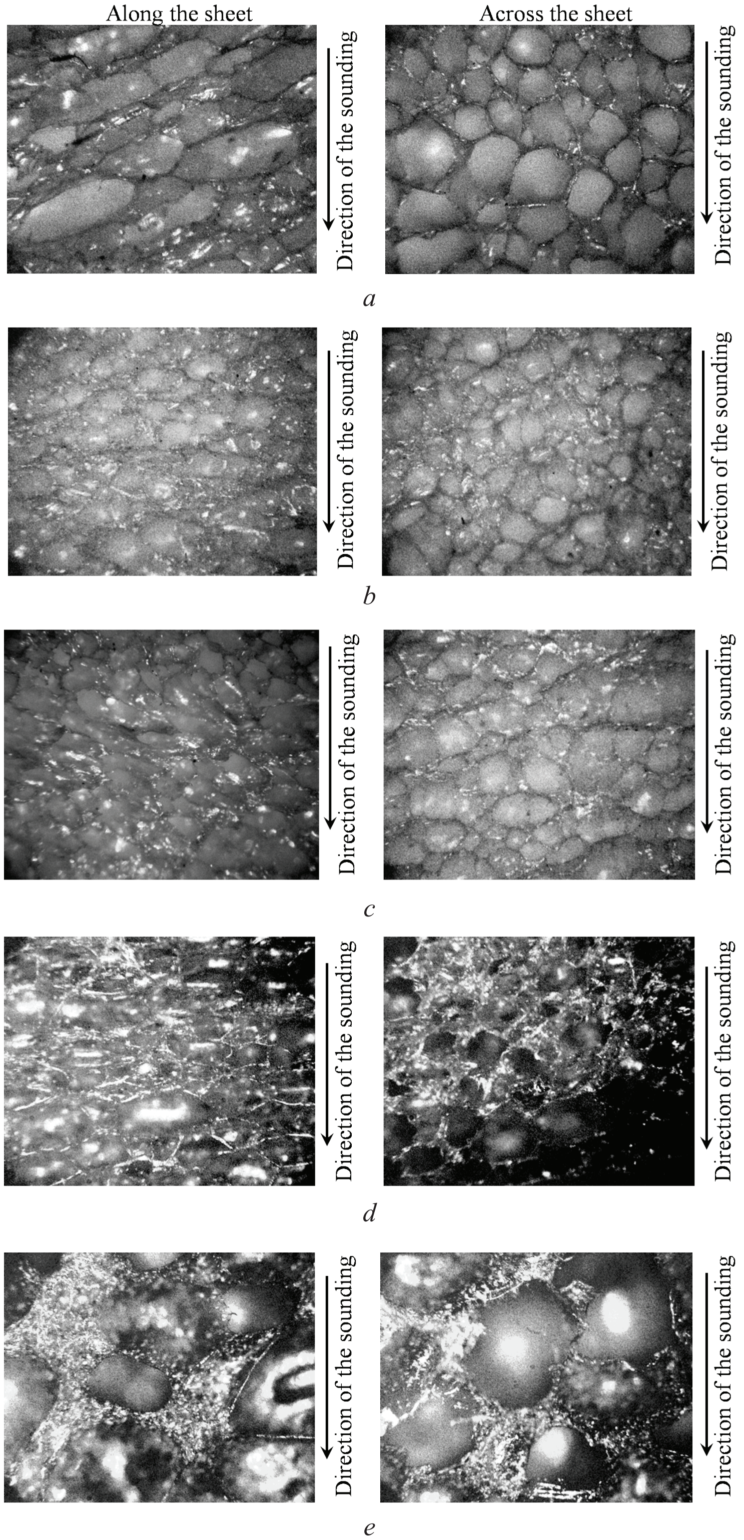

Figure 3 – Image of the structure of polyolefin foam sheets: *a* – *ISOLON* 500 3004 *AV W*; *b* – *ISOLON* 500 1004 *AV W*; *c* – *ISOLON* 500 1504 *SV W*; *d* – *ISOLON* 500 2004 *AH B*; *e* – *ISOLON* 300 2004 *AH D*

The study of the structure of the samples was carried out on sections which was made along the thickness of the sheet in two directions: along the sheet (direction 1–6) and across the sheet (direction I–V), while the direction of sounding of the sheet along the thickness is shown by an arrow. In all the samples studied, there is a clear orientation of the porous cells in the direction 1–6 along the sheet, which coincides with the direction of the rolled product during the foaming process. In this direction, the pores have an elongated shape, and the intercellular space conditionally has the form of channels, which contributes to better sound transmission along the sheet. In the direction I–V across the sheet, on the contrary, the porous cells have a more rounded appearance and sound transmission in this direction is difficult due to the absence of obvious channels in the intercellular space, which is typical for all the samples under study.

Analysis of the structure of the studied samples of polyolefin sheets in the direction of sounding (vertical image) shows that the size of the porous cells in the thickness of the sheet may differ several times for all samples. For sheets with minimal values of nonuniformity of amplitudes across the sheet $\Delta = \pm 4$ % (*ISOLON* 500 3004 *AV* (Figure 2*a*) and *ISOLON* 500 1504 *SV W* (Figure 2*c*)), it can be seen that the inter-cell space has a minimal spread in thickness. At the same time, the difference in the thickness of the space between the porous cells increases with an increase in the unevenness of the amplitudes along the sheet Δ. For example, for the sample *ISOLON* 500 1004 *AV W* (Figure 2*b*), it can be seen that the intercellular space around a small pore is thicker than near a large pore, this is due to the low value of the foaming multiplicity, as a result of which the pore growth did not have time to develop evenly over the entire thickness. For the samples *ISOLON* 500 2004 *AH B* (Figure 2*d*) and *ISOLON* 300 2004 *AH D* (Figure 2*e*), an increase in the difference in the thickness of the inter-cell space is also observed, especially for chemically cross-linked foamed polyethylene foam in a horizontal furnace.

Conclusion

A method and a device for assessing the uneven distribution of elastic properties of polyolefin sheets by the acoustic amplitude-shadow non-contact method have been developed.

It is shown that the absolute signal amplitude and its spread relative to the average value are affected by the structure of the polyolefin foam material and its heterogeneity over the area of the studied sheet, which is confirmed visually using microscopy. Studies have shown the effect on the unevenness of the indications of the method of production and the apparent density of the material. Based on the results obtained, it can be concluded that it is inappropriate to use chemically cross-linked sheets of polyolefin foam for strategically important areas of industry due to the large heterogeneity of properties, which can cause negative consequences. The lowest indicators of unevenness of the structure and elastic properties are the sheets of polyolefin foam obtained by physical cross-linking from a material of ethylene vinyl acetate with a low apparent density, and, consequently, a high foaming coefficient.

The developed method is quite simple to implement, has high reliability and reproducibility, and can be used not only to assess the unevenness of elastic properties, but also to detect various types of defects, including in production conditions, in order to prevent areas of the sheet with defects and a high degree of heterogeneity for further use.

Acknowledgments

The study was carried out with the financial support of the grant of the Russian science foundation No. 18-79-10122 (methodology and experimental setup, research results) and the Kalashnikov Izhevsk State Technical University within the framework of the scientific project No. PAV / 20-90-17 (structuroscopy of the studied samples) using the UNU "information and measurement complex for studies of acoustic properties of materials and products" (reg. number: 586308).

References

1. Kolbun N.V., Petrov S.N., Prudnik A.M. Electromagnetic and acoustic characteristics of multilayer materials for integrated protection systems. *Reports of the Belarusian State University of Informatics and Radioelectronics*, 2009, no. 3(41), pp. 79–85.

2. Kim B.-S., Seong Y., Park J. Modified two-thickness method for measurement of the acoustic properties of porous materials. *Applied Acoustics*, 2019, vol. 146, pp. 184–189. **DOI:** 10.1016/j.apacoust.2018.10.033

3. Tiuca A.-E., Vermeşana H., Gabora T., Vasileb O. Improved sound absorption properties of polyurethane foam mixed with textile waste. *Energy Procedia*, 2016, vol. 85, pp. 559–565. **DOI:** 10.1016/j.egypro.2015.12.245

4. Zhanga C., Lib J., Hua Z., Zhua F., Huanga Y. Correlation between the acoustic and porous cell morphology of polyurethane foam: Effect of interconnected porosity. *Materials & Design*, 2012, vol. 41, pp. 319–325. **DOI:** 10.1016/j.matdes.2012.04.031

5. Chen S., Zhu W., Cheng Y. Multi-Objective Optimization of Acoustic Performances of Polyurethane Foam Composites. *Polymers*, 2018, vol. 10, 788 p. **DOI:** 10.3390/polym10070788

6. Scarpa F., Bullough W.A., Lumley P. Rends in acoustic properties of iron particle seeded auxetic polyurethane foam. *Journal of Mechanical Engineering Science*, 2004, vol. 218, iss. 2, pp. 241–244. **DOI:** 10.1243/095440604322887099

7. Huangab K., Daiab L., Fanc Y. Applied Acoustics Characterization of noise reduction capabilities of porous materials under various vacuum conditions. *Applied Acoustics*, 2020, vol. 161, pp. 107–155. **DOI:** 10.1016/j.apacoust.2019.107155

8. Sgarda F., Castelb F., Atallac N. Use of a hybrid adaptive finite element/modal approach to assess the sound absorption of porous materials with meso-heterogeneities. *Applied Acoustics*, 2011, vol. 72, iss. 4, pp. 157–168. **DOI:** 10.1016/j.apacoust.2010.10.011

9. Chekkal I., Remillat C., Scarpa F. Acoustic properties of auxetic foams. *WIT Transactions on The Built Environment*, 2012, vol. 124, pp. 119–129. **DOI:** 10.2495/HPSM120111

10. Sua J., Zhenga L., Dengab Z. Study on acoustic properties at normal incidence of three-multilayer composite made of glass wool, glue and polyurethane foam. *Applied Acoustics*, 2019, vol. 156, pp. 319–326. **DOI:** 10.1016/j.apacoust.2019.07.016

11. Sung G., Kim J.H. Influence of filler surface characteristics on morphological, physical, acoustic properties of polyurethane composite foams filled with inorganic fillers. *Composites Science and Technology*, 2017, vol. 146, pp. 147–154. **DOI:** 10.1016/j.compscitech.2017.04.029

12. Shuming C., Yang J. The acoustic property study of polyurethane foam with addition of bamboo leaves particles. *Polymer composites*, 2018, vol. 39, iss. 4, pp. 1370–1381. **DOI:** 10.1002/pc.24078

13. Çelebi S., Küçük H. Acoustic Properties of Tea-Leaf Fiber Mixed Polyurethane Composites. *Cellular Polymers*, 2012, vol. 31, iss. 5, pp. 241–256. **DOI:** 10.1177/026248931203100501

14. Etchessahar M., Sahraoui S., Benyahia L., Tassin J.F. Frequency dependence of elastic properties of acoustic foams. *The Journal of the Acoustical Society of America*, 2005, vol. 117, iss. 3, p. 1114. **DOI:** 10.1121/1.1857527

15. Kumar R., Jin Y., Marre S., Poncelet O., Brunet T., Leng J., Mondain-Monval O. Drying kinetics and acoustic properties of soft porous polymer materials. *Journal of Porous Materials, Springer Verlag, inPress*, 2020. **DOI:** 10.1007/s10934-020-00987-w

16. Lenkov S.V., Molin S.M., Kopytov A.G. Resonance measurement technique for viscoelastic properties of damping materials of the porous closed cellular pe foam type. *Russian Journal of Nondestructive Testing*, 2014, vol. 50, iss. 3, pp. 180–185 (in Russian). **DOI:** 10.1134/S1061830914030061

17. Glushkov E.V., Glushkova N.V., Fomenko S.I. Influence of porosity on characteristics of rayleigh-type waves in multilayered half-space. *Acoustical Physics*, 2011, vol. 57, no. 2, pp. 230–240 (in Russian). **DOI:** 10.1134/S1063771011020059

18. Abdessalam H., Abbès B., Abbès F., Li Y., Guo Y.-Q. Prediction of acoustic properties of polyurethane foams from the macroscopic numerical simulation of foaming process. *Applied Acoustics*, 2017, vol. 120, pp. 129–136. **DOI:** 10.1016/j.apacoust.2017.01.021

19. Pauzin S.A. Accounting for anisotropy in the design of sound insulation of internal fences of high-rise buildings. *Privolzhsky nauchnyj zhurnal*, 2019, no. 4, pp. 40–45.

20. Pasmanik L.A., Kamyshev A.V., Radostin A.V., Zaitsev V.Yu. Parameters of acoustic inhomogeneity for non-destructive evaluation of the influence of manufacturing technology and operational damage on the metal structure. *Flaw detection*, 2020, no. 12, pp. 24–36. **DOI:** 10.31857/S0130308220120039

21. Zlobin D.V., Volkova L.V., Bogdan O.P., Zemskov T.I., Kazantsev S.V. Universal experimental setup for acoustic research. *Intelligent Systems in Production*, 2020, vol. 18, no. 2, pp. 28–36. **DOI:** 10.22213 / 2410-9304-2020-2-28-36

22. Bogdan O.P., Muravyeva O.V., Platunov A.V., Rysev D.S. Investigation of the characteristics of foam polyethylene sheets by acoustic methods. *Vestnik IzhSTU imeni M. T. Kalashnikov*, 2020, vol. 24, no. 2, pp. 61–68. **DOI:** 10.22213/2413-1172-2020-2-61-68

23. Bogdan O.P., Zlobin D.V., Muravieva O.V., Muraviev V.V., Volkova L.V. Acoustic and Eddy Current Methods of Nondestructive Testing of Thermally Expanded Graphite Sheets. *IOP Conference Series: Earth and Environmental Science*, 2020, no. 543(1), pp. 012033. **DOI:** 10.1088/1755-1315/543/1/012033

Development and Testing of a Methodology for Assessing of the Correlation Velocity Measurements' Accuracy for the Hydrodynamic Investigations of the Turbulent Coolant Flow in Nuclear Reactor Elements

I.A. Konovalov, A.A. Chesnokov, A.A. Barinov, S.M. Dmitriev, A.E. Khrobostov, M.A. Legchanov, S.S. Borodin, M.A. Makarov

*Nizhny Novgorod State Technical Univercity n.a. R.E. Alekseev,
Minin str., 24, Nizhny Novgorod 603950, Russia*

Received 27.01.2021
Accepted for publication 01.03.2021

Abstract

The correlation method of the coolant flow measuring is widely used in research practice including for studying of turbulent coolant flows in scale models of elements of nuclear power plants. The aim of this work was to develop a technique for assessing the effect of noise recorded by a measuring system on the flow rate readings obtained using the correlation method.

A technique to assess the effect of noise as well as the relative position and acquisition period of sensors is presented. An insignificant concentration of a salt solution ($NaCl$ or Na_2SO_4) is used as a passive impurity which creates a conductivity gradient of the medium recorded by a conductometric system. Turbulent pulsations at the interface between two concurrent isokinetic flows in a channel with a square cross section are used as the signal source for the correlational algorithm.

Paper presents the values of the turbulence′s transport time between spatial conductometers, the results of estimating the spectral power density and band of the recorded signal and also the signal-to-noise ratios of the measuring system obtained on their basis which are subsequently used to estimate the confidence interval of the transport time.

As a result of measurements the relationship between the confidence interval value and the signal length were obtained. The measurements which were carried out at different relative positions of conductometers make it possible to make a conclusion about an increase in the spectral width of the signal and, as a consequence, a decrease in the length of the confidence interval with increasing of distance between sensors.

The presented work is an approbation of this approach for its application as part of an experimental model of a nuclear reactor in order to determine per-channel flow rates in the channels of the core simulator using mesh conductometric sensors taking into account the effect of noise.

Keywords: spatial conductometry, wire mesh sensor, modeling of processes in the elements of nuclear power units.

DOI: 10.21122/2220-9506-2021-12-1-67-74

Адрес для переписки:
Коновалов И.А.
Нижегородский государственный технический университет,
ул. Минина, 24, г. Нижний Новгород 603950, Россия
e-mail: iliakonowaloff@yandex.ru

Address for correspondence:
Konovalov I.A.
Nizhny Novgorod State Technical Univercity,
Minin str., 24, Nizhny Novgorod 603950, Russia
e-mail: iliakonowaloff@yandex.ru

Для цитирования:
I.A. Konovalov, A.A. Chesnokov, A.A. Barinov, S.M. Dmitriev, A.E. Khrobostov, M.A. Legchanov, S.S. Borodin, M.A. Makarov.
Development and Testing of a Methodology for Assessing of the Correlation Velocity Measurements' Accuracy for the Hydrodynamic Investigations of the Turbulent Coolant Flow in Nuclear Reactor Elements.
Приборы и методы измерений.
2021. – Т. 12, № 1. – С. 67–74.
DOI: 10.21122/2220-9506-2021-12-1-67-74

For citation:
I.A. Konovalov, A.A. Chesnokov, A.A. Barinov, S.M. Dmitriev, A.E. Khrobostov, M.A. Legchanov, S.S. Borodin, M.A. Makarov.
Development and Testing of a Methodology for Assessing of the Correlation Velocity Measurements' Accuracy for the Hydrodynamic Investigations of the Turbulent Coolant Flow in Nuclear Reactor Elements.
Devices and Methods of Measurements.
2021, vol. 12, no. 1, pp. 67–74.
DOI: 10.21122/2220-9506-2021-12-1-67-74

Devices and Methods of Measurements
2021, vol. 12, no. 1, pp. 67–74
I.A. Konovalov et al.

Разработка и апробация методики оценки точности корреляционного определения скорости потока теплоносителя при исследованиях гидродинамики турбулентных потоков в элементах ядерных реакторов

И.А. Коновалов, А.А. Чесноков, А.А. Баринов, С.М. Дмитриев, А.Е. Хробостов, М.А. Легчанов, С.С. Бородин, М.А. Макаров

Нижегородский государственный технический университет имени Р.Е. Алексеева, ул. Минина, 24, г. Нижний Новгород 603950, Россия

Поступила 27.01.2021
Принята к печати 01.03.2021

Корреляционный метод измерения расхода теплоносителя находит широкое применение в исследовательской практике, в том числе для изучения турбулентных потоков теплоносителя в масштабных моделях элементов ядерных энергетических установок. Целью данной работы являлась отработка методики оценки влияния шума, регистрируемого измерительной системой, на показания скорости потока, полученные с применением корреляционного метода.

Представлена методика оценки влияния шума, а также взаимного расположения и периода опроса чувствительных элементов на основе кондуктометрической измерительной системы: пространственных кондуктометров сетчатой конструкции. Незначительная концентрация раствора соли (NaCl или Na_2SO_4) используется в качестве пассивной примеси, создающей градиент проводимости среды, регистрируемый кондуктометрической системой. В качестве переносимых возмущений в работе используются турбулентные пульсации на границе раздела двух спутных струй с одинаковыми скоростями в канале квадратного сечения.

Представлены значения времени транспорта турбулентности между пространственными кондуктометрами, результаты оценки спектральной плотности мощности и ширины регистрируемого сигнала, а также полученные на их основе отношения сигнал-шум измерительной системы, в дальнейшем использованные для оценки доверительного интервала времени транспорта.

В результате измерений получены зависимости величины доверительного интервала от времени регистрации показаний пространственных кондуктометров. Измерения, проведённые при различном взаимном расположении кондуктометров, позволяют сделать обобщающий вывод о росте спектральной ширины сигнала и, как следствие этого, уменьшение длины доверительного интервала с увеличением расстояния между датчиками.

Представленная работа является апробацией данного подхода для его применения в составе экспериментальной модели ядерного реактора с целью определения поканальных расходов в каналах имитатора активной зоны при помощи сетчатых кондуктометрических датчиков с учётом влияния шума, регистрируемого измерительной системой.

Ключевые слова: пространственная кондуктометрия, сетчатый датчик, кондуктометрический датчик, моделирование процессов в ЯЭУ.

DOI: 10.21122/2220-9506-2021-12-1-67-74

Адрес для переписки:
Коновалов И.А.
Нижегородский государственный технический университет,
ул. Минина, 24, г. Нижний Новгород 603950, Россия
e-mail: iliakonowaloff@yandex.ru

Address for correspondence:
Konovalov I.A.
Nizhny Novgorod State Technical Univercity,
Minin str., 24, Nizhny Novgorod 603950, Russia
e-mail: iliakonowaloff@yandex.ru

Для цитирования:
I.A. Konovalov, A.A. Chesnokov, A.A. Barinov, S.M. Dmitriev, A.E. Khrobostov, M.A. Legchanov, S.S. Borodin, M.A. Makarov.
Development and Testing of a Methodology for Assessing of the Correlation Velocity Measurements' Accuracy for the Hydrodynamic Investigations of the Turbulent Coolant Flow in Nuclear Reactor Elements.
Приборы и методы измерений.
2021. – Т. 12, № 1. – С. 67–74.
DOI: 10.21122/2220-9506-2021-12-1-67-74

For citation:
I.A. Konovalov, A.A. Chesnokov, A.A. Barinov, S.M. Dmitriev, A.E. Khrobostov, M.A. Legchanov, S.S. Borodin, M.A. Makarov.
Development and Testing of a Methodology for Assessing of the Correlation Velocity Measurements' Accuracy for the Hydrodynamic Investigations of the Turbulent Coolant Flow in Nuclear Reactor Elements.
Devices and Methods of Measurements.
2021, vol. 12, no. 1, pp. 67–74.
DOI: 10.21122/2220-9506-2021-12-1-67-74

Devices and Methods of Measurements
2021, vol. 12, no. 1, pp. 67–74
I.A. Konovalov et al.

Introduction

Nowadays special attention is paid to experimental studies of the hydrodynamic characteristics of the coolant flow in scale models of elements of nuclear power plants which are aimed at validating the computational models necessary to substantiate the reliability and safety of structures [1]. The question about the control of the indicators of the coolant flow rate in the elements under study when carrying out such experiments is often arised.

At the moment the correlation method for measuring the flow rate of a coolant is widely known the main requirement of which is the presence of a certain passive scalar flow function convectively transferred along with the flowing medium. It allows one to implement correlation measurements using various methods for measuring the properties of the flow: temperature, content of radioactive isotopes, optically distinguishable impurities, etc. [2–3]. This approach assumes determination of the transit time of the disturbance of the measured quantity (the so-called turbulence transport time) between the sensitive elements of the system which are located at some distance from each other.

The paper [4] presents a method of using a conductometric measuring system for the correlation determination of the flow velocity [5–7] based on the determination of the cross-correlation function maximum as the time of turbulence transport between sensors. To improve the measurement accuracy and reduce the influence of the most intense pickups a digital low-pass filter was used in the specified work [4] when processing the measuring signal [8]. However the question about assessing the contribution of the "noise" passed by the low-pass filter to the relative error in determining the position of the cross-correlation function maximum remains open.

This problem directly affects the measuring accuracy of the coolant flow rate in the elements of nuclear power plants therefore in the case of research facilities it can have a significant impact on results of experimental data processing which are used to substantiate the reliability and safety of the structures under study.

In correlation measurements of the flow velocity the duration of the realization is very important according to which the cross-correlation function is calculated. Therefore the question about the methodology for choosing of the optimal sampling rate of measuring elements (in this case conductometric sensors) arises, which would satisfy the conditions for maintaining an acceptable measurement accuracy at the maximum sampling rate of readings.

From the above it follows that the purpose of this work was to determine the confidence interval when finding the turbulence transport time between the measuring elements and to estimate the dependence of the confidence interval length on the recording period of the flow rate readings.

Test facility

The general layout of the stand (Figure 1) assumes the organization of an experimental regime with isothermal mixing in an open circulation loop (for studies flows with different concentrations of impurities were used) and non-isothermal mixing when flows with different temperatures were used.

The equipment of the stand makes it possible to create both laminar and turbulent flow regimes (with Re up to $20 \cdot 10^3$) at different temperatures, flow rates and tracer concentrations in the coolant flow. The main parameters of the test facility are shown in Table 1.

Table 1

Parameters of the test facility

Parameter	Value
Total heaters power, kW	12
Flow through test model, m^3/hr	to 2.1
Temperature of the mixing flows, °C	10–60

Experiments

Measurements were carried out in a test model with a square cross section of 50×50 mm^2, the general view of which is shown in Figure 2. The model repeats in general details of the test model geometry from [9]. Wire mesh sensors (WMS) were installed in a zone of intense mixing at different distances from each other.

Measurements were carried out in the flow range up to 2.1 m^3/h (Re = $20 \cdot 10^3$).

The main parameters of the experimental modes are presented in Table 2.

For each mode "non-contrast measurements" were made in which there was no impurity tracer in the mixed flows creating a gradient of the medium conductivity. In this case reading signals′ fluctuations of the mesh sensors were determined only by the noises recorded by the measuring system. These measurements were used to estimate the noise level and to determine the signal-to-noise ratio.

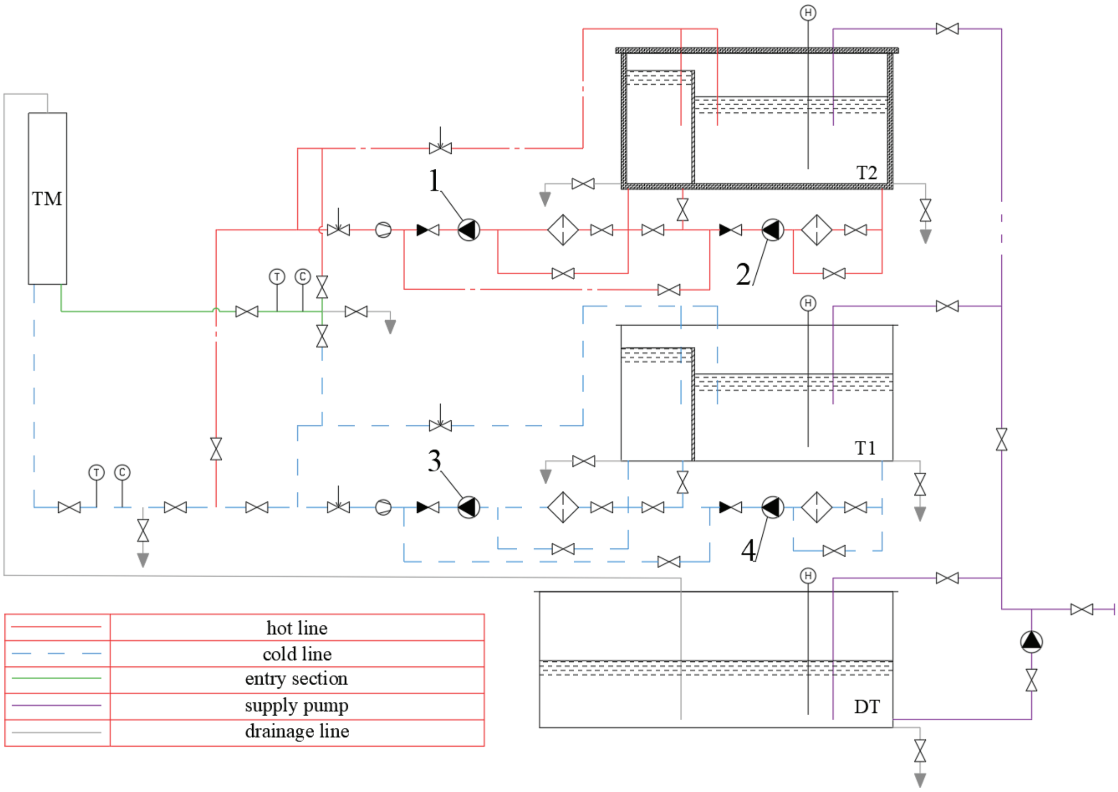

Figure 1 – Hydraulic diagram of the test facility: 1 – hot line circulation pump; 2 – hot line supply pump; 3 – cold line circulation pump; 4 – cold line supply pump; T1 – cold tank; T2 – hot tank; DT – drainage tank; TM – test model

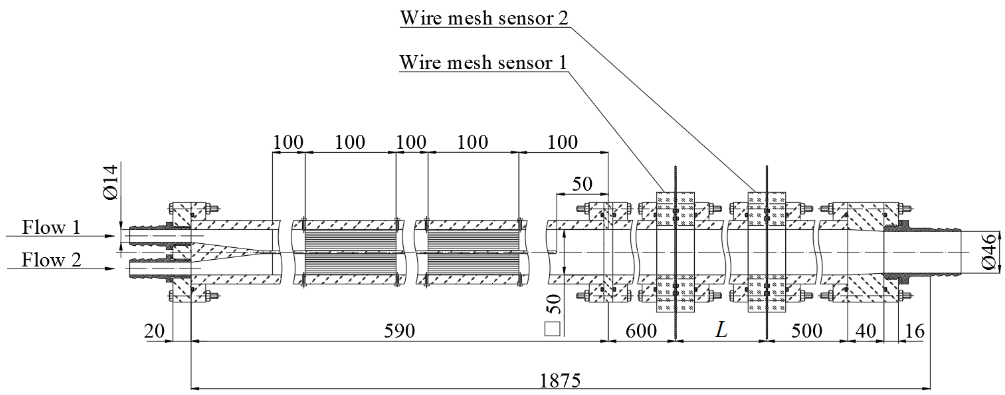

Figure 2 – Test model

Table 2

Main parameters of the experimental modes

$Re \cdot 10^3$	Temperature of the mixing flows, °C	Conductivity of salty flow, μS/cm	Conductivity of bulk flow, μS/cm	Distance between wire mesh sensors, mm	Duration of realization, s
20	45.0	1302.0	1030.0	640	120
	44.9	1335.0	1045.0	440	120
	44.9	1311.0	1029.5	240	120
	44.7	1318.0	1029.0	40	120

Measurements of the coolant velocities in the cells of the wire mesh sensors were carried out in accordance with the procedure described in [4]. The accepted cell numbering is shown on Figure 3.

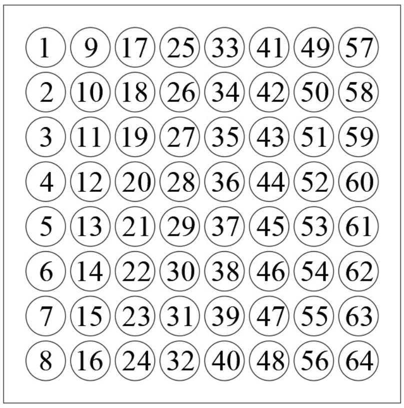

Figure 3 – Cells layout of wire mesh sensors

The experimental data are instantaneous and averaged conductivity fields, mode parameters, and averaged values of flow velocities in the model obtained by the correlation method.

Method of experimental data processing

In accordance with the method described in [10] estimation of the confidence interval for the turbulence transport time estimate between sensors is reduced to the determination of the normalized root-mean-square error of the cross-correlation function which for the frequency-limited "white noise" has the form [11]:

$$\varepsilon^2[R_{xy}(\tau)] = \frac{1}{2B \cdot T}(2 + (M/S) + (N/S) + (M/S)(N/S)), \quad (1)$$

where: $R_{xy}(\tau)$ – the value of the mutual correlation function at the moment of time τ; T – duration of realization, s; B – spectral width of white noise, Hz; M/S, N/S – the signal-to-noise ratio of the first and second WMS, respectively.

Assuming that the measurement signal $S(t)$ can be considered as frequency-limited "white noise" from expression (1) we obtain:

$$\varepsilon^2[R_{xy}(\tau)] = \frac{1}{2B \cdot T}(2 + (S/M) + (S/N) + (S/M)(S/N)). \quad (2)$$

In this case, the band of the measurement signal B can be defined as the frequency interval containing 95 % of the energy of the signal under investigation. The definition of B was made based on the analysis of the energy spectrum of the conductivity pulsations in the mixing zone obtained by the method of the modified Welch's periodogram using the expression:

$$0.95 \cdot W = \int_0^B P(f) \cdot df, \quad (3)$$

where: W – the power carried by the signal in the entire considered frequency range, W; $P(f)$ – the function of the spectral power density, W·s; f – frequency of pulsations of electrical conductivity in the measuring area, Hz.

The signal-to-noise ratio (Figure 4) was estimated individually for each sensor as the average quotient of spectral densities of the noise and signal in the band range B:

$$S/M = \frac{1}{B} \cdot \int_0^B \frac{S(f)}{M(f)} \cdot df, \quad (4)$$

where: $S(f)$, $M(f)$ – the functions of the spectral power density for contrast (signal) and non-contrast (noise) mixing, respectively, W·s; f – frequency of pulsations of specific electrical conductivity in the measuring area, Hz.

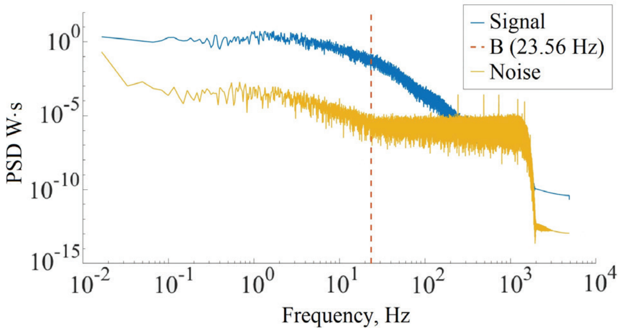

Figure 4 – Summary chart of power spectrum density (PSD) during "contrast mixing" (signal) and "non-contrast" mixing (noise) in cell 28 for experiment with Re = $20 \cdot 10^3$ (distance between WMS 240 mm)

Finally, the 95 % confidence interval in determining of the position of the maximum of the cross-correlation function was determined based on the expression:

$$[-2 \cdot \sigma_i(\tau_{\max}) \le \tau_{\max} \le 2 \cdot \sigma_i(\tau_{\max})], \quad (5)$$

where: $\tau_{\max}$ – the time shift corresponding to the position of the maximum of the mutual correlation function (turbulence transport time), s; $\sigma_i(\tau_{\max})$ – the variance of the normalized root-mean-square error, defined as:

$$\sigma_i(\tau_{\max}) \approx (\varepsilon^2[R_{xy}(\tau_{\max})])^{1/4}. \quad (6)$$

Analysis of results

As a result of processing the experimental data in accordance with the method described above, the cross-correlation functions of the realizations of the first and second WMS were obtained, the averaged values of the flow rates in the measuring cells of the sensors were obtained, and the confidence interval was evaluated when determining the position of the maximum of the cross-correlation function. Figure 5 shows the graphs of the cross-correlation function with the designated confidence intervals for the mode $\mathrm{Re} = 20{\cdot}10^3$ at various distances between the sensors.

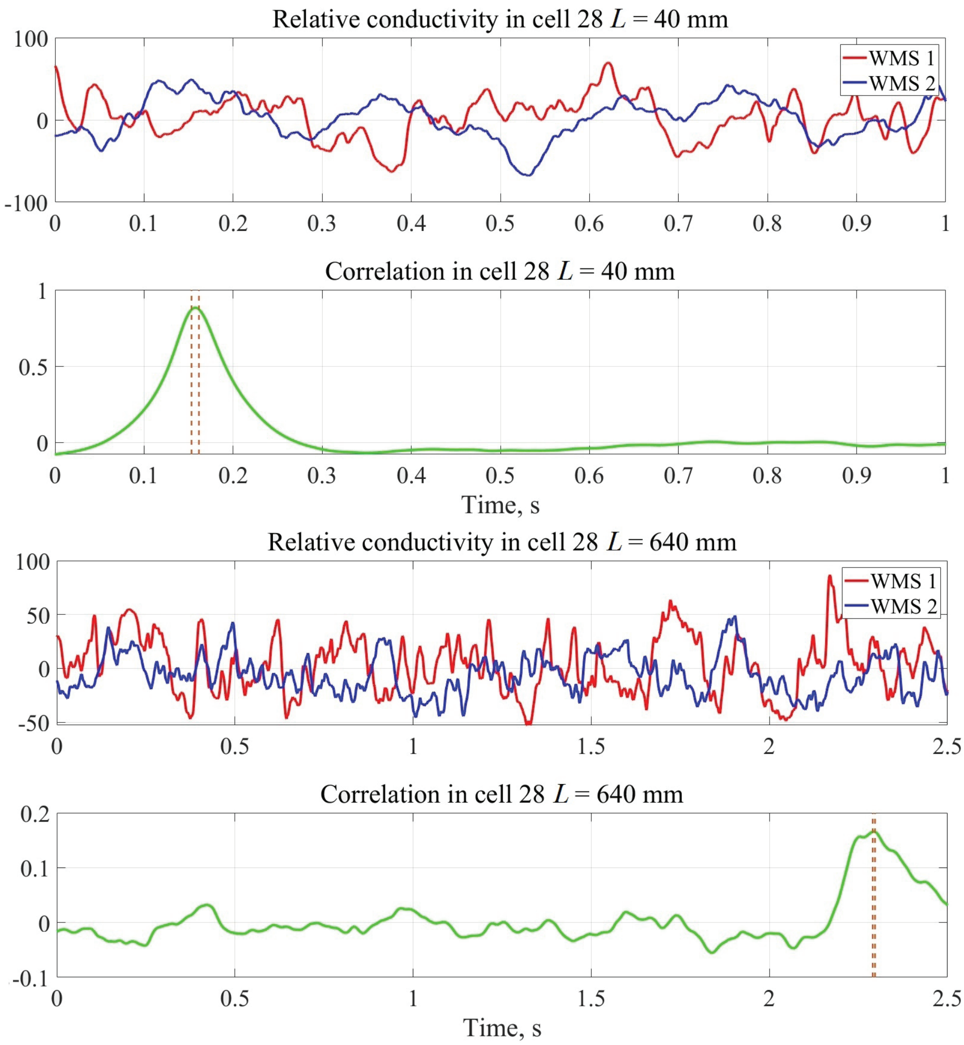

Figure 5 – Normalized electrical conductivities and cross-correlation functions in test with $\mathrm{Re} = 20{\cdot}10^3$ with different distances between wire mesh sensors for cell 28

Graphs show that with an increase of the distance between the measuring planes of the wire mesh sensor from 40 mm to 640 mm (approximately equal to the scale of the main energy-carrying vortices) a significant decrease in the level of signal correlation is observed.

Numerical estimates of the deviations in determining the position of the function maximum were obtained, as well as the variance of the normalized mean square error of the maximum position. Also average values of the measuring signal band and data on the average flow rate were obtained. The results are recorded in Table 3.

Studies of dependence of the confidence interval length on the duration of realization were carried out on the basis of dividing the initial signal realization (duration 120 s) into windows with durations ranging from 1 to 120 s (120 and 1 window, respectively). Further, in accordance with the technique (1)–(6), the confidence interval of the cross-correlation function maximum position was estimated for each window.

The results of the experimental data processing for the mode with Re = $20 \cdot 10^3$ at a distance between the WMS of 40 mm are shown in Figure 6 as the dependence of the absolute interval length on the interrogation period of the WMS.

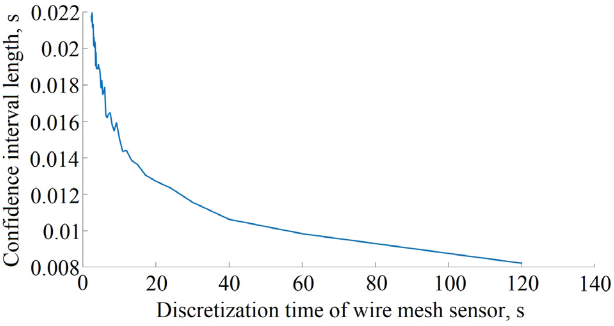

Figure 6 – Dependence of confidence interval on discretization time (time window) of wire mesh sensors

The graph shows the exponential dependence of the confidence interval length and consequently, the measurement accuracy on the duration of the realization (time window).

The dispersion of τ_{max} values was taken as a criterion for stability of determining of the cross-correlation function maximum position for each window within one realization (Figure 7).

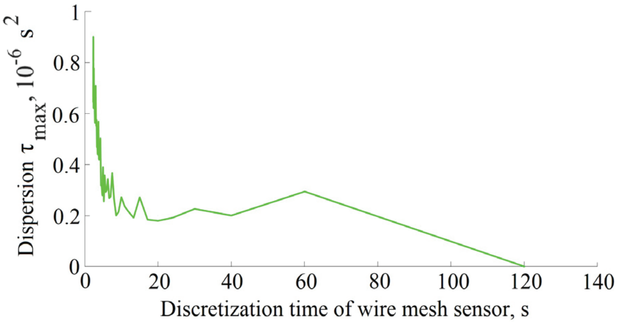

Figure 7 – Dispersions of turbulence transport time per discretization time (time window) of wire mesh sensors

The graph shows that the variance values do not exceed 10^{-6} s^2. This indicates that the readings of the first and second wire mesh sensors are correlated along all the considered window lengths.

Conclusion

The experimental data analysis made it possible to estimate the confidence interval of the cross-correlation function maximum position for the correlation method of measuring of the flow rate of the coolant turbulence transport time based on the correlation methodlogy. The obtained value of the relative deviation in determining of the turbulence transport time between the measuring planes of the mesh sensors indicates a low contribution of the "noise" recorded by the conductometric measuring system to the signal under study.

A decrease in the distance between the sensors allows one to obtain a higher value of the correlation coefficient which, in turn, can affect the accuracy of determining of the position of the cross-correlation function maximum when measuring the flow velocity with a low degree of turbulence. However, this entails an increase in the relative error in the study of high-speed flows due to decrease in the total time of turbulence transport between mesh conductometric sensors.

The results of the work can be used to determine the optimal relative position and interrogation period of sensors designed to register changes in time of a certain scalar quantity (temperature, concentration, radioactivity, etc.) when using sensors to determine the flow rate by the correlation method of measuring the speed for correlation flow rate methodology.

Acknowledgments

Developing and approbation of method of correlation velocity measurements for the turbulent flows with conductometric measurement system was funded by the grant of Russian Science Foundation (project No. 18-19-00473).

References

1. Rohde U., Kliem S., Hemstrom B., Toppila T., Bezrukov Y. The European project FLOMIX-R: Description of the slug mixing and buoyancy related experiments at the different test facilities (Final report on WP 2). Report FZR–430, 2005, pp. 5–8.

2. Kapulla R., Dyck C., Witte M., Fokken J., Leder F. Optical flow and cross correlation techniques for velocity field calculation. *Fachtagung "Lasermethoden in der Strömungsmesstechnik"*, 8–10 September 2009, Erlangen.

3. Borisov V.F., Strukov M.A. *Sposob izmereniya rashoda teplonositelya pervogo kontura yadernogo reaktora* [Method for measuring the flow rate of the primary loop of a nuclear reactor]. Patent RF, no. 2457558, 2012.

4. Konovalov I.A., Khrobostov A.E., Legchanov M.A., Solncev D.N., Barinov A.A., Ryazanov A.V., Chesnokov A.A., Makarov M.A. Application of the Correlation Velocity Measurements for Hydrodynamic

Investigations of Turbulent Coolant Flow in Nuclear Reactor Elements. *Devices and Methods of Measurements*, 2020, vol. 11, no. 3, pp. 196–203.
DOI: 10.21122/2220-9506-2020-11-3-196-203

5. Prasser H.M., Kleim S. Coolant mixing experiments in the upper plenum of the ROCOM test facility. *Nuclear Engineering and Design*, 2014, no. 276, pp. 30–42. **DOI:** 10.1016/j.nucengdes.2016.10.038

6. Dave A., Manera A., Beyer M., Lucas D., Prasser H.M. Uncertainty analysis of an interfacial area reconstruction algorithm and its application to two group interfacial area transport equation validation. *Nuclear Engineering and Design*, 2016, no. 310, pp. 30–42.
DOI: 10.1016/j.nucengdes.2014.05.016

7. Dmitriev S.M., Khrobostov A.E., Barinov A.A., Glavnii V.G. *Razrabotka I adaptatsiya vihrerazreshayshei izmeritelnoi systemi* [Development and Adaptation of Vortex Realizable Measurement System for Benchmark Test with Large Scale Model of Nuclear Reactor]. *Devices and Methods of Measurements*, 2017, vol. 8, no. 3, pp. 203–213 (in Russian).
DOI: 10.21122/2220-9506-2017-8-3-203-213

8. Sorokin G.A. *Filtri nizhnih chastot* [Low-pass filters]. *Vestnik Uzhno-Uralskogo gosudarstvennogo universiteta. Seriya: Computernie tehnologii* [Bulletin of the South Ural State University. Series: Computer technology, control, radio electronics], 2015, vol. 1, pp. 100–107 (in Russian).

9. Kokken J., Krohn B., Kapulla R., Niceno B., Prasser H.M., Badillo A. NEA Benchmark Exercise: Computational Fluid Dynamic Prediction and Uncertainty Quantification of a GEMIX Mixing Layer Test. *Nuclear energy agency committee on the safety of nuclear installations*, 2019, pp. 21–25.

10. Bendat J., Piersol A. Random Data: Analysis and Measurements Procedures. *Fourth Edition. John Willey* & *Sons*, 2012, pp. 272–274.

11. Bendat J., Piersol A. Engineering Applications of Correlation and Spectral Analysis. *Second Edition. John Willey* & *Sons*, 2013, pp. 274–276.

Variables Selection in the Ultraviolet, Visible and Near Infrared Range for Calibration of a Mixture of Vegetable Oils by Absorbance Spectra

M.A. Khodasevich, D.A. Borisevich

B.I. Stepanov Institute of Physics of the National Academy of Sciences of Belarus, Nezavisimosty Ave., 68, Minsk 220072, Belarus

Received 29.01.2021
Accepted for publication 01.03.2021

Abstract

The aim of the work was a multivariate calibration of the concentration of unrefined sunflower oil, considered as adulteration, in a mixture with flaxseed oil. The relevance of the study is due to the need to develop a simple and effective method for detecting the falsification of flaxseed oil which is superior in the content of essential polyunsaturated fatty acids to olive oil. A few works only are devoted to identifying adulteration of flaxseed oil, unlike olive oil.

Multivariate calibration carried out using a model based on the principal component analysis, cluster analysis and projection to latent structures of absorbance spectra in UV, visible and near IR ranges. Calibration uses three methods for spectral variables selection: the successive projections algorithm, the method of searching combination moving window, and method for ranking variables by correlation coefficient.

The application of the successive projections algorithm, ranking variables by correlation coefficient and searching combination moving window makes it possible to reduce the value of the root mean square error of prediction from 0.63 % for wideband projection to latent structures to 0.46 %, 0.50 %, and 0.03 %, respectively.

The developed method of multivariate calibration by projection to latent structures of absorbance spectra in UV, visible and near IR ranges using the spectral variables selection by searching combination moving window is a simple and effective method of detecting adulteration of flaxseed oil.

Keywords: spectral analysis, principal component analysis, projection to latent structures, spectral variables selection.

DOI: 10.21122/2220-9506-2021-12-1-75-81

Адрес для переписки:
Ходасевич М.А.
Институт физики имени Б.И. Степанова НАН Беларуси, пр-т Независимости, 68, г. Минск 220072, Беларусь
e-mail: m.khodasevich@ifanbel.bas-net.by

Address for correspondence:
Khodasevich M.A.
B.I. Stepanov Institute of Physics of the National Academy of Sciences of Belarus,
Nezavisimosty Ave., 68, Minsk 220072, Belarus
e-mail: m.khodasevich@ifanbel.bas-net.by

Для цитирования:
M.A. Khodasevich, D.A. Borisevich.
Variables Selection in the Ultraviolet, Visible and Near Infrared Range for Calibration of a Mixture of Vegetable Oils by Absorbance Spectra.
Приборы и методы измерений.
2021. – Т. 12, № 1. – С. 75–81.
DOI: 10.21122/2220-9506-2021-12-1-75-81

For citation:
M.A. Khodasevich, D.A. Borisevich.
Variables Selection in the Ultraviolet, Visible and Near Infrared Range for Calibration of a Mixture of Vegetable Oils by Absorbance Spectra.
Devices and Methods of Measurements.
2021, vol. 12, no. 1, pp. 75–81.
DOI: 10.21122/2220-9506-2021-12-1-75-81

Devices and Methods of Measurements
2021, vol. 12, no. 1, pp. 75–81
M.A. Khodasevich, D.A. Borisevich

Выбор переменных в ультрафиолетовом, видимом и ближнем инфракрасном диапазонах для калибровки смеси растительных масел по спектрам оптической плотности

М.А. Ходасевич, Д.А. Борисевич

Институт физики имени Б.И. Степанова Национальной академии наук Беларуси, пр-т Независимости, 68, г. Минск 220072, Беларусь

Поступила 29.01.2020
Принята к печати 01.03.2021

Целью работы являлась многопараметрическая калибровка концентрации нерафинированного подсолнечного масла, рассматриваемого в качестве фальсификата льняного масла. Актуальность исследования обусловлена необходимостью разработки простого и эффективного метода обнаружения фальсификации льняного масла, превосходящего по содержанию незаменимых полиненасыщенных жирных кислот оливковое масло, выявлению подделок которого в отличие от льняного посвящено большое количество работ.

Многопараметрическая калибровка проводилась с помощью модели, основанной на методе главных компонент, кластерном анализе и проекции на латентные структуры спектров оптической плотности в УФ-, видимом и ближнем ИК диапазонах с применением трех методов выбора спектральных переменных: метода последовательного проецирования, метода поиска комбинации сдвигающихся окон и метода ранжирования переменных по коэффициенту корреляции.

Показано, что применение методов последовательного проецирования, ранжирования переменных по коэффициенту корреляции и поиска комбинации сдвигающихся спектральных окон позволяет уменьшить величину среднеквадратичного отклонения калибровки с 0,63 % для широкополосной проекции на латентные структуры до 0,46 %, 0,50 % и 0,03 %, соответственно.

Разработанный метод многопараметрической калибровки с помощью проекции на латентные структуры спектров оптической плотности в УФ-, видимом и ближнем ИК диапазонах с применением выбора спектральных переменных путём поиска комбинации сдвигающихся окон является простым и эффективным средством обнаружения фальсификации льняного масла.

Ключевые слова: спектральный анализ, метод главных компонент, проекция на латентные структуры, выбор спектральных переменных.

DOI: 10.21122/2220-9506-2021-12-1-75-81

Адрес для переписки:
Ходасевич М.А.
Институт физики имени Б.И. Степанова НАН Беларуси, пр-т Независимости, 68, г. Минск 220072, Беларусь
e-mail: m.khodasevich@ifanbel.bas-net.by

Address for correspondence:
Khodasevich M.A.
B.I. Stepanov Institute of Physics of the National Academy of Sciences of Belarus,
Nezavisimosty Ave., 68, Minsk 220072, Belarus
e-mail: m.khodasevich@ifanbel.bas-net.by

Для цитирования:
M.A. Khodasevich, D.A. Borisevich.
Variables Selection in the Ultraviolet, Visible and Near Infrared Range for Calibration of a Mixture of Vegetable Oils by Absorbance Spectra.
Приборы и методы измерений.
2021. – Т. 12, № 1. – С. 75–81.
DOI: 10.21122/2220-9506-2021-12-1-75-81

For citation:
M.A. Khodasevich, D.A. Borisevich.
Variables Selection in the Ultraviolet, Visible and Near Infrared Range for Calibration of a Mixture of Vegetable Oils by Absorbance Spectra.
Devices and Methods of Measurements.
2021, vol. 12, no. 1, pp. 75–81.
DOI: 10.21122/2220-9506-2021-12-1-75-81

Devices and Methods of Measurements
2021, vol. 12, no. 1, pp. 75–81
M.A. Khodasevich, D.A. Borisevich

Introduction

Food adulteration is a serious problem around the world. Products of animal and vegetable origin with a high content of fat are most subject to falsification. Meat, fish, oils, dairy products, etc. account for almost 68 % of adulterated food products [1]. Vegetable oil is one of the most widely demanded foods. Olive oil, which is wrongly considered the most beneficial for human health, is the most often adulterated vegetable oil. A large number of studies are devoted to the detection of falsification of olive oil using optical spectroscopy methods such as fluorescence and UV and visible spectroscopy [2], Raman spectroscopy [3], combination of near and mid IR spectroscopy [4], etc. But olive oil is inferior to flaxseed oil in the content of essential polyunsaturated fatty acids, among which the content of alpha-linolenic (omega-3) acid can reach 64 %. Only a small amount of studies has been focused on detecting flaxseed oil adulteration. For example, Fourier spectroscopy was used to detect the falsification of flaxseed oil with olive oil [5] and mid-IR spectroscopy was used to detect the adulteration of flaxseed oil by soybean and sunflower oils [6].

Earlier [7], we carried out a multivariate calibration of the concentration of unrefined sunflower oil, considered as adulteration, in a mixture with flaxseed oil using a model based on the principal component analysis (PCA) [8], cluster analysis and projection to latent structures (PLS) [9] of absorbance spectra in UV, visible and near IR ranges. To further reduce the root mean square error of prediction ($RMSE_P$), in this work we compared three methods for spectral variables selection: the Successive Projections Algorithm (SPA) [10], the searching combination moving window interval PLS (scmwiPLS) and the method using correlation coefficients ranging [11].

The objects of the study were specially prepared samples of binary mixtures of unrefined sunflower and flaxseed oils with a percentage from 0 to 100 %. Absorbance spectra were measured on a Shimadzu UV-3101PC spectrophotometer with a step of 1 nm in two ranges: from 335 to 690 nm and from 1130 to 2200 nm with a slit width of 1 nm and 3 nm, respectively. The interval 1698–1766 nm, corresponding to the first overtone of the C – H vibrations of the $–CH_2–$ group [12, 13], is very noisy, therefore, it was not taken into account in further consideration.

Spectra processing and multivariate calibration

Before applying the PCA method, it is necessary to form a rectangular matrix of spectra of the studied samples. In this matrix rows are samples, columns are spectral variables. According to the dependence of the total explained variance of the spectral data on the number of principal components, it was determined that 99.7 % of the total variance is described by the first principal component. Using the linear approximation of the scores to the first principal component, samples that deviate significantly from the general dependence are identified as outliers. These samples correspond to 10 %, 25 %, 30 %, 60 %, 65 %, 70 % and 72.5 % concentrations of sunflower oil and were removed from further consideration.

To create the PLS model, the remaining samples were divided into training sampling and test one by the hierarchical cluster analysis in the Euclidean space of the first principal component of absorbance spectra. For a planned experiment, this method gives smaller values of $RMSE_P$ [14] compared to uniform partitioning by a calibrated parameter or the frequently used Kennard–Stone algorithm [15]. The values of scores to the first principal component were aggregated to 6 clusters. 6 spectra with scores that were closest to the centers of the clusters were selected to the test sampling. The remaining 18 samples constituted the training sampling. Thus, 75 % of the samples are used to build the model and 25 % to validate it.

After the stage of dividing the samples into training and test samplings, one can proceed to calibrating the content of sunflower oil in a mixture with flaxseed oil using a wideband multivariate PLS with all 1345 spectral variables. Figure 1 shows that the optimal number of latent structures is 6, since $RMSE_P$ in this case is minimal and equal to 0.63 %.

Due to the collinearity of spectral data and possibility of low signal-to-noise ratio for individual spectral variables and even in rather wide spectral intervals, the use of the entire measured spectral range may not be optimal for calibration accuracy. To improve the quality of the multivariate model, it is advisable to reduce the number of variables taken into account in the simulation. The spectral variables selection is an important step in improving the quality of calibration and stability of the model with possible verification using additional samples.

Devices and Methods of Measurements
2021, vol. 12, no. 1, pp. 75–81
M.A. Khodasevich, D.A. Borisevich

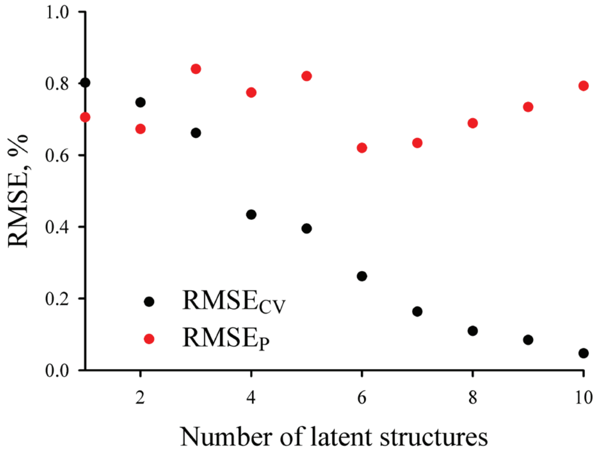

Figure 1 – Dependences of the RMSE$_{CV}$ (root mean square error of cross-validation) for the training sampling and RMSE$_P$ for the test sampling for the wideband PLS

We consider three following methods for spectral variables selection. The first method is based on ranking the variables using the correlation coefficients between spectral counts and the calibrated parameter found for wideband PLS with six latent structures. In this case, the spectral variables are excluded from the multivariate model one by one in accordance with the decreasing correlation coefficient. RMSE$_P$ is determined at each step. The minimum value of RMSE$_P$ specifies an optimum set of spectral variables that corresponds to the best model for the applied method. Figure 2 shows that this minimum value of RMSE$_P$ = 0.50 % is achieved when removing 1106 spectral variables for 239, taken into account in the multivariate model.

The second considered method is SPA. At the first stage of algorithm fulfillment, for the 1345 variables available in our case, a set of 1345 ordered sequences of spectral variables is constructed, the first elements of which are different. In the multidimensional space of spectral variables the remaining 1344 variables are projected onto the space orthogonal to the selected first variable. The largest projection value determines the second in order variable. Similarly, all the following spectral variables in considered sequence are ranked by projections on the subspace orthogonal to the subspace of the variables already selected. For each element of the generated set of ordered sequences of spectral variables, PLS is constructed starting with the first ten spectral variables for certainty, and ending with a set of all 1345 variables. For every number of spectral variables taken into account in the multivariate models for variables sequence considered, the optimal number of latent structures was selected based on the minimum value of RMSE$_P$. The global minimum of RMSE$_P$ was found from $1795575 = 1345 \times 1335$ values. Here 1345 is the number of elements in the set of ordered sequences of spectral variables and 1335 is the number of PLS models with an increase in the number of spectral variables from 10 to 1345. Based on the global minimum of RMSE$_P$ of the sunflower oil concentration in a binary mixture of vegetable oils, the required sequence of spectral variables was determined, which ensures maximum calibration accuracy for variables selection method applied. In our case, the required sequence of spectral variables began with wavelength of 1781 nm and consisted of only 14 variables. It is rather small number of selected variables and its further reduction is impractical. Often the final stage of SPA execution aims to reduce number of selected variables, taking into account the correlation coefficient of the spectral variables and the calibrated parameter.

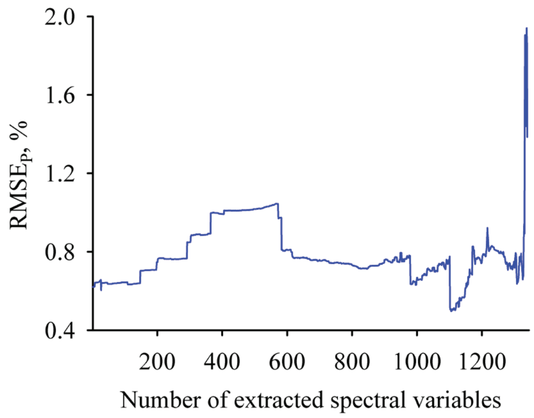

Figure 2 – Dependence of the RMSE$_P$ on the number of extracted spectral variables in ranking method using correlation coefficients between spectral counts and calibrated parameter

The third used method is searching combination moving window interval PLS (scmwiPLS) [14]. In contrast to the two previous methods, the described method operates not with individual spectral variables, but with a continuous interval or, as it is often called in multivariate analysis, a window [16]. The algorithm for applying this method is as follows. First, you need to select the width of the windows that shift along the spectrum. In the scmwiPLS modification we use, the number of spectral variables

Devices and Methods of Measurements
2021, vol. 12, no. 1, pp. 75–81
M.A. Khodasevich, D.A. Borisevich

in window exceeds the number of latent structures by one in order for PLS to be able to reduce the dimension of the variable space by at least one. Note that, unlike SPA, the number of latent structures (6 in our case) does not change during the whole algorithm. Second, the spectral position of the first window should be determined. It shifts across the entire spectral range and is fixed in the place where $RMSE_P$ of PLS model based on selected spectral variables is minimal. Third, it is necessary to determine the position of the added windows until they fill the entire measurement range. Subsequent windows are similarly shifted within the entire spectral range of measurements and are alternately combined with the selected ones, provided that the minimum value of $RMSE_P$ is reached for the combined set of windows. And finally the search for the minimum value of $RMSE_P$, depending on the number of windows, determines the desired set of spectral variables for scmwiPLS. Figure 3 shows the dependence of the $RMSE_P$ on the number of combined windows in scmwiPLS. The minimum root mean square error of prediction equals 0.03 % and corresponds to the combination of 38 windows with 7 variables or 266 spectral variables.

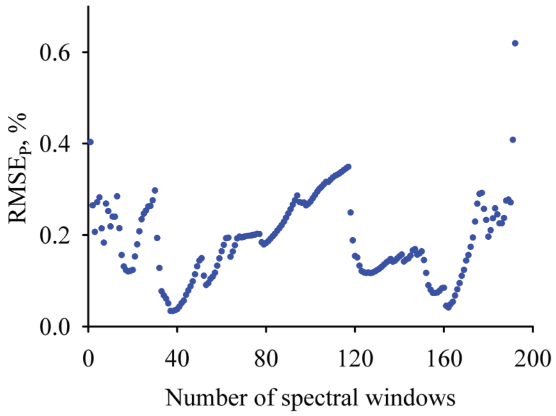

Figure 3 – Dependence of the $RMSE_P$ on the number of combined windows in scmwiPLS

Figure 4 shows dependence of concentration of sunflower oil predicted by the scmwiPLS on its measured concentration in a binary mixture of sunflower and flaxseed oils for training and test samplings. It indicates the high quality of the multivariate model with spectral variables selection, which can be characterized by the value of the residual predictive deviation RPD. RPD is equal to the ratio of the standard deviation of the calibrated parameter and $RMSE_P$. RPD exceeds 1000 for the described scmwiPLS model.

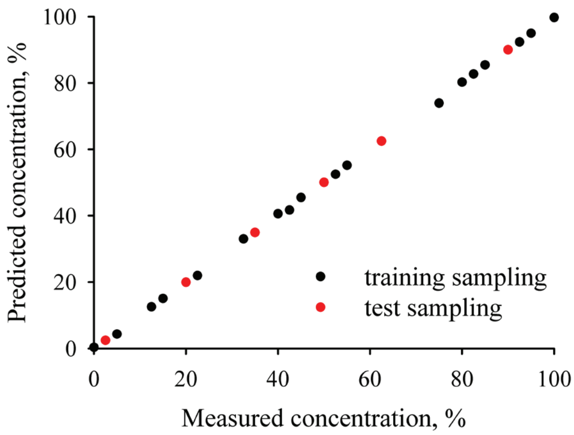

Figure 4 – Concentration of sunflower oil predicted by the scmwiPLS vs measured concentration in a binary mixture of sunflower and flaxseed oils

Figure 5 shows the spectral variables selected using the three investigated methods and the example of the absorbance spectrum of sunflower and flaxseed oils mixture.

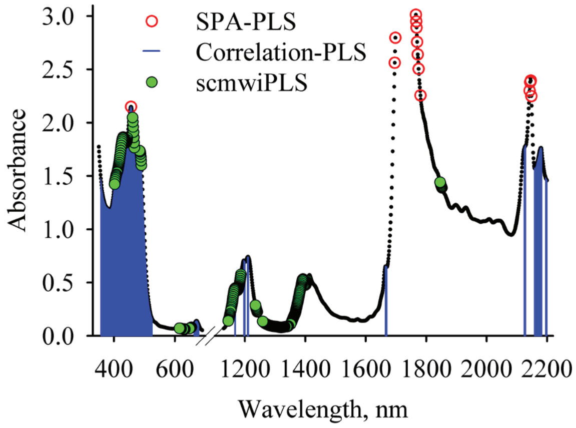

Figure 5 – Absorbance spectra of the mixture of sunflower (12.5 %) and flaxseed (87.5 %) oils and spectral variables selected using the three investigated methods

Spectral variables selection using the ranking of correlation coefficients (239 variables) and the SPA method (14 variables) allows reducing the value of the root mean square error of prediction of sunflower oil concentration from 0.63 % for wideband PLS to 0.50 % and 0.46 %, respectively. These selections are advisable for classical spectroscopy, since the variables selected by both methods are close to the spectral features of the studied objects. The spectral variables selection by scmwiPLS method (266 variables) is less consistent with classical spectroscopy, since a significant part of the selected variables does not describe the characteristic features of the studied spectra, but allows $RMSE_P$ to be reduced by more than an order of magnitude to 0.03 %. Thus, it can be noted that an increase in the calibration accuracy is achieved by using a formal method of variables selection, a feature of which is the use of narrow spectral intervals instead of separate wavelengths.

Conclusion

On the example of the calibration of the concentration of unrefined sunflower oil, considered as a falsified flaxseed oil, it was confirmed that the spectral variables selection is a necessary and important part of multivariate models to improve the accuracy.

It was found that from the considered methods applied to the projection to latent structures of the absorbance spectra for calibrating the concentration of sunflower oil in a mixture with flaxseed oil, a smaller root mean square error of prediction (0.03 %) is achieved for searching combination moving window method in comparison with the successive projection algorithm (0.46 %) and the ranking of spectral variables by the correlation coefficient (0.50 %).

Acknowledgments

This work was supported by the Belarusian Republican Foundation for Fundamental Research grant (project No. F19-060).

References

1. Valdés A., Beltrán A., Mellinas C., Jiménez A., Garrigós M.C. Analytical methods combined with multivariate analysis for authentication of animal and vegetable food products with high fat content. *Trends in Food Science & Technology*, 2018, vol. 77, pp. 120–130.
DOI: 10.1016/j.tifs.2018.05.014

2. Milanez K., Nóbrega T., Nascimento D., Insausti M., Band B., Pontes M. Multivariate modeling for detecting adulteration of extra virgin olive oil with soybean oil using fluorescence and UV–Vis spectroscopies: A preliminary approach. *Food Science and Technology*, 2017, vol. 85, pp. 9–15.
DOI: 10.1016/j.lwt.2017.06.060

3. Lima T., Musso M., Menezes D. Using Raman spectroscopy and an exponential equation approach to detect adulteration of olive oil with rapeseed and corn oil. *Food Chemistry*, 2020, vol. 333, pp. 127454.
DOI: 10.1016/j.foodchem.2020.127454

4. Li Y., Xiong Y., Min S. Data fusion strategy in quantitative analysis of spectroscopy relevant to olive oil adulteration. *Vibrational Spectroscopy*, 2019, vol. 101, pp. 20–27.
DOI: 10.1016/j.vibspec.2018.12.009

5. Elzey B., Pollard D., Fakayode S. Determination of adulterated neem and flaxseed oil compositions by FTIR spectroscopy and multivariate regression analysis. *Food Control*, 2016, vol. 68, pp. 303–309.
DOI: 10.1016/j.foodcont.2016.04.008

6. De Souza L., De Santana F., Gontijo L., Mazivila S., Neto W. Quantification of adulterations in extra virgin flaxseed oil using MIR and PLS. *Food Chemistry*, 2015, vol. 182, pp. 35–40.
DOI: 10.1016/j.foodchem.2015.02.081

7. Khodasevich M.A., Borisevich D.A. Identification of Flax Oil by Linear Multivariate Spectral Analys. *Journal of Applied Spectroscopy*, 2019, vol. 86, no. 6, pp. 880–884.
DOI: 10.1007/s10812-020-00929-z

8. Bro R., Smilde A.K. Principal component analysis. *Analytical Methods*, 2016, vol. 6, pp. 2812–2831.
DOI: 10.1039/C3AY41907J

9. Geladi P., Kowalski B.R. Partial Least-Squares Regression: A Tutorial. *Analytica Chimica Acta*, 1986, vol. 185, pp. 1–17.
DOI: 10.1016/0003-2670(86)80028-9

10. Soares S.F.C., Gomes A.A., Araujo M.C.U., Filho A.R.G., Galvão R.K.H. The successive projections algorithm. *TrAC Trends in Analytical Chemistry*, 2013, vol. 42, pp. 84–98.
DOI: 10.1016/j.trac.2012.09.006

11. Xiaobo Z., Jiewen Z., Malcolm J.W. Povey, Holmes M., Hanpin M. Variables selection methods in near-infrared spectroscopy. *Analytica Chimica Acta*, 2010, vol. 667, pp. 14–32.
DOI: 10.1016/j.aca.2010.03.048

12. Li Z., Wang J. , Xiong Y., Li Z., Feng S. The determination of the fatty acid content of sea buckthorn seed oil using near infrared spectroscopy and variable selection methods for multivariate calibration. *Vibrational Spectroscopy*, 2016, vol. 84, pp. 24–29.
DOI: 10.1016/J.VIBSPEC.2016.02.008

13. Wang L., Lee F., Wang X., He Y. Feasibility study of quantifying and discriminating soybean oil adulteration in camellia oils by attenuated total reflectance MIR and fiber optic diffuse reflectance NIR. *Food Chemistry*, 2006, vol. 95, pp. 529–536.
DOI: 10.1016/j.foodchem.2005.04.015

14. Khodasevich M.A., Aseev V.A. Selection of Spectral Variables and Improvement of the Accuracy

of Calibration of Temperature by Projection onto Latent Structures Using the Fluorescence Spectra of $Yb^{3+}:CaF_2$. *Optics and Spectroscopy*, 2018, no. 124, pp. 713–717.
DOI: 10.1134/S0030400X18050089

15. Nawar S., Mouazen A.M. Optimal sample selection for measurement of soil organic carbon using online vis-NIR spectroscopy. *Computers and Electronics in Agriculture*, 2018, vol. 151, pp. 469–477.
DOI: 10.1016/j.compag.2018.06.042

16. Li Y., Fang T., Zhu S., Huang F., Chen Zh., Wang Y. Detection of olive oil adulteration with waste cooking oil via Raman spectroscopy combined with iPLS and SiPLS. *Spectrochimica Acta Part A: Molecular and Biomolecular Spectroscopy*, 2018, vol. 189, pp. 37–43.
DOI: 10.1016/j.saa.2017.06.049

ПРАВИЛА ОФОРМЛЕНИЯ СТАТЕЙ

Статьи, направленные в редакцию журнала, должны удовлетворять требованиям «Инструкции о порядке оформления квалификационной научной работы (диссертации)…», утвержденной Постановлением ВАК РБ от 28.02.2014 г. № 3

1. Материал статьи должен соответствовать профилю журнала и излагаться предельно ясно.

2. Статья представляется на русском или английском языке и публикуется на языке представления.

3. Поступившие в редакцию статьи проходят двойное полуслепое рецензирование. Основные критерии целесообразности опубликования – актуальность тематики, информативность, научная новизна.

4. Статья представляется в распечатанном и в электронном виде в формате текстового редактора Word for Windows, набор – сплошным текстом (без деления на колонки). Объём статьи не должен превышать 14 страниц, включая текст (шрифт Times New Roman, размер 12 п., интервал 1,5), таблицы, графический материал, всю необходимую информацию на английском языке.

5. На первой странице статьи указываются: индекс УДК, название статьи, фамилии авторов (фамилия автора, с которым следует вести переписку, отмечается звёздочкой и указывается его адрес электронной почты), названия и почтовые адреса организаций (улица, номер дома, индекс, город, страна), в которых работают авторы, на русском и английском языках. Статья включает: аннотацию (в пределах 200–250 слов); ключевые слова (не более 5); введение, в котором делается краткий обзор сделанного в мире и конкретно формулируется цель работы; основную часть; заключение, в котором в сжатом виде сформулированы основные полученные результаты с указанием их новизны, преимуществ и возможностей применения; список использованных источников. Аннотация, ключевые слова, список использованных источников представляются на русском и английском языках.

6. Аннотация должна быть информативной (содержать «выжимку» из всех разделов статьи – введения с указанием цели работы, методики, основной части и заключения).

7. Графический материал должен быть контрастным и чётким. Необходимо придерживаться единообразия техники исполнения однотипных иллюстраций. Рисунок должен располагаться после абзаца, содержащего ссылку на него. Не допускается размещение рисунков в конце подраздела и статьи. Изобразительный материал вставляется в текст статьи, а также даётся в виде отдельных файлов **(формат tif, jpg, разрешение не менее 300 dpi).** Текст на рисунках набирается основной гарнитурой; размер кегля соизмерим с размером рисунка (желательно 8 пунктов). Все рисунки нумеруются и сопровождаются подрисуночными подписями. Фрагменты рисунка обозначаются строчными курсивными латинскими буквами – «*a*», «*b*» и т. д. Надписи на рисунках и подписи к рисункам даются на русском и английском языках. Все сокращения и обозначения должны быть расшифрованы в подрисуночной подписи. Рисунки желательно предоставлять в цвете. На рисунках должны быть указаны оси с обозначением приводимых величин и масштабов. На графиках не нужно давать координатную сетку, если это не осциллограмма. Во всех случаях на рисунках должен быть приведён масштаб.

8. У графиков, имеющих числовые значения по осям, рамки должны быть открыты, а засечки направлены внутрь рамки. На рисунках, представляющих собой графики зависимостей, не следует делать размерную сетку, следует дать лишь засечки на осях, причем все засечки должны быть оцифрованы. Если оси на рисунках оцифрованы, то они завершаются на позиции очередной засечки, где засечка не ставится, а вместо числовых значений даются обозначения переменной и единица измерения. Если оси не оцифровываются, то они завершаются стрелками, рядом с которыми даются обозначения переменных без единиц измерения.

9. Полутоновые фотографии приборов или их частей представляются при публикации в тех случаях, когда они несут существенную информацию, которую нельзя выразить иным способом. Фотографии должны быть высококачественными, контрастными, с хорошо различимыми деталями.

10. Иллюстрации (графики, диаграммы, схемы, чертежи), рисованные средствами MS Office, должны быть контрастными и чёткими. Недопустимо нанесение средствами MS Word каких-либо элементов поверх вставленного в файл рукописи рисунка (стрелки, подписи) ввиду большого риска их потери на этапах редактирования и вёрстки. Иллюстрации должны иметь размеры, соответствующие их информативности: 8–8,5 см (на одну колонку), 17–17,5 см (на две колонки) или 23 см (во весь лист). Поэтому желательно изображать отдельные элементы и надписи на рисунке так, чтобы при уменьшении масштаба рисунка до одного из указанных размеров буквы и цифры приобрели высоту 1,5–2 мм, элементы схем 3–5 мм, отдельные точки 1 мм, а линии должны быть при этом разнесены на расстояние не менее 0,5–1 мм.

11. Надписи и обозначения на иллюстрациях следует располагать так, чтобы они не соприкасались ни с какими её частями. На задний план иллюстрации желательно не добавлять серый (цветной) фон или сетки.

12. Таблицы не должны дублировать графики. Каждая таблица имеет заголовок. На все таблицы

и рисунки следует давать ссылки в тексте. Таблицы не должны содержать вертикальные линии, делящие таблицу на столбцы. Название и содержание таблиц представляется на русском и английском языках.

13. Обозначения и сокращения, принятые в статье, расшифровываются непосредственно в тексте.

14. Размерность всех величин, принятых в статье, должна соответствовать Международной системе единиц измерений (СИ).

15. Набор формул должен проводиться в редакторе MathType целиком. Набор формул из составных элементов не допускается, номера формул – по правому краю. Нумеруются лишь формулы, на которые есть ссылки в тексте.

16. Необходимо использовать следующие установки редактора формул. Размеры: полный – 10 пт, подстрочный – 9 пт, под-подстрочный – 7 пт, символ – 14,5 пт, подсимвол – 12,5 пт. Стили: текст, функция, число, кириллица – шрифт «Times New Roman», вектор-матрица – шрифт «Times New Roman», жирный; греческий малый, греческй большой, символ – шрифт «Symbol», прямой; переменная – шрифт «Times New Roman», курсив.

17. Отдельные строчные буквы и специальные символы набираются в тексте гарнитурой Symbol **без использования редактора формул**. При наборе формул и буквенных обозначений необходимо учитывать следующие правила: **русский алфавит не используется**; греческие буквы, математические символы (grad, div, ln, min, max и др.), единицы измерения (Вт, Дж, В, кг и др.), кириллические буквы, сокращения от русских слов ($q_{\text{ср}}$); обозначения химических элементов и соединений (в т. ч. в индексе) набираются **прямо**; латинские буквы – переменные и символы физических величин (в т. ч. в индексе) набираются **курсивом**; векторы – жирным шрифтом (стрелки вверху не ставятся).

18. Начертание обозначений в формулах и в основном тексте должно быть полностью идентично. В расшифровке формул, которая начинается словом «где», символы и их порядок должны соответствовать символам и их порядку следования в формулах.

19. Список использованных источников составляется в порядке упоминания ссылок по тексту, должен содержать полные библиографические данные и приводится в конце статьи. Не рекомендуется давать ссылки на материалы конференций, статьи из электронных журналов без идентификатора **DOI**, учебные пособия, интернет-ресурсы. Ссылки на неопубликованные работы не допускаются. Желательно, чтобы количество ссылок было не менее 10; самоцитирование – не более 20 %.

20. Авторы на отдельной странице предоставляют о себе следующие сведения: фамилия, имя, отчество, ученая степень и звание, место работы и занимаемая должность, адрес электронной связи.

21. Статьи, излагающие результаты исследований, выполненных в учреждениях, должны иметь соответствующее разрешение на опубликование в открытой печати.

22. При необходимости в конце основного текста указываются наименование фонда, оказавшего финансовую поддержку, или уровень и наименование программы, в рамках которой выполнена работа, на русском и английском языках.

23. Авторы несут ответственность за направление в редакцию статей, ранее уже опубликованных или принятых к печати другими изданиями.

24. Статьи, не соответствующие перечисленным требованиям, к рассмотрению не принимаются и возвращаются авторам. Датой поступления считается день получения редакцией первоначального варианта текста.

25. Редакция предоставляет возможность первоочередного опубликования статей лицам, осуществляющим послевузовское обучение (аспирантура, докторантура, соискательство), в год завершения обучения; не взимает плату с авторов за опубликование научных статей; оставляет за собой право производить редакторские правки, не искажающие основное содержание статьи.

AUTHOR GUIDELINES

1. Article materials should correspond to the journal profile and be clearly written.
2. An article should be submitted in Russian or English and will be published in its original language.
3. Articles received by the Editorial Board will be reviewed by 2 specialists. The main criteria of acceptance are theme actuality, information value, and scientific novelty.
4. All materials should be submitted in two hard copies together with electronic file in the Word for Windows format (97/2000/2003). The paper should not exceed 14 pages of the typewritten text (Times New Roman, 12 points, 1.5-space).
5. The article should contain UDC number, Title (printed in capitals), Authors' names (the corresponding author name should be marked with asterisk), full Address of organization(s) in which the author(s) work, Abstract (200–250 words), Keywords (not more than 5 words), Introduction, the Text of the paper with tables, diagrams and figures (if there are any), Conclusion with clearly stated inferences, List of References, List of Symbols and Abbreviations (if it is necessary). Title, Authors' names and affiliation(s), Abstract, Keywords should be presented both in English and Russian languages.
6. The abstract should be informative (contain «squeeze» from all sections of the article – the introduction stating the purpose of the work, methods, main part and conclusion).
7. Figures should be black-and-white, represented in graphical formats tif, attached with Excel or MS Graph and added with captions. All symbols in figures should be descripted.
8. Tables should be placed directly in the article body. Diagrams and tables should not contain the same information. Each table should have the title. All tables, diagrams and figures should be referenced in the text.
9. Symbols and abbreviations which are used in articles should be deciphered directly in the text and also (if necessary) taken out on a separate page.
10. Dimensions of all quantities used in the article should correspond to International System of Units.
11. Formulas should be taped in MathType.
12. List of References is to be placed at the end of the article with full bibliographic information. Order of references should correspond to the order of their occurrence in the text. It is not recommended to refer to conference proceedings, papers from electronic journals without *DOI* number, textbooks, internet resources. References on unpublished works are prohibited. It is recommended to refer to not less than 10 references, self-citations – not more than 20 %/
13. The following information about every co-author should be presented: family name, first name, patronymic (or second) name (if there are any), scientific degree and title, organization and position, full address with the postal code for correspondence, office or mobile phone numbers, fax, e-mail.
14. Articles containing investigation results obtained in organizations should have a corresponding permission for publication.
15. Names of Foundations or Programs financially granted the research may be acknowledged in the end of the text.
16. Authors are responsible for submitting articles previously published or accepted by other publisher.
17. Articles not meeting the requirements of the Editorial Board would not be accepted and may be returned to the authors. The date of receipt is considered to be the day when the Editorial Board receives the author's original paper.
18. Authors conducting postgraduate (graduate studies, doctoral studies) have a priority in publishing their articles out of queue in the year of completion. Authors do not pay for publishing scientific articles. The Editorial Board can shorten and/or change the text if it does not strain the meaning of the article.

Индексы:
74835; 748352